Study of D^0- $\overline{D}^0$ mixing parameters using a time-dependent amplitude analysis of the decay $D^0 \to K^0_S\pi^+\pi^-$

A dissertation submitted to the

Graduate School

of the University of Cincinnati

in partial fulfillment of the

requirements for the degree of

Doctor of Philosophy

in the Department of Physics

of the College of Arts and Sciences

by

Rolf Andreassen

Cand. Scient. University of Bergen

Cand. Mag. University of Bergen

Committee Co-chair: M. Sokoloff, Ph.D.

Committee Co-Chair: B. Meadows, D.Phil.

Abstract

I present a measurement of the mixing parameters in the D meson system, using 473.5 fb^{-1} of data from the *BABAR* detector. A time-dependent fit to the Dalitz plot of the decay $D^0 \to K_s\pi^+\pi^-$, assuming no CP violation, finds for the $D^0 - \overline{D^0}$ mixing parameters, the normalised mass and width differences x and y

$$\begin{aligned} x &= (0.43 \pm 0.25 \pm 0.20)\% \\ y &= (0.70 \pm 0.22 \pm 0.17)\% \end{aligned}$$

where the uncertainties are statistical and systematic. For D^0 and $\overline{D}^0$ samples separately, we find

$$\begin{aligned} x_{D^0} &= (0.49 \pm 0.36 \pm 0.20)\% \\ y_{D^0} &= (0.82 \pm 0.31 \pm 0.17)\% \\ x_{\overline{D}^0} &= (0.46 \pm 0.35 \pm 0.20)\% \\ y_{\overline{D}^0} &= (0.55 \pm 0.31 \pm 0.17)\%. \end{aligned}$$

Acknowledgements

This thesis is dedicated to the memory of my grandfather, Albert Edward Randall, who passed away before it could be completed. I wish he could have seen it.

Thanks are due to my advisors, Mike Sokoloff and Brian Meadows, for their patience, good humour, and good advice.

Contents

Chapter 1

Introduction

1.1 Definition and previous work

Mixing occurs in neutral meson systems when the mass and flavour eigenstates differ. Since only the mass eigenstates appear in the equations of motion, a meson that initially has an un-ambiguous flavour will at later times be in a superposition of that flavour and its anti-flavour. For example, a meson created as a D^0 - purely charm - will at later times have a component of anti-charm, and may therefore decay as a $\overline{D}^0$.

Mixing has been observed in the K, B and B_s mesons, ([1, 2, 3]). In these systems, however, it is very large and therefore easy to measure. In the D system, mixing is (in the Standard Model) suppressed by a combination of CKM and GIM factors ([4]; see also Chapter 2). This makes the observation of mixing interesting in its own right, because a large amount might indicate physics outside the Standard Model and because mixing must be established before CP violation in mixing can be studied. Nevertheless, D meson mixing has been measured recently using the very large samples of D mesons produced by the *BABAR* and Belle B factories (e.g., [5, 6, 7, 8, 9, 10]).

In the case where a neutral D meson decays into a state accessible from both flavours, such as $K_s\pi^+\pi^-$, there are two possible paths for the D^0 to follow: It may decay directly, or it may first oscillate into a $\overline{D}^0$ and only then decay. Because these two paths are quantum-

mechanically indistinguishable, they interfere. We can observe this in the distribution of D^0 decay times. In the case of no mixing, the decay-time distribution is purely exponential, $P(t) = (1/\tau)e^{-t/\tau}$ with τ a real number. $D^0 - \overline{D^0}$ mixing changes this simple shape. The full formalism of mixing is described in Chapter 2; in the limit of no *CP* violation it is usually parametrised by the quantities x and y, which are the normalised mass and width differences between the mass eigenstates. Figure 1.1 shows how the average D^0 decay time varies across the Dalitz plot when we assume $x = 0.80\%$, $y = 0.33\%$ as in [5]; Figure 1.2 shows the same variation for other mixing parameter values.

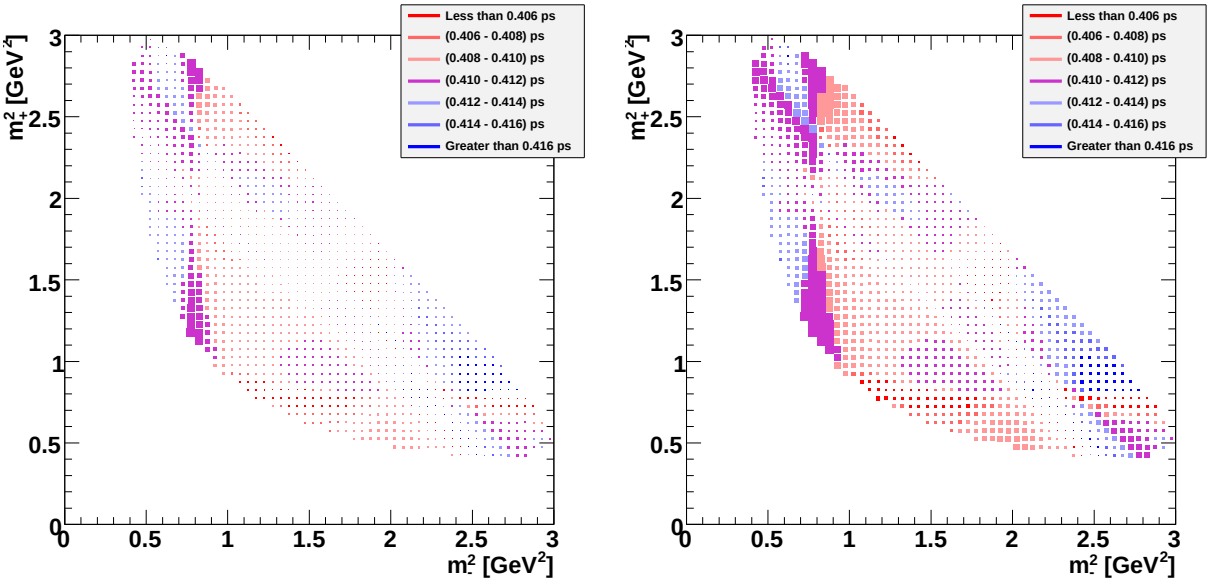

(a) Linear

(b) Capped linear

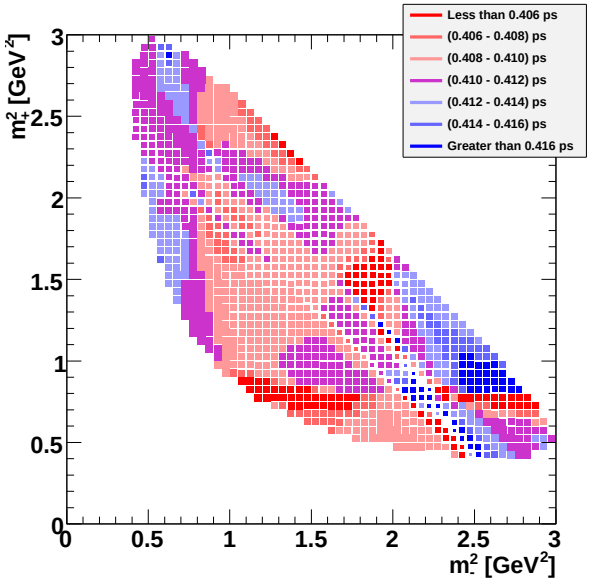

(c) Logarithmic

Figure 1.1: Average decay time as a function of position on the Dalitz plot, for $x = 0.8\%$, $y = 0.33\%$. The size of the boxes varies with the number of events; for clarity, the same data is shown in three different ways. In a) the box size is linear in the number of events. In b) the box size is linear up to 25% of the maximum number of events, and constant thereafter; this brings out the low-density parts of the plot better. In c) the box size is logarithmic in the number of events. m_+ and m_- are the masses of pairs of D^0 daughters, $K^0_S\pi^+$ and $K^0_S\pi^-$ respectively.

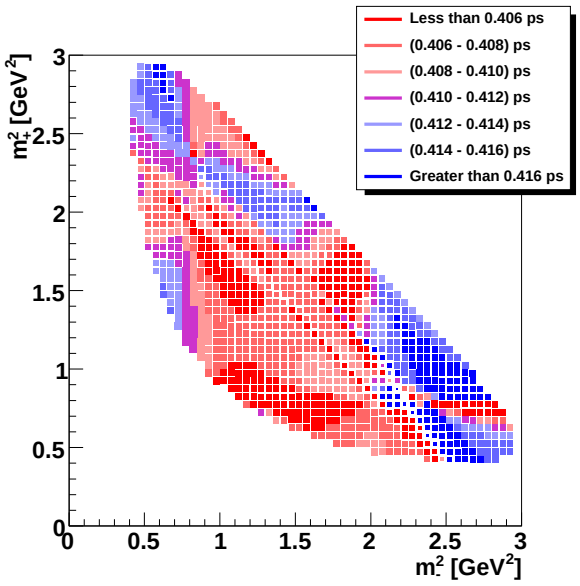

(a) $x = y = 1\%$

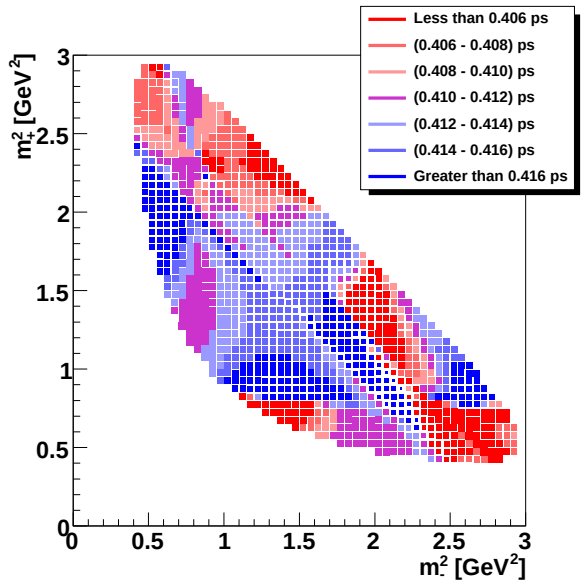

(b) $x = 1\%$, $y = -1\%$

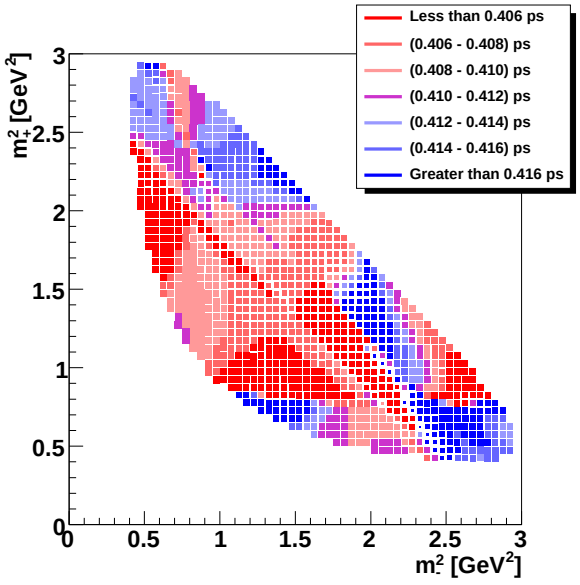

(c) $x = -1\%$, $y = 1\%$

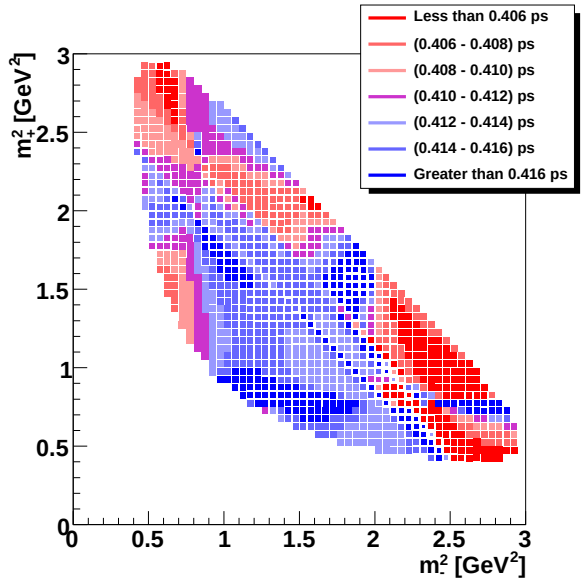

(d) $x = y = -1\%$

Figure 1.2: Average decay time as a function of position on the Dalitz plot for different mixing parameters. The box size is logarithmic in the number of events.

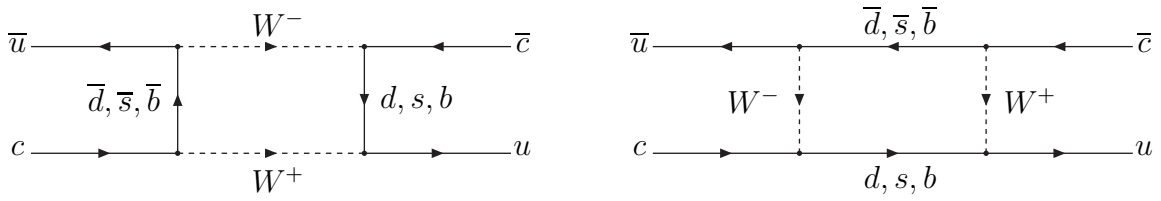

Figure 1.3: Feynman box diagrams of $D^0 \to \overline{D}^0$ oscillations.

1.2 The Standard Model

The Standard Model explains particle interactions in terms of the electroweak force, mediated by the carrier particles γ, Z^0, and $W^{\pm}$, and the strong force, mediated by gluons. The carrier particles all have spin one, making them bosons. The fundamental particles known to exist (apart from the carriers) are three generations of leptons, $e^{\pm}$, $\mu^{\pm}$ and $\tau^{\pm}$ with corresponding neutrinos $\nu_{e,\mu,\tau}$ and anti-neutrinos $\overline{\nu}_{e,\mu,\tau}$, and three of quarks and anti-quarks, with labels up, down, charm, strangeness, truth, and beauty; the labels are conventionally shortened to the first letter, with a bar indicating anti-quarks, e.g. u and $\overline{u}$ for up and anti-up. All of these particles are fermions, that is, they have spin one-half.

The quarks are classified by their electric charge into 'up-type' (u, c, and t) which have charge $+2/3$, and 'down-type' (d, s, and b) with charge $-1/3$. They also carry one of three 'colours', (strong charge), and are therefore bound into mesons (quark-antiquark pairs) and baryons (three-quark systems) due to the 'colour-confinement' property of the strong force. This comes about because gluons, the carriers of the strong force, also have strong charge, and thus interact further with the particles whose force they are mediating, and with the gluons mediating this interaction. This causes the strong force to be stronger at larger distances (a property called 'infrared slavery') and notoriously intractable computationally. Conversely it is weak at short distances ('asymptotic freedom'), where perturbative calculations are possible. The electroweak force, on the other hand, can be treated with perturbation theory at all distances, which allows very precise predictions; for example, the muon magnetic

moment has been calculated to nine significant digits ([11]).

The charged weak-force carriers $W^{\pm}$ do not couple to the pure quark states, but rather to superpositions of quark flavours; or equivalently, weak charged-current interactions do not conserve flavour. This causes the lightest particle with a given flavour to be relatively long-lived compared to heavier excitation states of the same flavour (but not stable, as it would be if flavour were conserved in all interactions), because it has to wait for the slow weak interaction to change its heavy quark to something lighter. For example, the D^* decays to a D^0 and a pion much more rapidly than the D^0 decays, because the D^* decay proceeds through the strong force, while the D^0 has to wait for its c quark to decay to an s or d quark through a weak interaction. The strengths of the quark couplings are given by the Cabibbo-Kobayashi-Maskawa, or CKM, matrix:

$$V_{CKM} = \begin{pmatrix} V_{ud} & V_{us} & V_{ub} \\ V_{cd} & V_{cs} & V_{cb} \\ V_{td} & V_{ts} & V_{tb} \end{pmatrix}. \tag{1.1}$$

The V_{ij} gives the coupling strength between quarks of flavours i and j. Notice that there are no terms coupling up-type to up-type or down-type to down-type quarks; only charged currents - that is, interactions involving the $W^{\pm}$ carriers - can change quark flavours, an experimental fact summed up in the phrase "flavour-changing neutral currents don't exist."

The Higgs mechanism with its eponymous particle is the current best guess for where mass comes from; but the Standard Model does not predict the mass of the fundamental particles, which must be inserted by hand from experimental results. The source of mass is therefore an example of New Physics, a catchall phrase for mechanisms not covered by the Standard Model. Further, although the Standard Model does allow for *CP* violation - that is, interactions whose rate changes when particles are replaced by antiparticles (and vice versa) and spatial coordinates are reversed - such violation only appears in the quark sector, through complex terms in the CKM matrix, and is too small (Ref. [12]) to explain the observed asymmetry between matter and anti-matter in the Universe. (In particular, all

we can see is made of matter, and there is no observable antimatter outside of very energetic particle collisions.) A source of additional *CP* violation is therefore a much sought-after kind of New Physics.

Within the Standard Model, D^0-$\overline{D}^0$ oscillations are explained by the box diagram (Figure 1.3), and also by long-range strong-force effects which cannot be calculated perturbationally. These processes are expected to be slow, below the current experimental sensitivity (see Chapter 2 for a fuller discussion), yet D mixing has been observed. It follows that either something important has been missed in making the Standard Model prediction, or New Physics is at work. For example, inserting unknown particles into the intermediate state of the box diagram can increase the rate of oscillation, and can also cause additional *CP* violation in the process.

1.3 Motivation

The Standard Model, to the extent that the calculation is possible, predicts a small value for the mixing parameters (defined in Eqns 2.8-2.9), that is, $x, y \ll 1\%$, although [13] argues that $(x, y) \sim 1\%$ may be possible in the presence of SU(3) breaking by phase-space asymmetries. The B-factory data sets are now sufficiently large that the sensitivity of mixing measurements are on the order of a few tenths of a percent, leading to the possibility of seeing mixing rates more compatible with New Physics processes than with the Standard Model.

It is further expected that $|x| \leq |y|$. Testing this prediction is made complicated by the existence of an unknown strong phase δ in hadronic mixing channels whose final state is not a *CP* eigenstate, as explained in Chapter 2, which means that only a rotated pair

$$x' = x\cos\delta + y\sin\delta \tag{1.2}$$

$$y' = -x\sin\delta + y\cos\delta \tag{1.3}$$

can be measured. When the final state is a *CP* eigenstate, e.g. $K_s\pi^+\pi^-$, the interference between direct, Cabibbo-suppressed decays and mixed decays makes it possible to account

for this strong phase and measure x and y directly. Additionally, since measurements not using such final states map out an annulus of possible values in x-y space, $K_s\pi^+\pi^-$ decays can give information about strong phases in other decays by fixing the underlying x and y values.

Finally, by measuring mixing rates separately for D^0 and $\overline{D}^0$ samples, we may find evidence of CP violation in mixing, which would be an indication of New Physics.

1.4 Organisation

This document is organised as follows. Chapter 2 describes the formalism of D^0 mixing. Chapters 3 and 4 describe the *BABAR* detector and the event sample used for the analysis. Chapter 5 describes the model of three-body D^0 decays used in the fit to the Dalitz plot. Chapter 6 explains the three-step fit used to extract the mixing parameters, and Chapter 7 considers the systematic uncertainties associated with this. Finally, Chapter 8 gives the results of the analysis.

Chapter 2

Formalism

This chapter contains a formal description of D meson mixing; it largely follows the discussion in [14] and the corrections thereto in [15].

2.1 Time development of flavour eigenstates

In $D^* \to D^0\pi_s$ decays, the D meson is produced in a pure flavour eigenstate, $|D^0\rangle$ or $|\overline{D}^0\rangle$. These flavour eigenstates are not equal to the mass and lifetime eigenstates,

$$|D_1\rangle = p|D^0\rangle + q|\overline{D}^0\rangle \tag{2.1}$$

$$|D_2\rangle = p|D^0\rangle - q|\overline{D}^0\rangle, \tag{2.2}$$

by which they propagate and decay. Therefore, a particle produced as a D^0 will be in a superposition of D^0 and $\overline{D}^0$ by the time it decays; a sufficiently long-lived meson will oscillate back and forth between the two flavour states several times. The process is governed by the mass and lifetime differences of the D_1 and D_2 states; these decay according to

$$|D_1(t)\rangle = e_1(t)|D_1\rangle = e^{-i(m_1 - i\Gamma_1/2)t}|D_1\rangle \tag{2.3}$$

$$|D_2(t)\rangle = e_2(t)|D_2\rangle = e^{-i(m_2 - i\Gamma_2/2)t}|D_2\rangle \tag{2.4}$$

where m_i, Γ_i are the mass and width of the D_i state. We define

$$\begin{aligned}
\Delta M &= m_1 - m_2 && (2.5)\\
\Delta\Gamma &= \Gamma_1 - \Gamma_2 && (2.6)\\
\Gamma &= (\Gamma_1 + \Gamma_2)/2 && (2.7)\\
x &= \Delta M/\Gamma && (2.8)\\
y &= \Delta\Gamma/2\Gamma && (2.9)\\
R_M &= (x^2 + y^2)/2. && (2.10)
\end{aligned}$$

The quantities x and y are collectively referred to as mixing parameters.

Eqns 2.3 and 2.4 give the time development of the mass eigenstates. For our purpose it is more convenient to consider the time evolution of the flavour eigenstates. A particle that is a pure D^0 or $\overline{D}^0$ at time zero (i.e. production time) will evolve thus:

$$\begin{aligned}
|D^0(t)\rangle &= \frac{1}{2p}\left[p\left(e_1(t) + e_2(t)\right)|D^0\rangle + q\left(e_1(t) - e_2(t)\right)|\overline{D}^0\rangle\right] && (2.11)\\
|\overline{D}^0(t)\rangle &= \frac{1}{2q}\left[p\left(e_1(t) - e_2(t)\right)|D^0\rangle + q\left(e_1(t) + e_2(t)\right)|\overline{D}^0\rangle\right]. && (2.12)
\end{aligned}$$

This is fully general; we now consider the case of three-body decays through quasi-two-body intermediate states - for example, the $D^0 \to K^0_S\pi^-\pi^+$ decay. Chapter 5 describes the intermediate states used in our model. We denote the Dalitz-plot variables $m_{K^0_S\pi^+} = m_+$ and $m_{K^0_S\pi^-} = m_-$. The amplitude for the D^0 to decay through the jth quasi-two-body state to a final Dalitz-plot position (m^2_+, m^2_-) is $c_j\mathcal{A}^j_k(m^2_+, m^2_-)$, where c_j is a complex coefficient, and $\mathcal{A}^j_k(m^2_+, m^2_-)$ is typically (but not necessarily; see Chapter 5) the spin-k Breit-Wigner amplitude for the resonance j:

$$\begin{aligned}
\mathcal{A}^j_k(m^2_+, m^2_-) &= \frac{m^2_j - m^2_{AB} + im_j\Gamma_j}{(m^2_j - m^2_{AB})^2 + m^2_j\Gamma^2_j}F_kF_DS_k && (2.13)\\
&= \frac{F_kF_DS_k}{(m^2_j - m^2_{AB}) - im_j\Gamma_j}. && (2.14)
\end{aligned}$$

Here m_j is the nominal mass of resonance j and Γ_j is its running width, given by

$$\Gamma_j = \Gamma_{j0}\frac{m_j}{m_{AB}}\left(\frac{p_{CM}(m_{AB})}{p_{CM}(m_j)}\right)^{2k+1} F_k^2 \tag{2.15}$$

with Γ_{j0} the nominal width for resonance j. $p_{CM}(x)$ is the momentum of the j decay products AB in the j rest frame on the assumption that j's mass is x. m_{AB} is the measured mass of the decay products of j, labeled A and B (the third final-state particle rejoices in the label C). For the particular case of the $D^0 \to K_s\pi^+\pi^-$ decay, we specify $A = K_s$, $B = \pi^+$, $C = \pi^-$ and use the notation $m_{AB} = m_+$, $m_{BC} = m_0$, and $m_{AC} = m_-$, referring to the charges of the daughters. Further,

$$F_k = \begin{cases} 1, & k = 0 \\ \sqrt{\frac{1+R^2p_{CM}^2(m_j)}{1+R^2p_{CM}^2(m_{AB})}}, & k = 1 \\ \sqrt{\frac{9+4R^2p_{CM}^2(m_j)+R^4p_{CM}^4(m_j)}{9+4R^2p_{CM}^2(m_{AB})+R^4p_{CM}^4(m_{AB})}}, & k = 2 \end{cases} \tag{2.16}$$

is the spin-k damping factor. R, the effective meson radius, is taken as 1.5 c/GeV. The form factor F_D is included by convention, but for this analysis we take it equal to 1, and leave it out of equations from this point. Finally,

$$S_k = \begin{cases} 1, & k = 0 \\ m_{BC}^2 - m_{AC}^2 + \frac{(m_D^2-m_C^2)(m_A^2-m_B^2)}{m_{AB}^2}, & k = 1 \\ \left(m_{BC}^2 - m_{AC}^2 + \frac{(m_D^2-m_C^2)(m_A^2-m_B^2)}{m_{AB}^2}\right)^2 & \\ -\frac{1}{3}\left(m_{AB}^2 - 2m_D^2 - 2m_C^2 + \frac{(m_D^2-m_C^2)^2}{m_{AB}^2}\right), & k = 2 \\ \times\left(m_{AB}^2 - 2m_A^2 - 2m_B^2 + \frac{(m_A^2-m_B^2)^2}{m_{AB}^2}\right) & \end{cases} \tag{2.17}$$

is the spin factor for spin k, with m_D the nominal D^0 mass. The spin factor as written here

hides the underlying spherical harmonics that are, nonetheless, present, in the calculation of the two-daughter masses. The corresponding Breit-Wigner for the $\overline{D}^0$, that is, the amplitude for $\overline{D}^0$ to decay through the resonance j to the final state (m_+^2, m_-^2), is denoted $\overline{\mathcal{A}_k^j}$.

The decay rate to a particular point on the Dalitz plot at time t, for an initially pure D^0 meson, is given (assuming CP conservation) by

$$d\Gamma(m_+^2, m_-^2, t) = \frac{|\mathcal{M}|^2 dm_+^2 dm_-^2}{256\pi^3 m_D^3} \tag{2.18}$$

$$|\mathcal{M}|^2 = \langle K_S^0\pi^+\pi^-(m_+^2, m_-^2)|\mathcal{H}|D^0(t)\rangle \tag{2.19}$$

where m_D is the mass of the D^0. We now consider $|\mathcal{M}|^2$ in terms of a linear combination of the intermediate states, which we split into three classes: CP-even, CP-odd, and flavour eigenstates. Let $|f_{+,-}\rangle$ define intermediate states with phase space coordinates (m_+, m_-), with the sign indicating CP-even or odd, respectively; and let $|f\rangle$ ($|\overline{f}\rangle$) denote intermediate states which are D^0 ($\overline{D}^0$) flavour eigenstates. Note that $\overline{f}$ refers to the same intermediate states, but the opposite spot in the Dalitz plot, $(m_1^2, m_2^2) \to (m_2^2, m_1^2)$. Then we have

$$\langle f_{+,-}|\mathcal{H}|D^0\rangle = A_{+,-} = \sum_{even,odd} c_j \mathcal{A}_k^j \tag{2.20}$$

$$\langle \overline{f_{+,-}}|\mathcal{H}|D^0\rangle = \pm A_{+,-} = \sum_{even,odd} c_j \overline{\mathcal{A}_k^j} \tag{2.21}$$

$$\langle f|\mathcal{H}|D^0\rangle = A_f = \sum_{flavour} c_j \mathcal{A}_k^j \tag{2.22}$$

$$\langle \overline{f}|\mathcal{H}|\overline{D}^0\rangle = \overline{A}_{\overline{f}} = \sum_{flavour} c_j \overline{\mathcal{A}_k^j}. \tag{2.23}$$

By analogy, $\langle \overline{f}|\mathcal{H}|D^0\rangle = A_{\overline{f}}$ and $\langle f|\mathcal{H}|\overline{D}^0\rangle = \overline{A}_f$ are the respective sums over flavour eigenstates into the final state $\langle \overline{f}|$, or from the initial state $|\overline{D}^0\rangle$, respectively. This is a convenient shorthand for the next step, which is to take the inner product of Eqn 2.11 and $\langle f|\mathcal{H}$ and collect terms with similar time dependences:

$$\mathcal{A}(D \to f) = \langle f|\mathcal{H}|D^0(t)\rangle \tag{2.24}$$

$$= \frac{1}{2p}\langle f|\mathcal{H}|\left[p\left(e_1(t) + e_2(t)\right)|D^0\rangle + q\left(e_1(t) - e_2(t)\right)|\overline{D}^0\rangle\right]$$

$$
\begin{aligned}
&= \frac{e_1(t)}{2p}\langle f|\mathcal{H}|pD^0 + q\overline{D}^0\rangle + \frac{e_2(t)}{2p}\langle f|\mathcal{H}|pD^0 - q\overline{D}^0\rangle \\
&= \frac{e_1(t)}{2p}\left(p(A_+ + A_- + A_f) + q(\overline{A}_+ + \overline{A}_- + \overline{A}_f)\right) \\
&\quad + \frac{e_2(t)}{2p}\left(p(A_+ + A_- + A_f) - q(\overline{A}_+ + \overline{A}_- + \overline{A}_f)\right) \\
&\equiv A_1 e_1(t) + A_2 e_2(t)
\end{aligned}
$$

and similarly for Eqn 2.12

$$
\begin{aligned}
\mathcal{A}(\overline{D} \to \overline{f}) &= \frac{e_1(t)}{2q}\left(p(A_+ + A_- + A_{\overline{f}}) + q(\overline{A}_+ + \overline{A}_- + \overline{A}_{\overline{f}})\right) && (2.25)\\
&\quad + \frac{e_2(t)}{2p}\left(p(A_+ + A_- + A_{\overline{f}}) - q(\overline{A}_+ + \overline{A}_- + \overline{A}_{\overline{f}})\right) && (2.26)\\
&\equiv \overline{A_1} e_1(t) + \overline{A_2} e_2(t). && (2.27)
\end{aligned}
$$

It is worth remembering the purpose of this algebra: We have re-expressed the amplitude for a particle produced as a flavour eigenstate to decay to a particular point on the Dalitz plot at time t in terms of sums over amplitudes of intermediate states. The innocent-looking symbol A_1 hides a large number of complex relative amplitudes, a strong dependence through the Breit-Wigner functions on position in the Dalitz plot, and two *CP*-related parameters p and q. Using this shorthand, we can find the time-dependent decay rates at each point in the Dalitz plot:

$$
\begin{aligned}
|\mathcal{M}|^2 &= |\mathcal{A}(D \to f)|^2 && (2.28)\\
&= |A_1|^2|e_1(t)|^2 + |A_2|^2|e_2(t)|^2 + 2\Re\left(e_1(t)e_2(t)^* A_1 A_2^*\right) \\
&= |A_1|^2 e^{-(1+y)t/\tau} + |A_2|^2 e^{-(1-y)t/\tau} + 2\Re\left(e^{-(1+ix)t/\tau} A_1 A_2^*\right) \\
&= |A_1|^2 e^{-(1+y)t/\tau} + |A_2|^2 e^{-(1-y)t/\tau} \\
&\quad + 2\Re\left(A_1 A_2^*\right) e^{-t/\tau}\cos(xt/\tau) + 2\Im\left(A_1 A_2^*\right) e^{-t/\tau}\sin(xt/\tau) \\
|\overline{\mathcal{M}}|^2 &= |\mathcal{A}(\overline{D} \to \overline{f})|^2 && (2.29)\\
&= |\overline{A_1}|^2|e_1(t)|^2 + |\overline{A_2}|^2|e_2(t)|^2 + 2\Re\left(e_1(t)e_2(t)^* \overline{A_1 A_2^*}\right) \\
&= |\overline{A_1}|^2 e^{-(1+y)t/\tau} + |\overline{A_2}|^2 e^{-(1-y)t/\tau} + 2\Re\left(e^{-(1+ix)t/\tau} \overline{A_1 A_2^*}\right)
\end{aligned}
$$

$$
\begin{aligned}
&= |\overline{A_1}|^2 e^{-(1+y)t/\tau} + |\overline{A_2}|^2 e^{-(1-y)t/\tau} \\
&\quad +2\Re\left(\overline{A_1}\overline{A_2^*}\right) e^{-t/\tau}\cos(xt/\tau) + 2\Im\left(\overline{A_1}\overline{A_2^*}\right) e^{-t/\tau}\sin(xt/\tau).
\end{aligned}
$$

In Chapter 6 we describe a convolution of Eqn 2.29 with a time-resolution function, to form the time-dependent Dalitz-plot distribution we fit to.

So far we have assumed *CP* conservation. We distinguish between direct and indirect *CP* violation; direct *CP* violation means that the D^0 decay amplitudes differ from the $\overline{D}^0$ amplitudes; indirect *CP* violation occurs when either the mixing rates or the interference between mixed and direct decays are different - for example, if D^0 oscillates to $\overline{D}^0$ faster than vice-versa. For this purpose it is convenient to return to the amplitude:

$$
\begin{aligned}
\mathcal{A}(D \to f) &= \frac{e_1(t)}{2p}\left(p(A_+ + A_- + A_f) + q(\overline{A}_+ + \overline{A}_- + \overline{A}_f)\right) && (2.30)\\
&\quad +\frac{e_2(t)}{2p}\left(p(A_+ + A_- + A_f) - q(\overline{A}_+ + \overline{A}_- + \overline{A}_f)\right) && (2.31)\\
&= \frac{e_1(t)}{2}\left[(1+\chi_f)A_f + (1+\chi_+)A_+ + (1+\chi_-)A_-\right] && (2.32)\\
&\quad +\frac{e_2(t)}{2}\left[(1-\chi_f)A_f + (1-\chi_+)A_+ + (1-\chi_-)A_-\right] && (2.33)\\
\mathcal{A}(\overline{D} \to \overline{f}) &= \frac{e_1(t)}{2}\left[(1+\chi_{\overline{f}}^{-1})\overline{A}_{\overline{f}} + (1+\chi_+^{-1})\overline{A}_+ + (1+\chi_-^{-1})\overline{A}_-\right] && (2.34)\\
&\quad +\frac{e_2(t)}{2}\left[(1-\chi_{\overline{f}}^{-1})\overline{A}_{\overline{f}} + (1-\chi_+^{-1})\overline{A}_+ + (1-\chi_-^{-1})\overline{A}_-\right]. && (2.35)
\end{aligned}
$$

The χ are defined thus:

$$
\begin{aligned}
\chi_f &\equiv \frac{q\overline{A}_f}{pA_f} && (2.36)\\
\chi_{\overline{f}} &\equiv \frac{q\overline{A}_{\overline{f}}}{pA_{\overline{f}}} && (2.37)\\
\chi_+ &\equiv \frac{q\overline{A}_+}{pA_+} && (2.38)\\
\chi_- &\equiv \frac{q\overline{A}_-}{pA_-}. && (2.39)
\end{aligned}
$$

In the absence of direct *CP* violation this becomes

$$\chi_f = \left|\frac{\overline{A}_f}{A_f}\right| \frac{1-\epsilon}{1+\epsilon} e^{i(\delta_f+\phi)} \quad (2.40)$$

$$\chi_{\overline{f}} = \left|\frac{\overline{A}_{\overline{f}}}{A_{\overline{f}}}\right| \frac{1-\epsilon}{1+\epsilon} e^{-i(\delta_f-\phi)} \quad (2.41)$$

$$\chi_{+,-} = \pm\frac{1-\epsilon}{1+\epsilon} e^{i\phi}. \quad (2.42)$$

where δ_f is the strong phase between $D^0 \to K_s\pi\pi$ and $\overline{D}^0 \to K_s\pi\pi$, and ϕ and ϵ are *CP*-violation parameters; ϵ is given by

$$\epsilon = \frac{p-q}{p+q}. \quad (2.43)$$

In the semileptonic case, where there is no doubly-Cabibbo-suppressed term in the time dependence, we are only sensitive to ϵ; we may therefore refer (a little loosely) to this as measuring the "*CP* violation in mixing". In hadronic channels, which have a DCS term and a term for the interference between DCS decays and mixing, we are also sensitive to ϕ. In the limit of *CP* symmetry both ϵ and ϕ are zero. Note that there is an asymmetry between $\chi_{f,\overline{f}}$ and $\chi_{+,-}$: The latter are exactly ± 1 in the absence of *CP* violation; the former are not. We are therefore sensitive to mixing even in the absence of *CP* violation, but not vice-versa.

2.2 Standard Model predictions

The box diagrams shown in Figure 1.3 are suppressed in two ways: First, there is the CKM suppression of c coupling to d and b, and u coupling to s and (especially) b; and second, there is suppression by the GIM (Glashow, Iliopoulos, and Maiani) mechanism (Refs [16, 4]). To see this, first notice that box diagrams having a b in the loop carry a factor V_{ub}, which is tiny. To a very good approximation we may ignore these diagrams; this is the CKM suppression. It follows that there are four versions of the box diagrams that matter, created by choosing either s or d quarks for the two inner lines. We shall now show that these

diagrams are suppressed; although the argument makes use of CKM quantities, it is called GIM suppression. Label the four non-negligible diagrams $s\overline{s}$, $d\overline{d}$, $s\overline{d}$ and $d\overline{s}$. Since we are now working only in the first two generations of quarks, the CKM matrix reduces to the Cabibbo matrix. The box diagrams consist of two kinds of quark lines: csu and cdu. The first kind has a cs vertex of strength $\cos\theta_C$ followed by an su vertex with $\sin\theta_C$. The second kind has a cd vertex, which is $-\sin\theta_C$ (note the sign!), and a du of strength $\cos\theta_C$. Thus the four kinds of box diagram exactly cancel:

$$s\overline{s} \propto (\sin\theta_C \cos\theta_C)^2 \tag{2.44}$$

$$d\overline{d} \propto (-\sin\theta_C \cos\theta_C)^2 \tag{2.45}$$

$$d\overline{s} \propto (-\sin\theta_C \cos\theta_C)(\sin\theta_C \cos\theta_C) \tag{2.46}$$

$$s\overline{d} \propto (\sin\theta_C \cos\theta_C)(-\sin\theta_C \cos\theta_C) \tag{2.47}$$

and the sum is zero. This is the GIM suppression mechanism. However, in reality the cancellation is not quite exact, because the s and d quarks are not really identical; SU(3) symmetry (on which the argument just made relies) is broken by the quark masses. In particular, the masses appear in the propagators of the internal quarks. It can be shown (Ref. [4]) that this leads to a factor $(m_s^2 - m_d^2)^2/m_c^4$ giving, with non-leading terms also included, x and y both of order 10^{-3}. Notice that this argument does not apply to B or K mixing, which can have the heavy c quark in the loop - SU(3) symmetry is very strongly broken in these cases.

So far we have considered short-distance effects calculable by perturbation theory; but there are also long-distance effects. Here it is necessary to make more qualitative arguments. (For an overview of Standard Model methods and of experimental constraints on New Physics, see Ref. [17] and references therein.) We saw above that D mixing arises only in the presence of SU(3) breaking; Falk et. al. in Ref. [13] show that it occurs in the second (and higher) order of SU(3)-breaking parameters. They then consider the amount of SU(3)-breaking that can arise from phase-space differences in hadronic intermediate states,

abandoning the assumption of quark-hadron duality - in other words, taking into account long-distance effects. To visualise this one can simply replace the internal quarks in Figure 1.3 by the corresponding hadrons, e.g. strange quarks by kaons; the hadronisation is non-perturbative. It is easy to see that there is asymmetry (i.e., SU(3) symmetry is broken) between $s\overline{s}$, which hadronises to states involving at least two kaons, and $d\overline{d}$, which can use two much lighter pions instead.

With this approach Ref. [13] finds that y can be as large as 1% within the Standard Model. This number rests mainly on the four-pseudoscalar S-wave intermediate states, where the phase-space asymmetry is on the order of 10%. For example, $4K$ is kinematically forbidden, while 4π occurs at the percent level ([11]). Since the total branching fractions of the 4P decays is in the region of 15% (Ref. [13] rounds to the nearest 5% and gets 10%, reflecting the 2001 knowledge of these branching fractions; the change strengthens the argument) one can multiply together and find 10% asymmetry in 10% of branching fractions giving a 1% total asymmetry, and hence a percent-level contribution to y. In Ref. [18] this argument is extended, by means of a dispersion relation derived from Heavy Quark Expansion Theory (HQET), to give a prediction for x as well; the conclusion drawn is that x is of the same order of magnitude as y, but of opposite sign.

The phase-space argument relies on there being either no SU(3) asymmetry in the matrix elements, or else that any such asymmetry does not cancel that in the phase space. Falk *et. al.* divide the D^0 decay channels by the daughter particles' parity properties, so that, for example, the $D^0 \to PP$ (pseudoscalar-pseudoscalar) class contains the channels $D^0 \to KK$, $D^0 \to \pi\pi$, and $D^0 \to K\pi$. They then consider the branching fractions within each class, and find that in most classes the phase-space asymmetry is in fact roughly cancelled by the measured branching fractions. Now, in the limit that there were infinitely many classes (or channels) each breaking SU(3) symmetry at roughly the same level, one would expect to get a net of zero mixing, since the direction of the symmetry breaking in each channel would be random, and cancel overall. But in fact, Ref. [13] finds that only the $D^0 \to 4P$ class has a large asymmetry after taking branching fractions into account - of order 10%. Since the

$D^0 \to 4P$ channels together have around 10% of the D^0 branching fraction, this asymmetry can lead to y as large as 1%.

Against this argument, it is worth recalling the phenomenon of 'precocious scaling' in deep inelastic scattering of electrons from protons; here duality holds (on average) well into the resonant regime near threshold, where there is no calculation explaining such agreement (Ref. [19]). If this is due to something other than random chance, perhaps a symmetry in physics we do not yet know, then it might extend to D^0 mixing as well and destroy the phase-space argument. (And branching fraction measurements do improve as time goes on; cancellations in 2004 numbers are not the end of the story.) Until such a reason is found, however, we can only say that percent-level mixing parameters is at best a weak signature of New Physics; that finding x and y with the same sign is a better (although still not certain) signature; and that the only unambiguous New Physics signature is *CP* violation - *CP* violation being small in the Standard Model. In particular, the weak phase is tiny in the two-by-two subset of the CKM matrix which (as shown above) governs D^0 mixing.

Chapter 3

The *BABAR* detector

This chapter describes the *BABAR* detector and the PEP-II accelerator. The discussion largely follows Ref. [20]. The coordinate system is shown in Figures 3.1 and 3.2. The z axis is defined to lie along the direction of the electron beam, the y axis straight up, and the x axis points towards the center of the PEP-II ring to make a right-handed coordinate system.

3.1 Cross-sections and $\Upsilon(4S)$ production

The PEP-II accelerator operated (for runs 1 through 6) in two main modes; *on-peak*, in which the center-of-mass (CM) energy is very near the $\Upsilon(4S)$ mass of 10.5794 GeV, and *off-peak*, in which the CM energy is 40 MeV lower and thus barely below the $b\overline{b}$ production threshold. In either case, the acceleration is asymmetric; the electron beam has a (lab) energy of 9.1 GeV, while the positron beam has energy 3 GeV (with rms spreads of respectively 5.5 MeV and 2.3 MeV), giving the CM system a boost of $\beta = 0.486$ in the lab frame. The beams collide head-on, with their collision axis offset from the detector z axis by about 20 mrad, to form the beam spot, the region in which events take place. The beam spot is a flattened, very elongated ellipsoid; the standard deviation of the coordinates of the e^+e^- collisions are a few micrometers in the y direction, slightly over a hundred micrometers in the x direction, and several *milli*meters in the z direction (along the beams).

$e^+e^- \rightarrow$	$b\bar{b}$	$c\bar{c}$	$s\bar{s}$	$d\bar{d}$	$u\bar{u}$	$\tau^+\tau^-$	$\mu^+\mu^-$	e^+e^-
Cross-section[nb]	1.05	1.30	0.35	1.39	0.35	0.94	1.16	~ 40

Table 3.1: Production cross-sections at the on-peak energy.

The cross-sections for $e^+e^- \rightarrow q\overline{q}$ at the on-peak energy are given in Table 3.1. By design, $b\overline{b}$ production is zero at the off-peak energy, permitting cross-checks of B meson measurements - anything visible in the off-peak data is certainly not a B meson. The other cross-sections remain essentially the same, since the quark masses involved are much smaller than the energy, and the change in CM energy between on-peak and off-peak is relatively tiny. For our purposes, the most interesting cross-section is that for $c\overline{c}$ production, because most $c\overline{c}$ events produce a D^* which decays very close to the beam spot, usually to a D meson and a slow pion. Although most B mesons do have a D^* in their decay chain, these D^*s are produced (because of the relatively long B lifetime, giving a (lab) decay length of a few hundred micrometers) some distance from the beam spot. Since our kinematic fit (see Chapter 4) assumes that the D^* was produced and decayed at the beam spot, D mesons from B decays produce results which are hard to interpret correctly. We therefore take steps to exclude such D mesons from the sample.

3.2 Tracking subdetectors

BABAR 's two innermost subdetectors are the Silicon Vertex Tracker (SVT) and the Drift Chamber (DCH), both of which are used to provide tracking information for charged particles. The SVT gives positions of decay vertices close to the beam spot and also measures the initial direction of tracks very accurately, which is important for Δm resolution. It consists of five layers of silicon strip detectors, covering the region from 20.1° forward (that is, at an angle of 20.1° to the electron beam) to 29.8° backwards. It has an error in vertex positions of 55 μm (for 1-GeV tracks) in the $x-y$ plane, and of 65 μm along the z-axis, corresponding to errors in lifetime of about 300 femtoseconds. This is an average for single tracks. Since this analysis uses a decay chain involving several tracks, the production and decay vertices (and

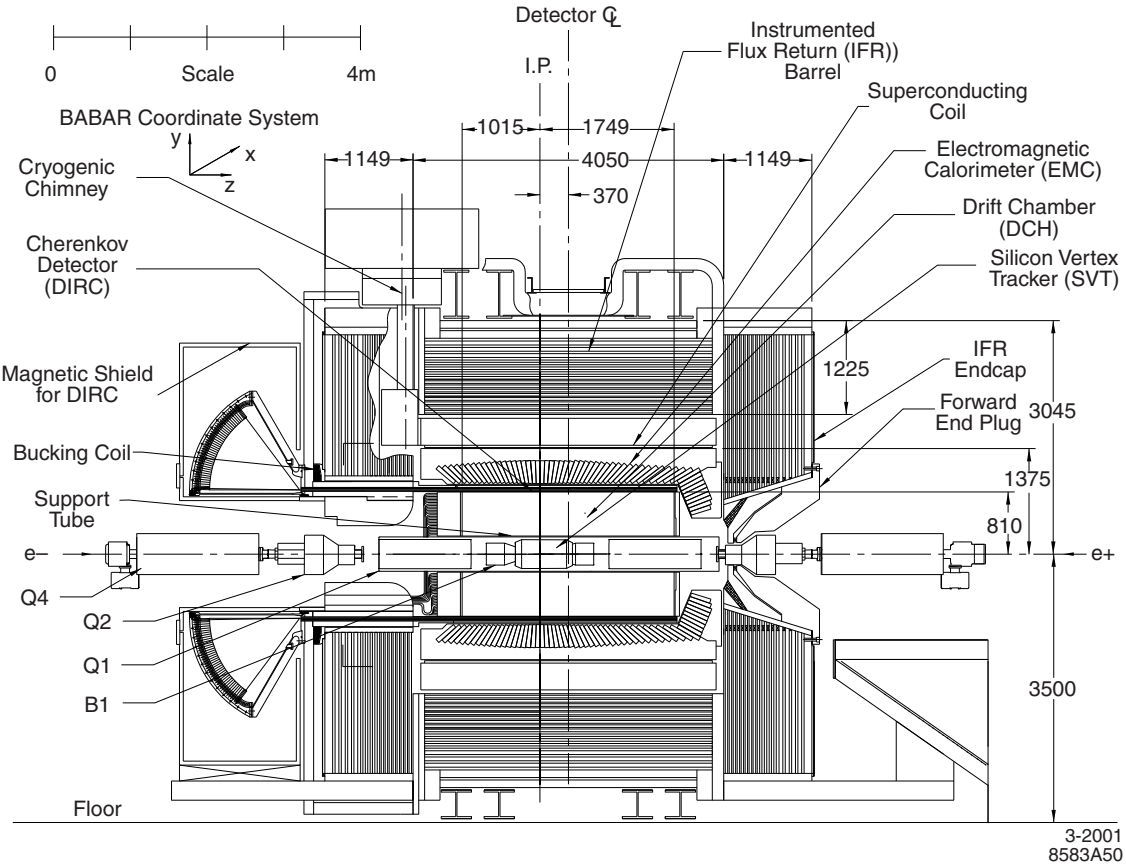

Figure 3.1: The *BABAR* detector, side view. Source: [20].

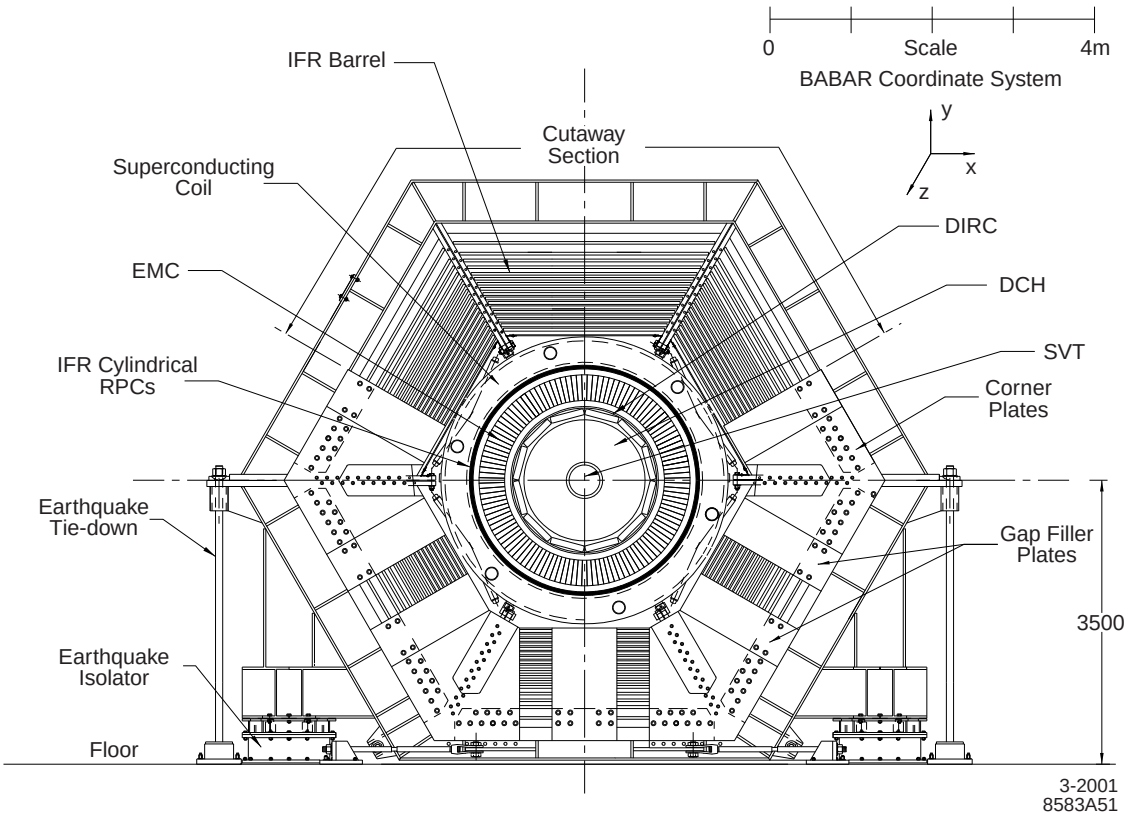

Figure 3.2: The *BABAR* detector, end view. Source: [20].

hence decay time) of the D^0 are better constrained than for a single track. The best-case errors in D^0 lifetime are therefore rather lower, and the peak (see Figure 6.9) is slightly lower.

The DCH is used to determine the momentum of particles and to aid in particle identification (PID) at low momenta through energy-loss (dE/dx) measurements. It consists of forty layers of detector cells in a helium-isobutane gas mix. As charged particles go through the gas, they ionise it; the resulting free electrons drift to the closest signal (anode) wire, providing a voltage pulse which can be read off to get time and position information; the amplitude of the pulse is used in determining dE/dx. The spatial resolution of individual hits varies with the distance from the closest wire, but averages about 0.2 millimeters. Calibration using cosmic rays, which pass through both sides of the detector, allowing comparison of two reconstructed tracks, shows that the azimuthal angle can be reconstructed with errors of 0.4 mrad. For tracks of momentum 1 GeV, the DCH measures transverse momentum with an accuracy of half a percent, and has an error in dE/dx of 7.5% (Ref. [20]).

3.3 DIRC

At energies above ∼750 MeV, dE/dx measurements no longer provide good K/π separation, as shown in Figure 3.3. The Detector of Internally Reflected Cherenkov light (DIRC) provides particle identification at higher energies, by measuring the angle at which Cherenkov photons are produced when particles pass through fused-silica bars. The fused silica has a refractive index of 1.473, giving a Cherenkov threshold of $\beta = 0.68$. For kaons this corresponds to an energy of roughly 700 MeV.

The Cherenkov photons are passed along the quartz bars by total internal reflection until they reach the Stand-Off Box, a water tank containing 11000 photomultiplier tubes (PMTs). This box acts as an extension volume, allowing measurements of the photon angles. The average photon multiplicity is a few tens, giving (along with the geometric resolution in the bars and PMTs) a per-track resolution in the Cherenkov angle of 2.5 mrad at 1 GeV ([20]).

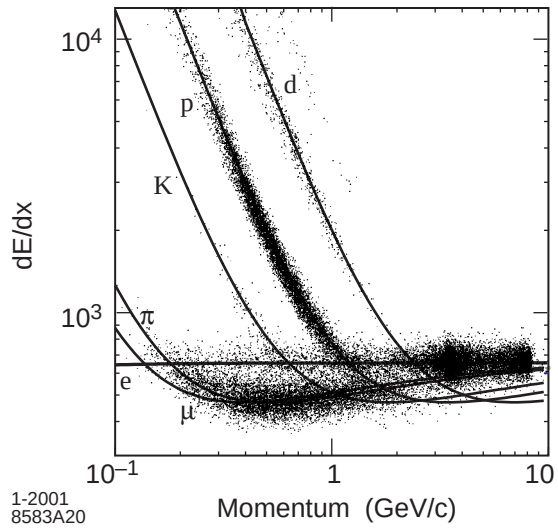

Figure 3.3: dE/dx measurements in the DCH as a function of track momentum; the curves show the Bethe-Bloch predictions. Source: [20].

This is sufficient for K/π separation at the four-sigma level out to energies of 4 GeV.

3.4 Outer detector layers

Surrounding the DIRC are the Electromagnetic Calorimeter (EMC) and the Instrumented Flux Return (IFR). The EMC consists of several thousand cesium iodide (CsI) crystals, laid so that their long axes point towards the beam spot. With the exception of muons, particles hitting these crystals will produce an electron-photon *shower*, that is, they will interact electromagnetically or strongly with the crystals, producing other particles going in the same general direction, which in turn generate other particles, until the initial energy is exhausted. Even neutral particles, which do not ionise the tracking detectors and do not produce Cherenkov photons, can be detected in this manner, although the spatial resolution is much poorer than the tracking detectors give. For example, to measure the momentum of a photon, all we can do is draw a line from the centroid of its EMC hit back to the beam spot. Since each crystal is 4.7×4.7 cm^2 in cross section, and since the photon may have come from a decay removed from the beam spot, this is much less accurate than tracking. (Note that hits can extend over several crystals, which improves the resolution slightly.) The

analysis described here does not have any neutral final-state particles, and can therefore rely on the inner detector systems for tracking; the two outer systems are used only for particle identification.

The outmost layer of *BABAR* is the IFR, which has a dual purpose: It consists of layers of iron, which guide the magnetic flux generated by the superconducting coil, and Limited Streamer Tubes (or Resistive Plate Chambers before the 2006 installation of LSTs), which detect particles which have passed through the other detector elements. These are mainly muons, which are both long-lived and minimum-ionising, and do not interact much with the detector material.

Chapter 4

Event selection

This chapter describes the reconstruction procedure, the selection of events, and the resulting event sample. Unless otherwise noted, charge conjugation is implied throughout. The study that led to the cut-based selection criteria was performed by Jordi G. Tico of the University of Barcelona.

4.1 Event reconstruction

The decay chain for this analysis is

$$D^{*+} \rightarrow D^0 \pi_s^+ \tag{4.1}$$

$$D^0 \rightarrow K_S^0 \pi^- \pi^+ \tag{4.2}$$

$$K_S^0 \rightarrow \pi^- \pi^+ \tag{4.3}$$

(and the charge-conjugated chain.) The end products observable in the detector, therefore, are five charged pions. We denote the pion from the D^* decay with the subscript 's', for slow, because the small phase space available limits its lab momentum to $\sim$450 MeV/c at most. The charge of this slow pion 'tags' the initial flavour of the D^0, since it is the same as the charge of the D^*. A positive slow pion indicates that the D meson was produced as a D^0, and a negative slow pion indicates the production of a $\overline{D}^0$.

The reconstruction of the decay chain begins with the K^0_S. We search for pairs of tracks (found by the basic *BABAR* reconstruction software) whose invariant mass (calculated using the momenta at the point of closest approach) is between 0.45 and 0.55 GeV/c^2. Such pairs are then fitted with the constraint that they come from a common vertex, and the invariant mass of the particles after this fit is required to be within 20 MeV/c^2 of the nominal K^0_S mass 497.67 MeV/c^2; they are then refitted with the further constraint that they have the nominal K^0_S mass. Note that this K^0_S mass constraint is also applied in the fits of the full decay chain mentioned below.

We combine each K^0_S candidate with pairs of oppositely charged tracks satisfying the `GoodTracksVeryLoose` requirements of *BABAR*, that is, their distance of closest approach to the beam spot must be less than 1.5 cm in the xy plane, and less than 10 cm in the z direction. We require that the invariant mass of the $K^0_S\pi^+\pi^-$ combination be within 70 MeV/c^2 of the nominal D^0 mass, 1864.5 MeV/c^2. We then fit them with the constraint of coming from a single point (and the two daughters of the kaon are still required to come from one point as before), and after this fit we require the $K\pi\pi$ mass to be within 40 MeV/c^2 of the nominal. Further, we require the CM momentum of the D^0 candidate to be greater than 2.2 GeV/c.

Finally, we create D^* candidates by combining the D^0 candidates above with another track satisfying the GoodTracksVeryLoose criterion, again fitting with the constraint of coming from a single point (and maintaining the previous single-point constraints). When the fit is complete, the difference Δm between the masses of the D^0 and D^* candidates is required to be between 130 and 170 MeV/c^2.

The geometric fit above is sufficient for a rough first cut, but for purposes of measuring D^0 lifetimes we use additional constraints. We create 'beam-constrained' D^* candidates by re-fitting the tracks with the additional constraint that the D^0 momentum must point back to the beam spot - in other words, there is a χ^2 term for the shortest distance between the beam spot and the line drawn from the D^0 decay vertex in the direction of its momentum. This additional constraint takes advantage of our knowledge of the production point of the

D^*, and therefore gives better estimates of the decay times and momenta. Then we create 'mass-constrained' candidates by imposing the requirement that the $K_s\pi\pi$ mass be equal to the nominal value 1864.5 MeV/c^2. This is in addition to the beam constraint. This mass-constrained fit is used to calculate the position of the event in the Dalitz plot, since the D^0 mass constraint automatically enforces the kinematic boundary arising from energy-momentum conservation.

4.2 Event selection

Given the list of D^* candidates above, we now begin applying additional selection criteria to improve the purity of our sample:

- The vertex probability (from the χ^2 and degrees of freedom) of the D^* vertex in the beam-constrained fit must be at least 0.01%. This eliminates bad fits, where large changes to the measured momenta are required to meet the constraints.
- Each pion is required to have a transverse momentum of at least 0.1 GeV/c. This ensures that they reach the drift chamber.
- The two pions from the D^0 decay are required to have at least two hits in the two innermost layers of the SVT, for accuracy in the measurement of their position.
- The slow pion is required to have at least one hit in the drift chamber.
- The mass of the K^0_S candidate is required to be within 9 MeV/c^2 of the nominal mass.
- The CM momentum of the D^0 candidate is required to be at least 2.5 GeV/c; this avoids D mesons originating in B decays.
- The reported error on the D^0 decay time (from the beam-constrained fit) must be less than 1 ps.

- The flight distance of the K^0_S, that is, the distance between the D^0 and K^0_S decay vertices, must be at least ten times its reported error. This, together with the next selection, strongly suppresses the decay $D^0 \to 4\pi$, as shown in Table 4.1.

- The angle between the K^0_S momentum and the vector from the D^0 to the K^0_S decay vertex (the K^0_S 'flight angle') must have a cosine greater than 0.99. This guards against combinatorial K^0_S mesons, made up from randomly combined pions.

- In events where more than one candidate meets all these criteria, the highest vertex probability is chosen.

The effects of these cuts are shown in Table 4.1.

4.3 Likelihood selector

In addition to the cut-based selection described above and developed by Jordi Tico, I have developed a likelihood-based selector in an attempt to improve the purity of the sample. The likelihood works as follows. First I apply all the cuts mentioned above, with the exception of those on the K^0_S mass, flight length, and flight angle, the D^0 CM momentum, and the χ^2 fit probability. These variables were chosen because they discriminate between signal and background, rather than between good and bad reconstructions. The distribution of the number of SVT hits, for example, is (approximately) the same for tracks in signal and background events, and hence this is not an appropriate variable for the likelihood; the cut is intended to suppress tracks with poor information, rather than background. Similar considerations apply to the other variables not used in the likelihood.

I split the resulting sample into even and odd events according to their timestamps. I then split the even and odd samples further into signal and background, taking the background events as those with a reconstructed D^0 mass below 1.81 GeV/c^2 or above 1.91 GeV/c^2, and signal as those within 11 MeV/c^2 of the nominal D^0 mass. (Figure 4.1 shows these bands.) Next, I create normalised histograms (even and odd) of the signal and background

CUTS	$B^0\overline{B^0}$	B^+B^-	$c\bar{c}$	uds
Reconstruction	1132099 (0.16)	595033 (0.09)	2072393 (0.15)	244680 (0.03)
$\lvert\vec{p}^*_{D^0}\rvert$	177698 (15.70)	101358 (17.03)	847803 (40.91)	80588 (32.94)
K_s mass width	177198 (99.72)	101030 (99.68)	845248 (99.70)	80343 (99.70)
$\lvert\vec{p}^{\pi_s}_t\rvert$	151108 (85.28)	88263 (87.36)	811330 (95.99)	75038 (93.40)
$\lvert\vec{p}_t\rvert$ for D^0 dau	142005 (93.98)	83409 (94.50)	769450 (94.84)	71753 (95.62)
$\lvert\vec{p}_t\rvert$ for K_s dau	129241 (91.01)	76100 (91.24)	731421 (95.06)	66965 (93.33)
Prob(D^* vertex)	78823 (60.99)	43839 (57.61)	466404 (63.77)	39761 (59.38)
# DCH hits for π_s	70232 (89.10)	38923 (88.79)	437855 (93.88)	35450 (89.16)
$cos(\theta_{K_s})$	54105 (77.04)	29255 (75.16)	361139 (82.48)	27016 (76.21)
$L^p_{K_s}/\sigma_L$	30864 (57.04)	14967 (51.16)	251758 (69.71)	14517 (53.73)
# SVT hits	29417 (95.31)	14298 (95.53)	238306 (94.66)	13787 (94.97)
σ_t	28807 (97.93)	14074 (98.43)	232666 (97.63)	13538 (98.19)
Absolute eff [%]	0.0040	0.0020	0.017	0.0016
N_{evt}	9952	4976	104732	15241

CUTS	$\tau^+\tau^-$	$D^0 \to 4\pi$	$D^0 \to K_sK_s$	signal
Reconstruction	320 ($8 \cdot 10^{-5}$)	200535 (0.96)	31336 (2.75)	3667263 (36.67)
$\lvert\vec{p}^*_{D^0}\rvert$	184 (57.50)	140666 (70.15)	22829 (72.85)	2553689 (69.63)
K_s mass width	183 (99.46)	140589 (99.95)	22821 (99.96)	2552265 (99.94)
$\lvert\vec{p}^{\pi_s}_t\rvert$	171 (93.44)	137706 (97.95)	22319 (97.80)	2503037 (98.07)
$\lvert\vec{p}_t\rvert$ for D^0 dau	163 (95.32)	135019 (98.05)	21373 (95.76)	2450253 (97.89)
$\lvert\vec{p}_t\rvert$ for K_s dau	157 (96.32)	129273 (95.74)	20939 (97.97)	2377578 (97.03)
Prob(D^* vertex)	71 (45.22)	82956 (64.17)	18569 (88.68)	2006538 (84.39)
# DCH hits for π_s	66 (92.96)	79328 (95.63)	17793 (95.82)	1923887 (95.88)
$cos(\theta_{K_s})$	43 (65.15)	44521 (56.12)	17714 (99.56)	1916303 (99.61)
$L^p_{K_s}/\sigma_L$	5 (11.63)	4404 (9.89)	17042 (96.21)	1838255 (95.93)
# SVT hits	1 (20.00)	4204 (95.46)	16130 (94.65)	1742803 (94.81)
σ_t	1 (100.00)	4165 (99.07)	15991 (99.14)	1730912 (99.32)
Absolute eff [%]	$3 \cdot 10^{-7}$	0.0200	1.40	17.3
N_{evt}	1	1845	7077	580000

Table 4.1: Absolute numbers and efficiencies (in percent) of the selection criteria, applied to different Monte Carlo samples. The efficiencies are shown relative to the sample after the previous selection. The efficiencies reported for the reconstruction are relative to the full Monte Carlo sample, which varies between 280 and 1040 fb^{-1} of luminosity. The final line shows the expected number of events in the data sample of 473.5 fb^{-1}. The numbers are shown for the $(m_{D^0}, \Delta m)$ window used in the step-1 fit (Section 6.2), $1.8245 < m_{D^0} < 1.9045$ GeV/c^2 and $143 < \Delta m < 149$ MeV/c^2, and are therefore roughly 20 times the expected numbers in the signal box, assuming flat distributions.

distributions of the likelihood variables, which are the mass, flight length, and flight angle of the K^0_S candidate, the D^0 CM momentum, and the chi-square probability of the beam-

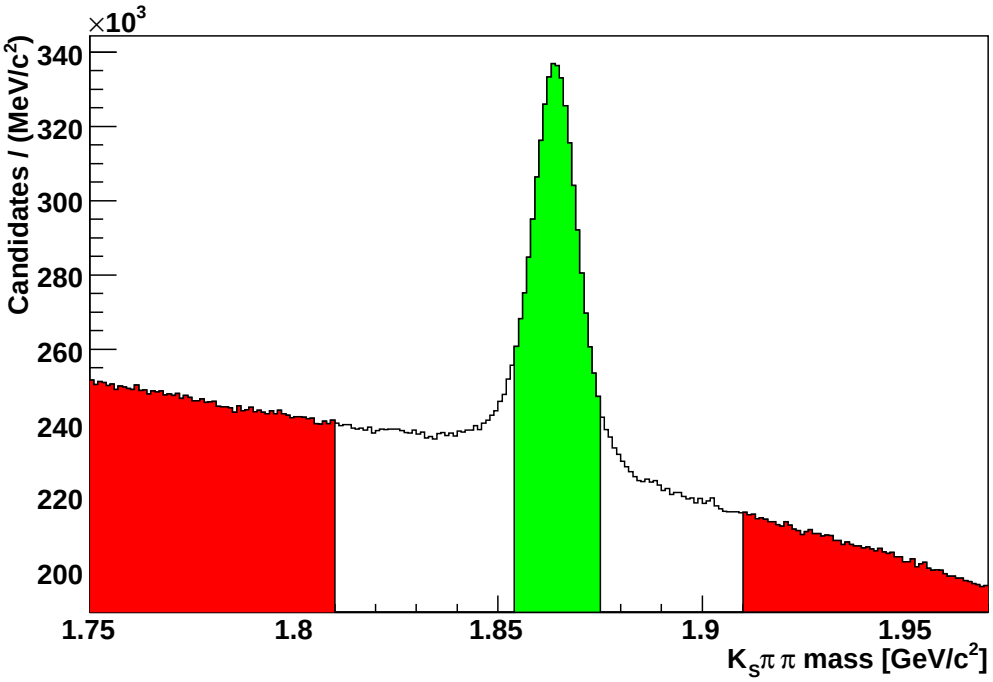

Figure 4.1: Distribution of the D^0 candidate mass, before any selection. The green area shows the signal band used for the likelihood; the red areas are the background sidebands.

constrained fit. These histograms are shown in Figures 4.2 through 4.6. Note that these distributions are made using data rather than Monte Carlo.

Now, for each D^* candidate, I determine whether it is even or odd. If it is even, I use the odd histograms in what follows, and vice-versa; this avoids using any candidate to create the likelihood it is selected by. For each of the five likelihood variables, I determine which histogram bin the candidate falls into, take the ratio of the signal to the background histogram in that bin, and sum the logarithms of these ratios to get the final likelihood. For example, suppose a candidate has D^0 momentum of 2.60 MeV/c, and that the corresponding signal histogram bin has (normalised) content 0.025 while the background histogram has 0.032. In other words, 3.2% of background falls into this bin, while only 2.5% of signal does. Then the likelihood from this variable, for this candidate, is $\ln(0.025/0.032) = -0.25$.

Figures 4.7 through 4.12 show comparisons of the D^0 mass distribution after selection by this likelihood, with the same distribution after the cut-based selection above. The two methods are very similar in their efficiency for the same purity. However, the likelihood

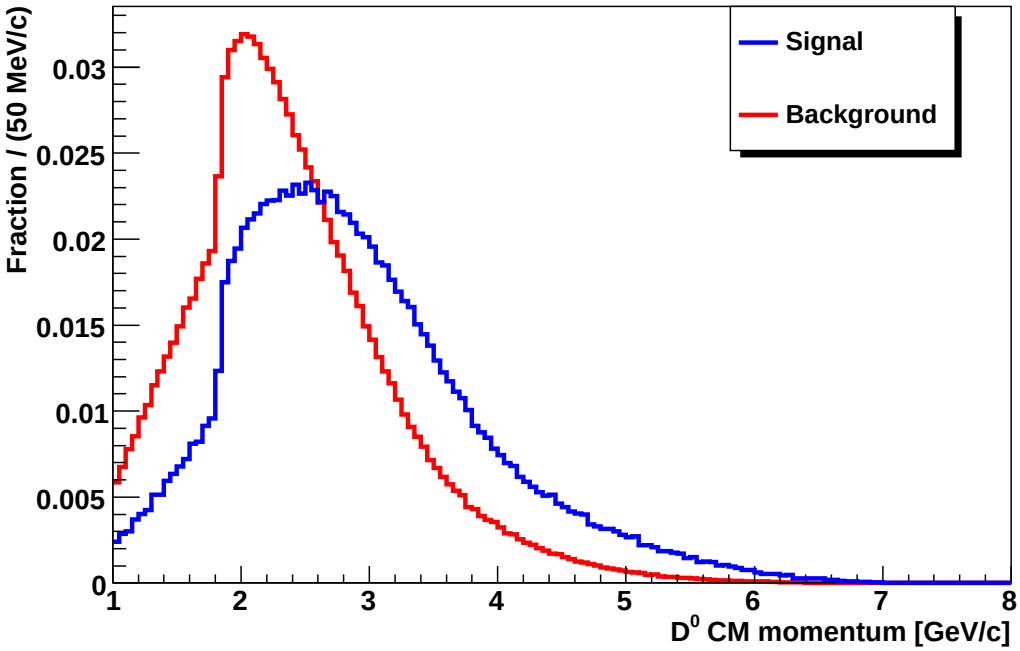

Figure 4.2: Signal and background distributions of the D^0 center-of-mass momentum.

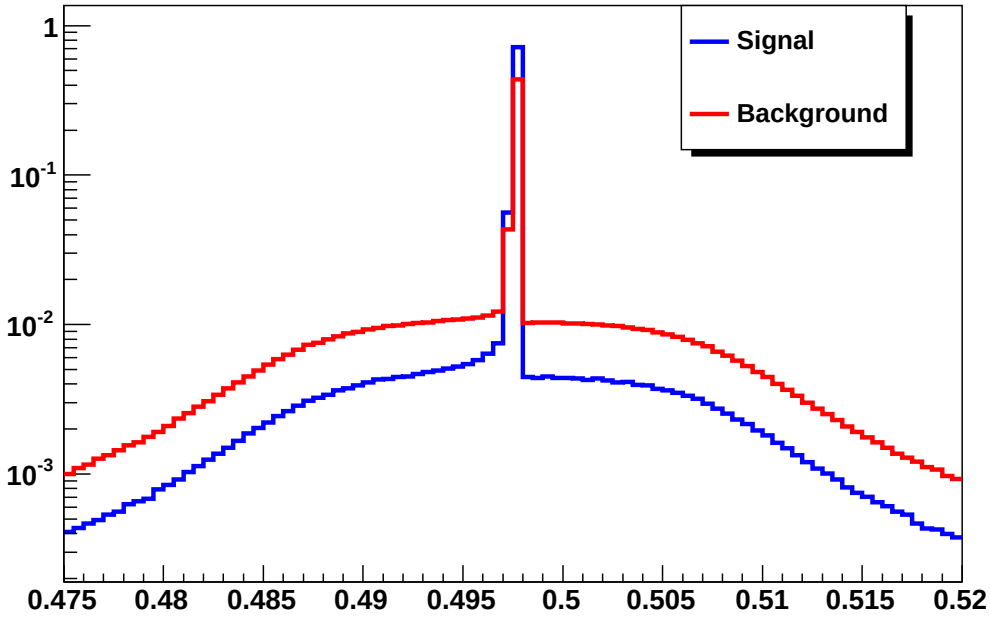

Figure 4.3: Signal and background distributions of the K^0_S mass.

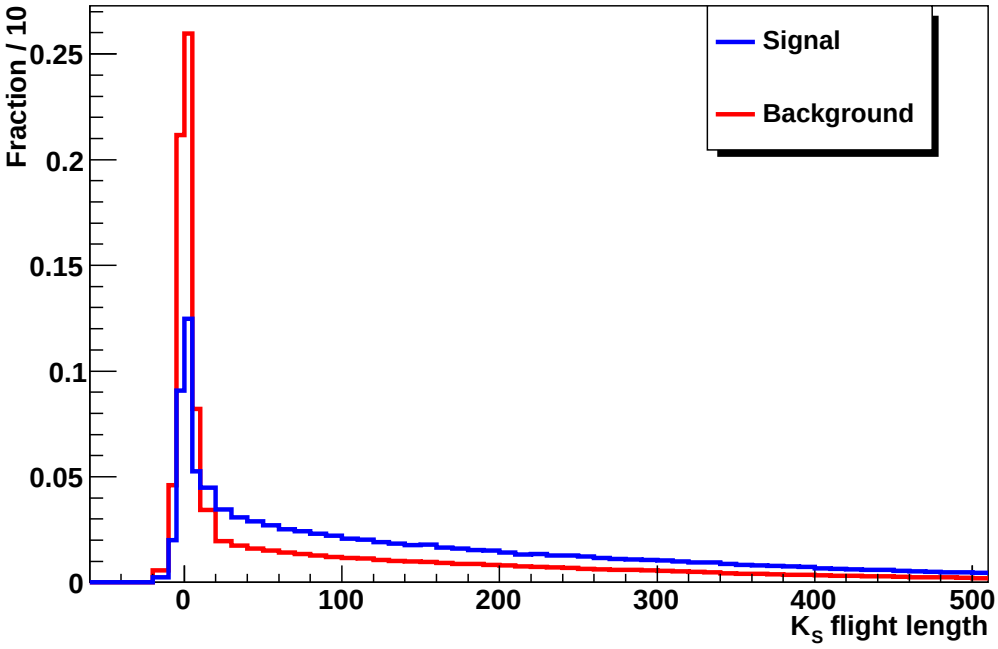

Figure 4.4: Signal and background distributions of the K_S^0 flight length (in units of the error). Note the finer binning around zero, intended to take advantage of the additional structure there.

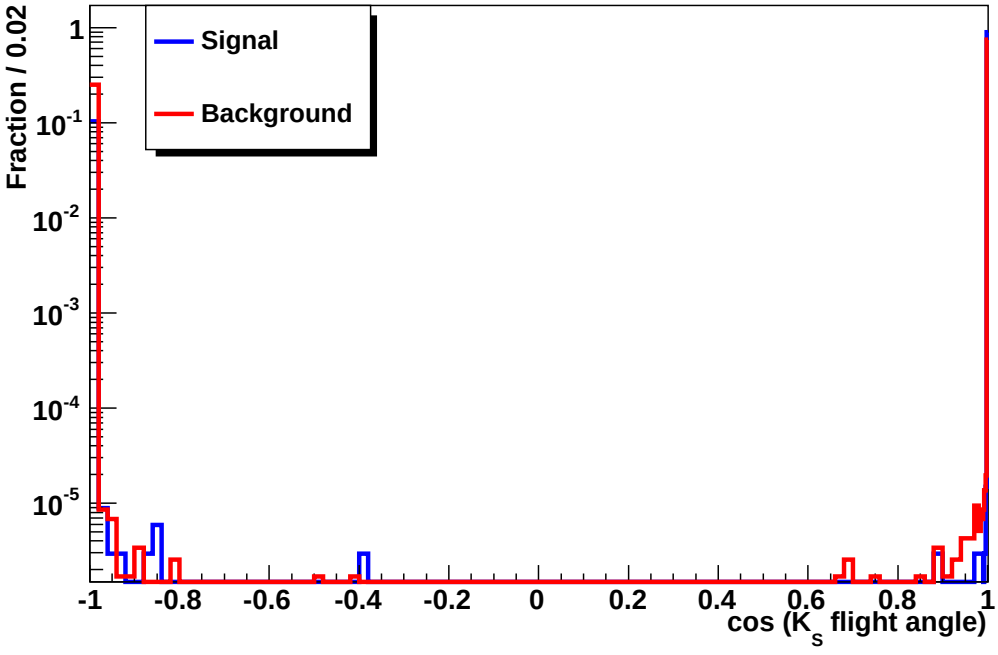

Figure 4.5: Signal and background distributions of the K_S^0 flight angle.

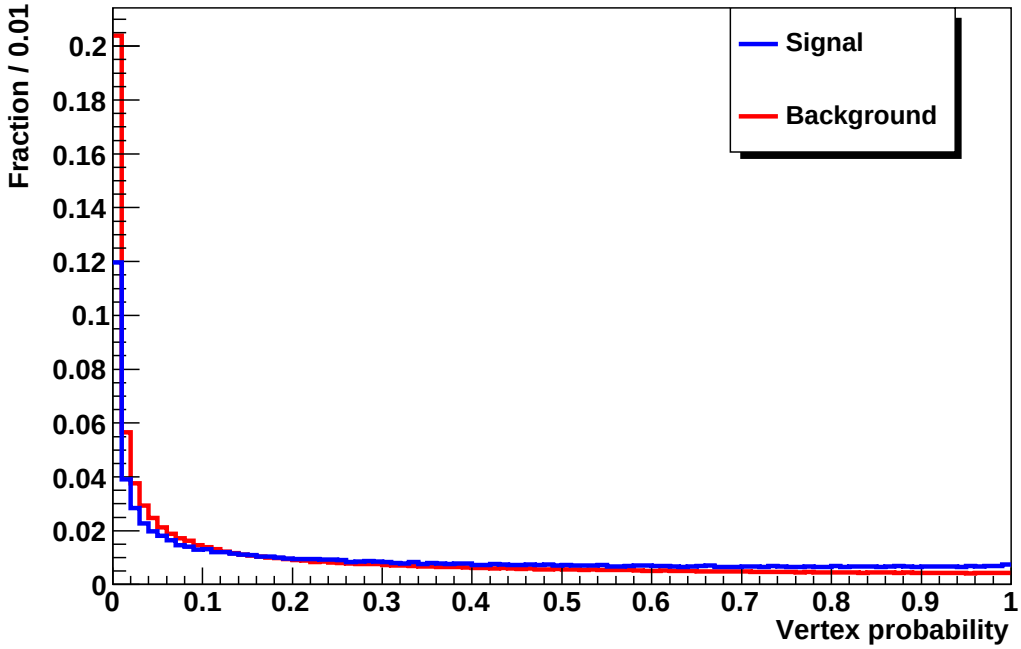

Figure 4.6: Signal and background distributions of the chi-square fit probability.

offers the advantage that it is easily 'tunable'. That is, we can change our efficiency/purity tradeoff very easily simply by selecting a different likelihood requirement. This allows us to optimise the total error by trading systematic for statistical error. For example, if we find that our uncertainty is dominated by systematics due to background, we can increase our statistical uncertainty a little by using a smaller, purer sample, and reduce the total uncertainty.

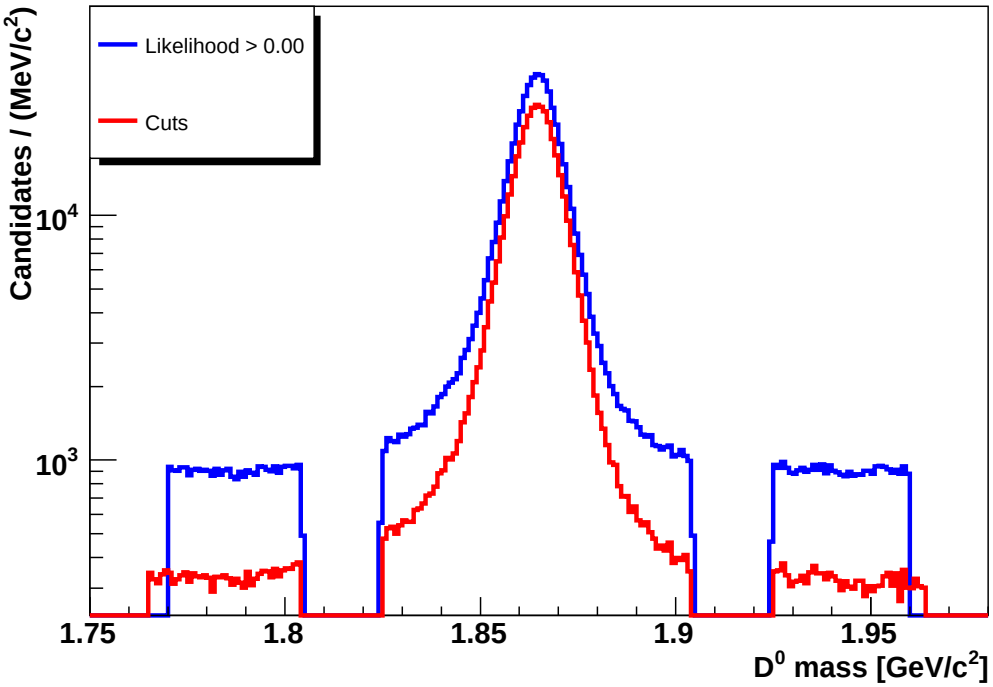

Figure 4.7: Data selected with cuts (red) and likelihood greater than 0 (blue).

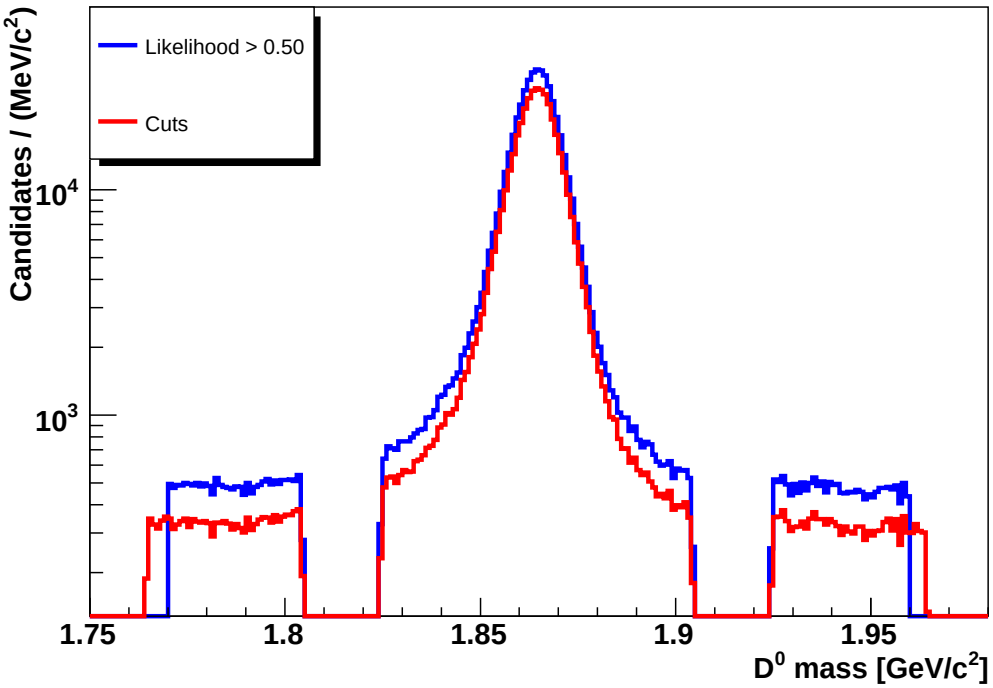

Figure 4.8: Data selected with cuts (red) and likelihood greater than 0.5 (blue).

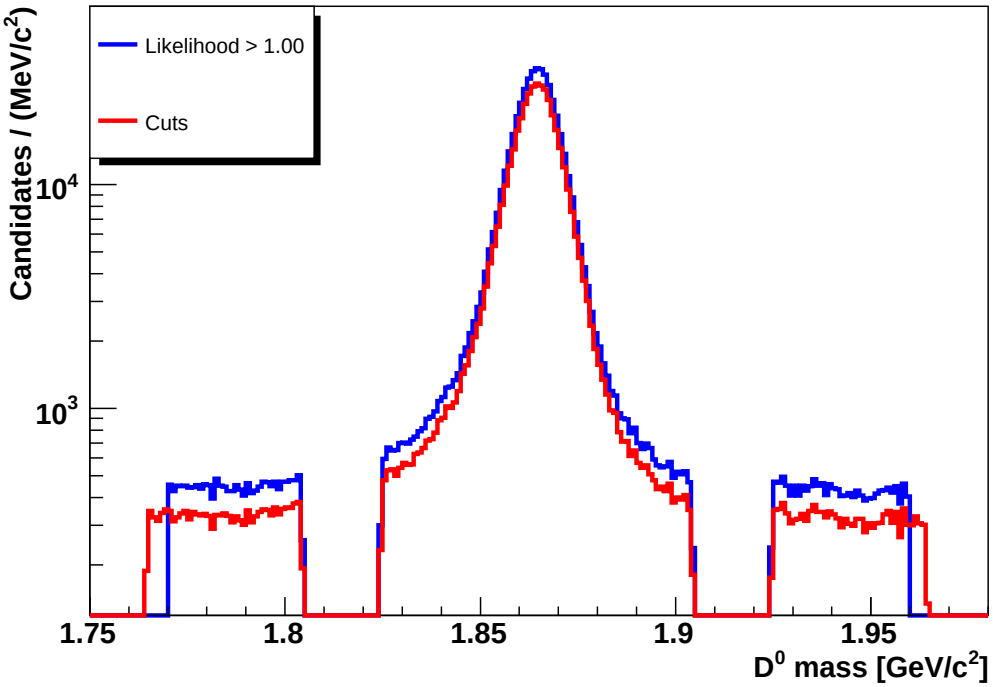

Figure 4.9: Data selected with cuts (red) and likelihood greater than 1 (blue).

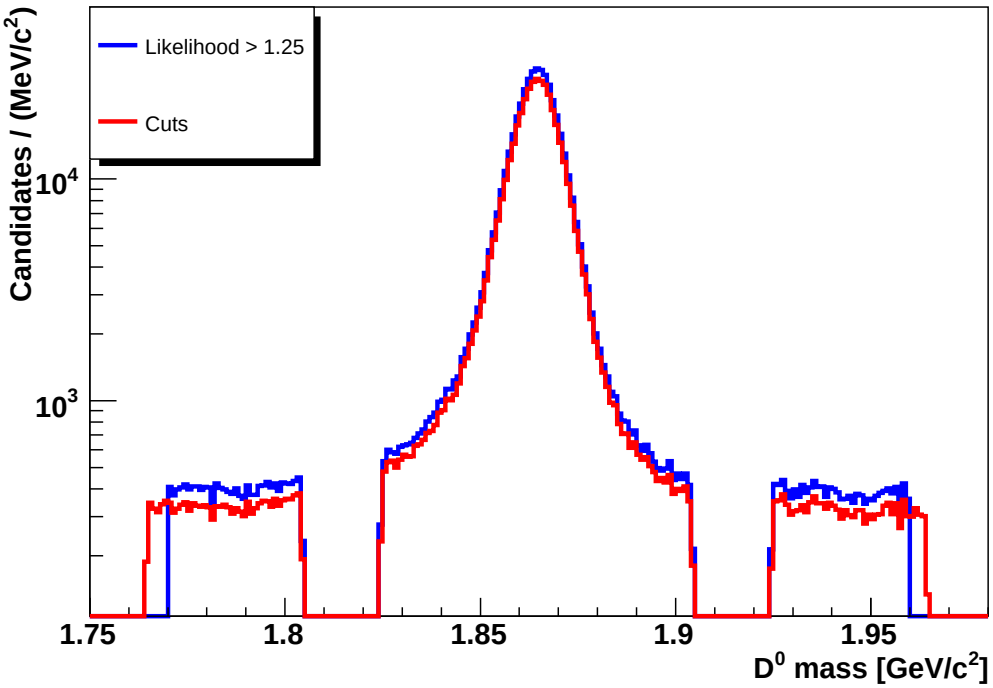

Figure 4.10: Data selected with cuts (red) and likelihood greater than 1.25 (blue).

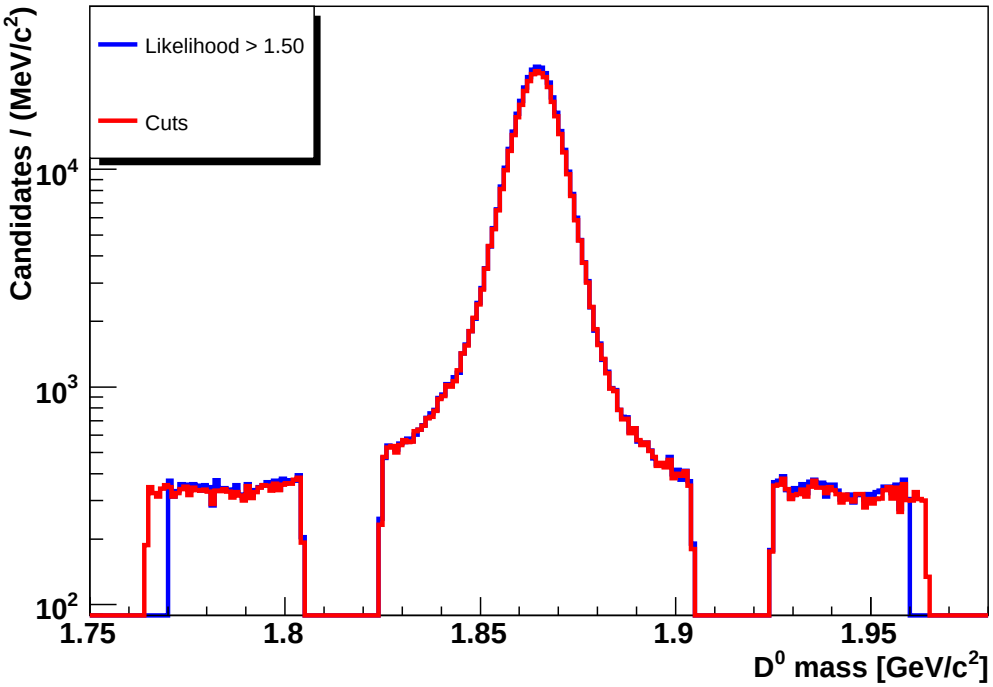

Figure 4.11: Data selected with cuts (red) and likelihood greater than 1.5 (blue).

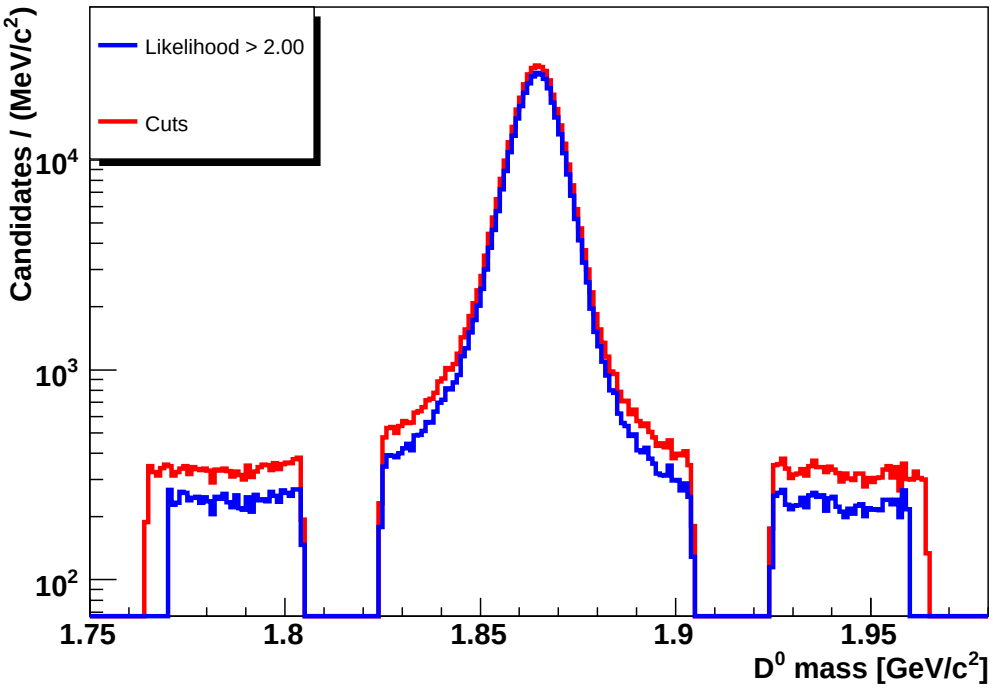

Figure 4.12: Data selected with cuts (red) and likelihood greater than 2 (blue).

Chapter 5

D^0 decay model

This chapter describes the model we use to describe the distribution of events in the Dalitz plot.

5.1 Formalism

In a three-body decay, $A \to B + C + D$, the amplitude is proportional to a phase-space factor:

$$d\Gamma = \frac{|\mathcal{M}|^2}{16(2\pi)^5 M_A} \,\mathrm{d}E_B \,\mathrm{d}E_C \,\mathrm{d}\alpha \,\mathrm{d}\cos\beta \,\mathrm{d}\gamma \tag{5.1}$$

([21]), where the Euler angles α, β, γ specify the orientation of the three-particle system in the rest frame of the mother. Define $p_{ij} = p_i + p_j$, and $m_{ij}^2 = p_{ij}^2$. We have

$$p_{BC}^2 + p_{BD}^2 + p_{CD}^2 = 2p_B^2 + 2p_C^2 + 2p_D^2 + 2p_B p_C + 2p_B p_D + 2p_C p_D \tag{5.2}$$

$$m_{BC}^2 + m_{BD}^2 + m_{CD}^2 = (p_B + p_C + p_A)^2 + p_B^2 + p_C^2 + p_D^2 \tag{5.3}$$

$$= m_A^2 + m_B^2 + m_C^2 + m_D^2 \tag{5.4}$$

$$p_{BC}^2 = (p_A - p_D)^2 \tag{5.5}$$

and in the rest frame of A, where $\vec{p}_A = \vec{0}$,

$$m_{BC}^2 = m_A^2 + m_D^2 - 2m_A E_D. \tag{5.6}$$

By cyclically permuting the indices,

$$m_{BD}^2 = m_A^2 + m_C^2 - 2m_A E_C \tag{5.7}$$

$$m_{CD}^2 = m_A^2 + m_B^2 - 2m_A E_B \tag{5.8}$$

and hence

$$dE_B = -(1/2m_A)dm_{CD}^2 \tag{5.9}$$

$$dE_C = -(1/2m_A)dm_{BD}^2. \tag{5.10}$$

Substituting this into 5.1, and integrating over the Euler angles, we get

$$d\Gamma = \frac{\overline{|\mathcal{M}|^2}}{32(2\pi)^3 M_A^3}\,\mathrm{d}m_{CD}^2\,\mathrm{d}m_{BD}^2 \tag{5.11}$$

where $\overline{|\mathcal{M}|^2}$ indicates averaging over the spin states of A. We can therefore see that plotting the number of events as a function of m_{CD}^2 and m_{BD}^2 (or either of the other two pairs of squared two-daughter masses) shows us the spin-averaged squared magnitude directly. This is a Dalitz plot.

Underlying the amplitude contributing to what we see in the Dalitz plot are strong-force interactions between quarks, both short-range, i.e. internal to the D^0, and long-range, between the daughter particles before they are fully separated. These interactions are beyond our ability to calculate; we must therefore turn to models to explain what we see. One such is the *isobar model*, in which we think of the amplitude as a sum of amplitudes for quasi-two-body decays. For example, seeing that the $D^0 \to K_S^0\pi\pi$ Dalitz plot has a strong band near $m_{K_S^0\pi^-} = 0.892$ GeV/c^2 (see Figure 5.1), we can think of this as being due to the decay

chain $D^0 \to K^{*-}\pi^+$, $K^{*-} \to K^0_S\pi^-$. In this model we consider the matrix element as a sum of complex Breit-Wigner functions with different complex coefficients c_j:

$$\mathcal{M} \;=\; \sum_j c_j \mathcal{B}(m^2_{BC}, m^2_{BD}; m_j, \Gamma_j) \tag{5.12}$$

where $\mathcal{B}$ is the Breit-Wigner function described in Eqn 2.13 (including the spin and form factors), and m_j and Γ_j are the mass and width of resonance j. Since the coefficients are complex and the Breit-Wigner phase changes across the Dalitz plot, resonances interfere with each other.

The isobar model is easy to interpret, and it is also easy to compare isobar results with other types of experiment where resonances appear. Its weakness is that in some circumstances it can violate unitarity, a phrase which requires some explanation and a diversion into scattering theory. Consider the decay $D^0 \to K^0_S\pi^+\pi^-$, whose kinematics we parametrise in the two masses $m_{K\pi^+}$ and $m_{K\pi^-}$. If we imagine time-reversing the K^0_S while holding the CM energy constant, we get instead a scattering experiment, $D^0K^0_S \to \pi^+\pi^-$, whose kinematics and dynamics are exactly the same as for the decay. We may therefore apply results from scattering theory to our analysis of the decay. In particular, we may express the amplitude as an infinite sum over partial waves, that is, amplitudes for particular states of the $\pi\pi$ system with given angular momentum. Such a sum is an exact solution to either the scattering or the decay problem. Now, if instead of time-reversing the K^0_S, we had time-reversed the positive pion (which also reverses its charge), we would have the scattering problem $D^0\pi^- \to K^0_S\pi^-$, which we can solve in terms of an infinite sum over the $K^0_S\pi^-$ states. Because both these sums contain the solution to the decay problem, there exists some basis transformation to go from one to the other. In other words, all the features of the $\pi\pi$ partial-wave expansion are contained in the $K^0_S\pi$ expansion, including the $\pi\pi$ resonances such as the $\rho(770)$.

Now, in the isobar model, we are taking the first few terms of each of the three possible expansions - in particular, we stop at resonances with spin 2. But there exists some combination of terms from the $\pi\pi$ expansion which gives us each resonance of the other two

expansions; we are therefore double-counting some part of each sum of resonances. For example, the K^{*+} in this decay amplitude can be expressed as some sufficiently large sum over the $\pi\pi$ resonances, and this sum includes the $\rho(770)$; therefore, by counting the $\rho(770)$ and the K^{*+} separately, we have counted the $\rho(770)$ more than once. This is what is meant by violating unitarity. However, while this is theoretically unsatisfying, it does not prevent the isobar model from being a reasonable description of data with finite statistics. The reason for this is that, like adding sine curves to make a square wave, it takes a lot of $\pi\pi$ terms to make a K^{*+} resonance. Hence, while we've counted the $\rho(770)$ more than once, we haven't counted it very much more, and the isobar model gives us a function which describes the Dalitz plot - which is the test of any model, as long as we keep in mind that the model is not the physics.

5.2 Isobar model

The resonances used in the present analysis are shown in Table 5.1, along with their phases and amplitudes (relative to the $\rho(770)$) as measured by Step 2 of our fit (described in Section 6.4). Figure 5.1 shows a Dalitz plot of Monte Carlo events generated according to this model, which can be compared to the Dalitz plot of real data shown in Figure 5.2. Notice the trough, relative to the surrounding area, along the wrong-sign K^* band. In the isobar model we can understand this by looking at the Feynman diagrams of the underlying quark reactions. The doubly Cabibbo-suppressed reaction $D^0 \to K^{*-}\pi^+$ shown in Figure 5.3(b) has Cabibbo couplings of $-\sin^2\theta_C$, while the the Cabibbo-favoured $D^0 \to K^{*+}\pi^-$ shown in Figure 5.3(a) has $\cos^2\theta_C$. These processes therefore interfere destructively, and the Cabibbo-suppressed resonance shows up as a trough in the number of events. (Alternatively we may note that their phases, respectively 2.341 and -0.841 radians, are almost exactly π radians apart - in other words, the resonances are almost perfectly out of phase.) Thus quantum-mechanical interference is manifestly visible in this plot.

Resonance	$\Re c_j$	$\Im c_j$	Mass [GeV/c^2]	Width [GeV/c^2]	Spin	Type
$\pi^+\pi^-$						
$\rho(770)$	1.000	0.000	0.776	0.150	1	CP-odd
$f_0(1370)$	-2.165	3.624	1.434	0.173	0	CP-even
$f_0(980)$	-0.424	-0.236	0.975	0.044	0	CP-even
$f_2(1270)$	0.218	-0.133	1.275	0.185	2	CP-even
$\omega(782)$	-0.025	0.039	0.783	0.008	1	CP-odd
σ	-1.556	-0.932	0.528	0.512	0	CP-even
σ'	-0.274	-0.054	1.033	0.099	0	CP-even
$K^0_S\pi^-$						
$K^*(892)^-$	-1.164	1.068	0.894	0.046	1	Flavour
$K^*_0(1430)^-$	1.621	1.068	1.459	0.175	0	Flavour
$K^*_2(1430)^-$	1.155	-0.773	1.426	0.099	2	Flavour
$K^*(1680)^-$	-1.697	0.128	1.677	0.205	1	Flavour
$K^0_S\pi^+$						
$K^*(892)^+$	0.106	-0.119	0.894	0.046	1	Flavour
$K^*_0(1430)^+$	0.149	0.090	1.459	0.175	0	Flavour
$K^*_2(1430)^+$	0.141	-0.165	1.426	0.099	2	Flavour
$K^0_S\pi^+\pi^-$						
NR	0.849	0.894	0.000	0.000	0	CP-even

Table 5.1: Complex amplitudes, relative to $\rho(770)$, of the resonances used in our Monte Carlo.

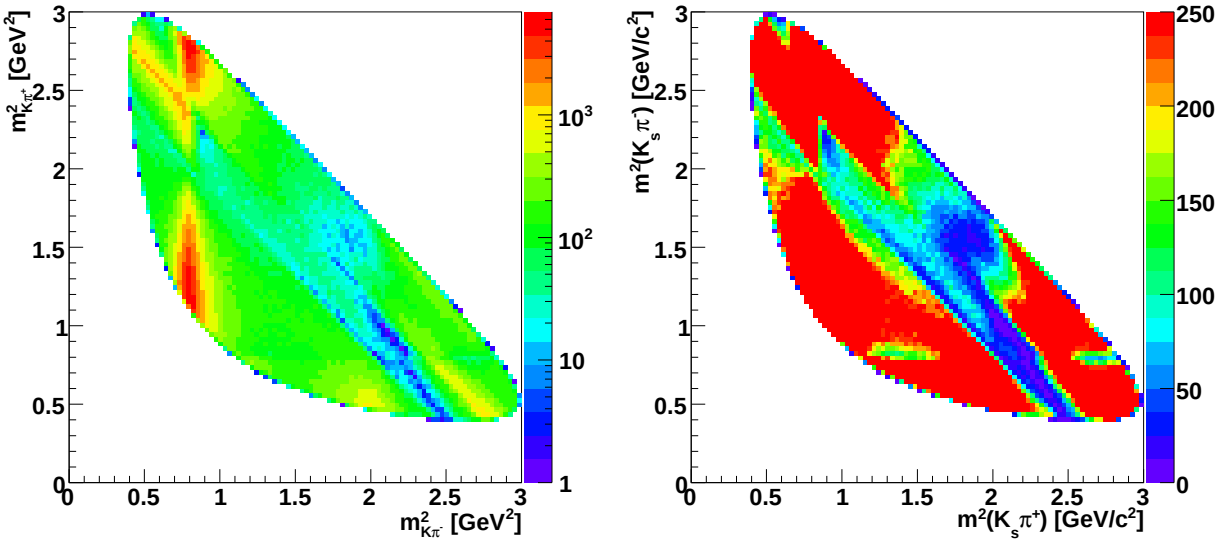

(a) Logarithmic

(b) Capped linear

Figure 5.1: Dalitz plot from signal Monte Carlo, showing the generated distribution. The left-hand plot shows the full range on a logarithmic scale; the right-hand one has a linear scale and is capped at 250 events, in order to bring out the variation in the scarcely populated areas.

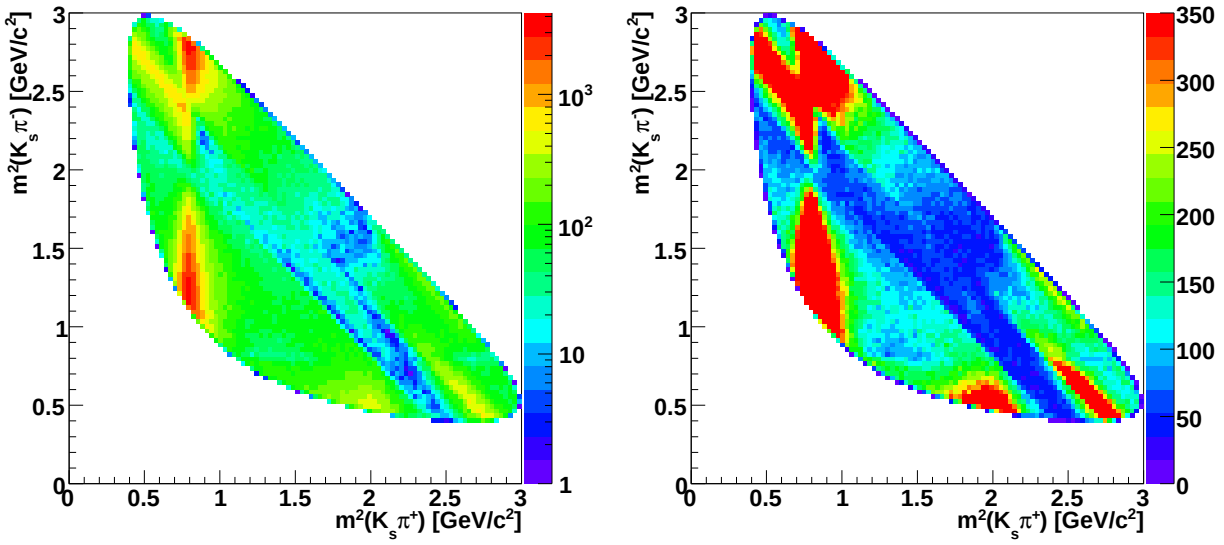

(a) Logarithmic (b) Capped linear

Figure 5.2: Dalitz plot from data. The left-hand plot shows the full range on a logarithmic scale; the right-hand one has a linear scale and is capped at 350 events, in order to bring out the variation in the scarcely populated areas.

The non-resonant component denoted 'NR' is taken as uniform across the entire Dalitz plot. However, from (e.g.) Ref. [22] it is clear that the non-resonant $\pi\pi$ S-wave has more structure than this. We model this structure by including the two σ resonances, which are not supposed to be real particles in the sense that a K^* is real, but rather are a convenient way of introducing additional structure to the nonresonant term. Their justification is empirical: The fit works better with σ resonances than without.

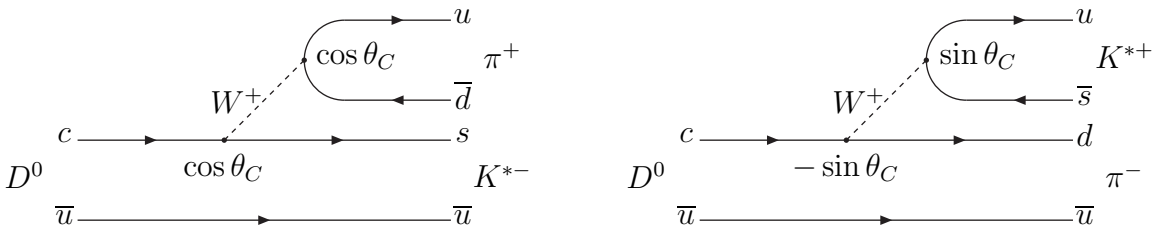

(a) Right-sign (b) Wrong-sign

Figure 5.3: Feynman diagrams of the right- and wrong-sign $D^0 \to K^*\pi$ processes.

5.3 K-matrix model

The K-matrix description avoids the violation of unitarity in individual partial waves (e.g. the $\pi\pi$ S-wave) encountered in the isobar model. In the following, which follows Ref. [23], the difference between scattering processes and decays is ignored. For example, we consider the decay of D^0 to $K^0_S\pi^+\pi^-$ to have dynamics equivalent to a scattering of K^0_S from a $\pi\pi$ bound state, with the mass of the $K^0_S\pi\pi$ system equal to the D^0 mass. This allows us to use arguments from scattering theory.

We begin by writing the amplitude in terms of a transition matrix T:

$$\begin{aligned} \mathcal{A} &= \langle f|S|i\rangle & (5.13)\\ &= \langle f|1+2iT|i\rangle. & (5.14) \end{aligned}$$

Here $|i\rangle$ is the initial state and $|f\rangle$ is the final state. Because the scattering matrix S is unitary (or else probability is not conserved), $SS^\dagger = S^\dagger S = I$, we have

$$\begin{aligned} I &= SS^\dagger & (5.15)\\ I &= (I+2iT)(I+2iT)^\dagger & (5.16)\\ I &= I+2iT-2iT^\dagger+4TT^\dagger & (5.17)\\ 4TT^\dagger &= 2iT^\dagger-2iT & (5.18)\\ 2iTT^\dagger &= T-T^\dagger & (5.19)\\ 2iT^\dagger &= I-T^{-1}T^\dagger & (5.20)\\ -2iT &= I-T\left(T^{-1}\right)^\dagger & (5.21)\\ -2iI &= T^{-1}-\left(T^{-1}\right)^\dagger & (5.22)\\ \left(T^{-1}\right)^\dagger - iI &= T^{-1}+iI & (5.23)\\ \left(T^{-1}+iI\right)^\dagger &= T^{-1}+iI \equiv K^{-1}. & (5.24) \end{aligned}$$

This implies that the K-matrix is Hermitian, and since both S and T are invariant under

time reversal, it is also symmetric; hence it can be chosen to be real. Multiplying this by K from the left and T from the right, and vice-versa, gives respectively

$$\begin{aligned} K + iKT &= T & (5.25)\\ K + iTK &= T & (5.26)\\ KT &= TK & (5.27) \end{aligned}$$

which shows that K and T commute; and solving for T,

$$\begin{aligned} K &= T(I - iK) = (I - iK)T & (5.28)\\ T &= K(I - iK)^{-1} = (I - iK)^{-1}K. & (5.29) \end{aligned}$$

Since K is real, we have

$$\begin{aligned} \Re(T) &= \Re\left(K + iKT\right) & (5.30)\\ &= K\left(I + \Re\left(i\left(\Re(T) + i\Im(T)\right)\right)\right) & (5.31)\\ &= K\left(I - \Im(T)\right) & (5.32)\\ \Im(T) &= \Im\left(K + iKT\right) & (5.33)\\ &= \Im(K) + K\Im\left(i\left(\Re(T) + i\Im(T)\right)\right) & (5.34)\\ &= K\Re(T) & (5.35) \end{aligned}$$

which implies

$$\begin{aligned} \Re(T) &= K(I + K^2)^{-1} = (I + K^2)^{-1}K & (5.36)\\ \Im(T) &= (I + K^2)^{-1}K^2 = K^2(I + K^2)^{-1}. & (5.37) \end{aligned}$$

Recalling that the relation $T - T^\dagger = 2iTT^\dagger$ was derived from the requirement of unitarity,

we can see that unitarity now reduces to

$$\Im(T) \;=\; TT^* = T^*T. \tag{5.38}$$

Having defined this K-matrix, the next step is to demonstrate its usefulness. First consider the case when the process is dominated by a single spinless resonance. In this case we know that the scattering matrix is simply $S = e^{2i\delta}$, and the transition amplitude is given by $T = \sin\delta e^{i\delta}$, with δ the phase shift. (Notice that the Argand diagram of T, that is, the plot of T's position in the complex plane as a function of the mass, is a circle of radius $1/2$, as one can easily show by calculating $|T - i/2|^2$.) Hence

$$\begin{aligned}
K^{-1} &= T^{-1} + i && (5.39)\\
&= \frac{1 + ie^{i\delta}\sin\delta}{e^{i\delta}\sin\delta} && (5.40)\\
&= \frac{1 + i(\cos\delta + i\sin\delta)\sin\delta}{(\cos\delta + i\sin\delta)\sin\delta} && (5.41)\\
&= \frac{1 + i(\cos\delta + i\sin\delta)\sin\delta}{\sin\delta\cos\delta + i\sin^2\delta} && (5.42)\\
&= \frac{(1 + i\sin\delta\cos\delta - \sin^2\delta)(\sin\delta\cos\delta - i\sin^2\delta)}{\sin^2\delta\cos^2\delta + \sin^4\delta} && (5.43)\\
&= \frac{(\cos^2\delta + i\sin\delta\cos\delta)(\sin\delta\cos\delta - i\sin^2\delta)}{\sin^2\delta} && (5.44)\\
&= \frac{\sin\delta\cos^3\delta - i\sin^2\delta\cos^2\delta + i\sin^2\delta\cos^2\delta + \sin^3\delta\cos\delta}{\sin^2\delta} && (5.45)\\
&= \frac{\sin\delta\cos\delta(\cos^2\delta + \sin^2\delta)}{\sin^2\delta} && (5.46)\\
&= \cot\delta && (5.47)\\
K &= \tan\delta. && (5.48)
\end{aligned}$$

It follows that K has a pole when $\delta = \pi/2$, in other words at the resonance mass.

Next we consider the more difficult multi-resonance case. It is convenient first to introduce Lorentz-invariant forms for T and K, denoted $\hat{T}$ and $\hat{K}$, by multiplication with the phase-

space terms for the final and initial states:

$$S = I + 2i\sqrt{\rho}\hat{T}\sqrt{\rho} \tag{5.49}$$

where the phase-space matrix ρ is the diagonal matrix $\rho_{ii} = 2q_i/m$, with q_i the threshold momentum for channel i. We then find

$$\hat{K}^{-1} = \hat{T}^{-1} + i\rho \tag{5.50}$$

$$\hat{T} = \hat{K}(I - i\rho\hat{K})^{-1}. \tag{5.51}$$

We can now define the elements of K-matrices in processes dominated by multiple resonances:

$$\hat{K}_{ij} = \sum_{\alpha} \frac{g_{\alpha i}(m) g_{\alpha j}(m)}{(m_\alpha^2 - s)\sqrt{\rho_i \rho_j}} \tag{5.52}$$

where the sum is over poles of mass m_α and the residue functions g are given by

$$g_{\alpha i}^2(m) = m_\alpha \Gamma_{\alpha i}(m). \tag{5.53}$$

The widths $\Gamma_{\alpha i}$ are given in terms of barrier factors,

$$\Gamma_{\alpha i}(m) = \left(B_{\alpha i}^l\right)^2 = \gamma_{\alpha i}^2 \Gamma_\alpha^0 \rho_i \left(\frac{F_l(q_i)}{F_l(q_\alpha)}\right)^2 \tag{5.54}$$

where the F_l are (for this analysis) the spin damping factors given in Chapter 2 and the γ are real constants subject to the normalisation constraint $\sum_i \gamma_{\alpha i}^2 = 1$. As a practical matter, we take for our fit parameters 'base residue functions'

$$g_{\alpha i}^0 = \gamma_{\alpha i}\sqrt{m_\alpha \Gamma_\alpha^0} \tag{5.55}$$

and thus express the residue functions more simply as

$$g_{\alpha i}(m) \;=\; g^0_{\alpha i} B^l_{\alpha i} \sqrt{\rho_i}. \tag{5.56}$$

From this we see that

$$\hat{K}_{ij} \;=\; \sum_\alpha \frac{g^0_{\alpha i} g^0_{\alpha j} B^l_{\alpha i} B^l_{\alpha j}}{m^2_\alpha - s}. \tag{5.57}$$

The fit parameters for a K-matrix model, then, are the pole masses m_α and the base residue functions. These correspond in some sense to the resonance masses and widths of an isobar model, but do not have an intuitive physical interpretation.

Up to this point all has been general, but now we turn to the application to Dalitz-plot analysis of $D^0 \to K_s\pi\pi$. Here the goal is not to preserve unitarity, but rather to have a second description of the Dalitz plot, which we can use to check the dependence of the mixing measurement on the model. We therefore describe only the $\pi\pi$ S-wave by a K-matrix method, and add this coherently to the isobar model description of the $K^0_S\pi^+$ and $K^0_S\pi^-$ resonances. The production part of the decay process is parametrised by a production vector P, and the amplitude becomes

$$F_i \;=\; (I - iK\rho)^{-1}_{ij} P_j. \tag{5.58}$$

Here the matrix involving K may be considered as a scattering propagator, carrying the initially produced states from P to the final state; this relies on the assumption that the $\pi\pi$ system does not interact with the K^0_S after the production. For this analysis we take the production vector as

$$P_j(s) \;=\; \left(f^{prod}_{1j} \frac{1 - s^{prod}_0}{s - s^{prod}_0} + \sum_\alpha \frac{\beta_\alpha g^\alpha_j}{m^2_\alpha - s} \right). \tag{5.59}$$

We take the channels j as $\pi\pi$, KK, $\eta\eta$, $\eta'\eta'$, and 4π. The K-matrix elements are (from [24],

m_α	$g_{\pi\pi}$	g_{KK}	$g_{4\pi}$	$g_{\eta\eta}$	$g_{\eta'\eta'}$
0.65100	0.22889	-0.55377	0.00000	-0.39899	-0.34639
1.20360	0.94128	0.55095	0.00000	0.39065	0.31503
1.55817	0.36856	0.23888	0.55639	0.18340	0.18681
1.21000	0.33650	0.40907	0.85679	0.19906	-0.00984
1.82206	0.18171	-0.17558	-0.79658	-0.00355	0.22358
s_0^{scatt}	f_{11}^{scatt}	f_{12}^{scatt}	f_{13}^{scatt}	f_{14}^{scatt}	f_{15}^{scatt}
-3.92637	0.23399	0.15044	-0.20545	0.32825	0.35412
s_0^{prod}	f_{11}^{prod}	f_{12}^{prod}	f_{13}^{prod}	f_{14}^{prod}	f_{15}^{prod}
-3.92637	-11.44+0.057i	-6.62+13.97i	-3.58-5.89i	0	0
	$s_{A0} = -0.15$			$s_A = 1$	

Table 5.2: Constants used in the K-matrix calculation of the $\pi\pi$ S-wave, from Ref [24]. Pole masses and coupling constants are in GeV.

but note that our sign convention differs with respect to s_0, which we take negative)

$$K_{ij}(s) = \left(f_{ij}^{scatt} \frac{1 - s_0^{scatt}}{s - s_0^{scatt}} + \sum_\alpha \frac{g_i^\alpha g_j^\alpha}{m_\alpha^2 - s} \right) \left(\frac{1 - s_{A0}}{s - s_{A0}} \frac{2s - s_A m_\pi^2}{2} \right). \tag{5.60}$$

The free parameters in our fit are the complex production coupling constants β_α. This leaves the K-matrix pole masses m_α, coupling constants g_i^α, Adler zeroes s_A and s_{A0}, and production background parameters f_{1j}^{prod} and s_0^{prod}, all of which we take from [24] and leave constant. Their values are shown in Table 5.2. Notice that the f_{ij} are zero for $i \neq \pi\pi$, since the final state is $\pi\pi$.

5.4 LASS parametrisation

For the case of the $K\pi$ S-wave, there is an alternative to the isobar model, known as the LASS parametrisation. Its origin is a study of K^-p scattering to $K^-\pi^+n$ carried out at SLAC by the LASS collaboration (Ref. [25]). This study found a broad, spinless resonance in the $K\pi$ spectrum with a Breit-Wigner lineshape, centered around 1430 MeV/c^2, atop a non-resonant background. LASS therefore adopted an effective-range parametrisation of the

background, giving an S-wave transition matrix

$$T = \sin\delta_B e^{i\delta_B} + \sin\delta_R e^{i\delta_R} e^{2i\delta_B}, \tag{5.61}$$

where

$$\tan\delta_R = \frac{m_r\Gamma(s)}{m_r^2 - m_{K\pi}^2}, \tag{5.62}$$

$$\cot\delta_B = \frac{1}{ap} + \frac{rp}{2}, \tag{5.63}$$

a is the scattering length, r is the effective range, and p is the 3-momentum of the spectator particle in the two-body rest frame (in our case, the excluded pion). We can consider this as a special case of the two-body K-matrix formalism with $K = \tan(\delta_B+\delta_R)$; the parametrisation is thus describing a rapid phase shift from a resonant part (subscripts R) and a slower shift from the non-resonant background part (subscripts B).

So far the parametrisation applies only to the elastic case; we can generalise to production experiments by adding a relative phase ϕ_B and magnitude R to the terms:

$$T = \sin(\delta_B + \phi_B)e^{i(\delta_B+\phi_B)} + R\sin\delta_R e^{i(\delta_R+\phi_R)} e^{2i(\delta_B+\phi_B)}. \tag{5.64}$$

This reproduces the $K_0^*(1430)$ lineshape in the presence of final-state interactions, which were absent in the scattering case discussed above (Ref. [26]). For the Dalitz-plot mode, we use the Lorentz-invariant amplitude

$$\hat{T} = \frac{T}{\rho(s)} = \frac{T\sqrt{s}}{2q(s)} \tag{5.65}$$

$$= e^{i\phi_B}\frac{(\cos\phi_B + \cot\delta_B\sin\phi_B)\sqrt{s}}{q(s)\cot\delta_B - iq(s)} \tag{5.66}$$

$$+ Re^{i\phi_R}e^{i2(\delta_B+\phi_B)}\frac{m_r\Gamma_r(m_r/q(m_r^2))}{m_r^2 - s - im_r\Gamma(s)}, \tag{5.67}$$

Parameter	a	r	R	ϕ_R	ϕ_B
Value	0.224	-15.042	1.627	1.11	-0.098

Table 5.3: Values of the LASS parameters.

with

$$q(s)\cot\delta_B = \frac{1}{a} + \frac{rq(s)^2}{2} \tag{5.68}$$

and

$$e^{i2\delta_B} = \frac{q(s)\cot\delta_B + iq(s)}{q(s)\cot\delta_B - iq(s)}. \tag{5.69}$$

Note that this reduces to the elastic case if $B = R = 1$, $\phi_B = \phi_R = 0$.

The free parameters in the LASS variant of the fit are the phase and amplitude of the two $K\pi$ S-waves, relative to the ρ. The parameters of the LASS function are held fixed to the values shown in Table 5.3.

Chapter 6

Fit description

This chapter describes the procedure for fitting the data. This is the means by which we extract the mixing parameters; a Probability Density Function (PDF) describes the variation in D^0 decay time across the Dalitz plot as a function of x and y, and we then search $x - y$ space (while allowing other parameters to float) to find the pair which best describes the variation actually present in our data.

6.1 Fit steps

In addition to the change in D^0 decay times, the PDF also describes the distribution of signal and background in the mass of the D^0 (m_{D^0}), the D^*-D^0 mass difference (Δm), and the Dalitz plot. The first two are used to find the amount of signal and background in our sample, while the Dalitz-plot distribution is a necessary prerequisite for doing a fit to the distribution of decay times across the Dalitz plot. Because this makes the PDF quite complicated, we perform the fit in two steps:

- Fit to the m_{D^0}-Δm distribution. We use the m_{D^0} value from the geometric fit (described in Chapter 4), and the Δm value from the beam-constrained fit.

- Keeping the signal and background fractions from the previous step fixed as weighting factors, do a full time-dependent fit to the Dalitz plot, using only the data in the signal

region $1.8534 < m_{K\pi\pi} < 1.8656$ GeV/c^2, $0.1447 < \Delta m < 0.1461$ GeV/c^2; this is $\pm 2\sigma$ in both quantities. The fit variables are the decay time t and its uncertainty σ_t (both taken from the beam-constrained fit) and the Dalitz-plot coordinates $m^2_{K\pi^+}$ and $m^2_{K\pi^-}$.

The following sections describe the PDFs used in each step in detail.

6.1.1 Notes on normalisation

Each PDF is normalised by integrating it, analytically where possible, over the phase space of the observables it depends on - usually one of the pairs $m_{D^0}, \Delta m$ or t, σ_t. In the interest of brevity the normalisation terms are given separately; thus, if it is stated that a PDF is $P(x)$, it should be understood that the actual value is $P(x)/N(x)$, where

$$N(x) = \int_{x_{min}}^{x_{max}} P(x)\mathrm{d}x. \tag{6.1}$$

Where the $N(x)$ have analytic formulae, these will be given; however, since many of the PDFs are Gaussian functions, rather than repeating this well-known integral several times we give it once here:

$$\begin{aligned} N_G(x;\sigma,\overline{x}) &= \int_{x_{min}}^{x_{max}} e^{-\frac{(x-\overline{x})^2}{2\sigma^2}}\mathrm{d}x & (6.2)\\ &= \sigma\sqrt{\frac{\pi}{2}}\left(\mathrm{erf}(\frac{x_{max}-\overline{x}}{\sqrt{2}\sigma} - \mathrm{erf}(\frac{x_{min}-\overline{x}}{\sqrt{2}\sigma})\right) & (6.3)\end{aligned}$$

where erf is the error function.

6.2 Step 1: D^0 mass and Δm fit

The PDF for the first stage has terms accounting for signal events and for three kinds of background:

$$P_1(m_{D^0},\Delta m) = n_1 P_s(m_{D^0},\Delta m) + n_2 P_2(m_{D^0},\Delta m) \tag{6.4}$$

$$+n_3 P_3(m_{D^0}, \Delta m) + n_4 P_4(m_{D^0}, \Delta m). \tag{6.5}$$

Here n_i is the number of events in category i. The categories are numbered thus:

- Category 1 consists of correctly-reconstructed signal events (including those where a pion decayed in flight to a muon).
- Category 2 consists of events where a D^0 has been correctly reconstructed, but matched with a slow pion from elsewhere in the event to create a fake D^*.
- Category 3 events have a slow pion that did come from a D^* decay, but the D^0 reconstruction is wrong.
- Category 4 events are 'combinatoric'; neither the D^0 nor the slow-pion reconstruction are correct.

Note that events in which a $\pi \to \mu\nu$ decay occurred are considered signal; their main effect is to broaden the D^0 mass distribution. The total likelihood contains a term for the Poisson probability of seeing N events, the size of the actual data sample, from an expectation of $n_1 + n_2 + n_3 + n_4$, in effect constraining the sum of the yields to the observed sample size.

The signal PDF $P_s(m_{D^0}, \Delta m)$ consists of an uncorrelated and a correlated part:

$$P_s(m_{D^0}, \Delta m; f_u) \;=\; f_u G(m_{D^0}) J(\Delta m) + (1 - f_u) G_c(m_{D^0}, \Delta m) \tag{6.6}$$

where $G(m_{D^0})$ is a sum of two Gaussians, $J(\Delta m)$ is the sum of a Gaussian and a Johnson function, and $G_c(m_{D^0}, \Delta m)$ is the sum of two correlated Gaussians. For these functions it is convenient to introduce the notation

$$\hat{x}_i = \frac{x - \overline{x}_i}{\sigma_{xi}}, \tag{6.7}$$

allowing us to briefly express the distance of variable x from its ith mean in units of its ith uncertainty. Notice that each subscript i introduces two new fit parameters; for example, the

notation $\hat{m}_1$ hides a mean $\overline{m}_1$ and an uncertainty σ_{m1}. To avoid an abundance of subscripts, in the following we use m for m_{D^0} and d for Δm. With these shorthands, we have

$$\begin{aligned}
G(m; f_{g1}, \hat{m}_1, \hat{m}_2) &= f_{g1} e^{-0.5\hat{m}_1^2} + (1 - f_{g1}) e^{-0.5\hat{m}_2^2} && (6.8)\\
J(d; f_{J1}, \delta_{J1}, \gamma_{J1}, \sigma_{J1}, \hat{d}_{J1}, \hat{d}_{J2}) &= f_{J1} \frac{\delta_{J1} e^{-0.5(\gamma_{J1} + \delta_{J1} \ln(\hat{d}_{J1} + \sqrt{1+\hat{d}_{J1}^2}))^2}}{\sqrt{\pi/2}\sigma_{J1}\sqrt{1+\hat{d}_{J1}^2}} && (6.9)\\
&\quad + (1 - f_{J1}) e^{-0.5\hat{d}_{J2}^2} && (6.10)\\
G_c(m, d; f_{G1}, k_{G1}, k_{G2}, \hat{m}_{G1}, \hat{m}_{G2}, \hat{d}_{G1}, \hat{d}_{G2}) &= f_{G1} e^{-0.5\hat{m}_{G1}^2} e^{-\frac{\hat{d}_{G1}^2}{2\left(1 + k_{G1}\hat{m}_{G1}^2\right)}} && (6.11)\\
&\quad + (1 - f_{G1}) e^{-0.5\hat{m}_{G2}^2} e^{-\frac{\hat{d}_{G2}^2}{2\left(1 + k_{G2}\hat{m}_{G2}^2\right)}}. && (6.12)
\end{aligned}$$

Notice that in the case where the correlation coefficients k are zero, the correlated Gaussians reduce to products of independent, separate Gaussian functions. The Johnson function and correlated Gaussian are integrated numerically.

The category-2 background shares its m_{D^0} functional form and parameters with the signal PDF:

$$P_2(m_{D^0}, \Delta m) = f_u G(m_{D^0}) A(\Delta m) + (1 - f_u) G_c(m_{D^0}, \Delta m) \quad (6.13)$$

where $G(m_{D^0})$ and $G_c(m_{D^0}, \Delta m)$ are the same as for signal, describing correctly reconstructed D^0 particles, and $A(\Delta m)$ is a threshold function:

$$A(\Delta m; a, b) = \begin{cases} 0, & \Delta m < t \\ \Delta m \sqrt{(\Delta m/a)^2 - 1}\, e^{b((\Delta m/a)^2 - 1)}, & \Delta m \geq a. \end{cases} \quad (6.14)$$

The threshold parameter a is fixed at 139.5 MeV/c^2, the kinematic boundary for $D^{*+} \to D^0\pi^+$ decays. The normalisation for this function is

$$\begin{aligned}
\int_{x_{min}}^{x_{max}} A(x; a, b)\mathrm{d}x &= \frac{a^2}{2}\Bigg(e^{b(x_{max}^2/a - 1)} \frac{1}{b} \sqrt{x_{max}^2/a - 1} + && (6.15)\\
&\quad \frac{\sqrt{\pi}}{2(-b)^{3/2}} \mathrm{erf}(\sqrt{-b(x_{max}^2/a - 1)}) -
\end{aligned}$$

$$e^{b(x^2_{min}/a-1)}\frac{1}{b}\sqrt{x^2_{min}/a-1}+$$
$$\frac{\sqrt{\pi}}{2(-b)^{3/2}}\mathrm{erf}(\sqrt{-b(x^2_{min}/a-1)})\Bigg)$$

where it is worth noting that the slope parameter b is always negative.

Intuitively the category-3 background might be expected to similarly share the signal distribution for Δm, and have a flat or exponential PDF for m_{D^0}, but in fact its distribution proved hard to capture in an analytic function. Instead we simply use a histogram of its Monte Carlo distribution,

$$P_3(m_{D^0}, \Delta m) \;=\; H(m_{D^0}, \Delta m) \tag{6.16}$$

where H is in effect a lookup table for the density. This distribution is shown in Figure 6.1. The normalisation is simply the sum of the histogram entries.

The category-4 background, being combinatorial in both dimensions, is more or less flat; it shares its Δm description with the category-2 PDF and has a simple polynomial for m_{D^0}:

$$P_4(m_{D^0}, \Delta m; c) \;=\; (1 + c m_{D^0}) A(\Delta m). \tag{6.17}$$

Table 6.1 shows the parameter values returned by this fit; Figures 6.2 and 6.3 show the fits to the data. The peak (evaluated numerically) of the $m_{K\pi\pi}$ signal PDF for data occurs at 1.86408 GeV/c^2, and the average at 1.86411 GeV/c^2. Since these numbers reflect the specifics of the *BABAR* detector, e.g. its momentum scale, we use this average rather than the nominal PDG value 1.86484 GeV [11] to define the signal box when reducing the data set for the second step of the fit. For Monte Carlo samples, the real value of the D^0 mass is known to be 1.8645 GeV, and this is the value we use.

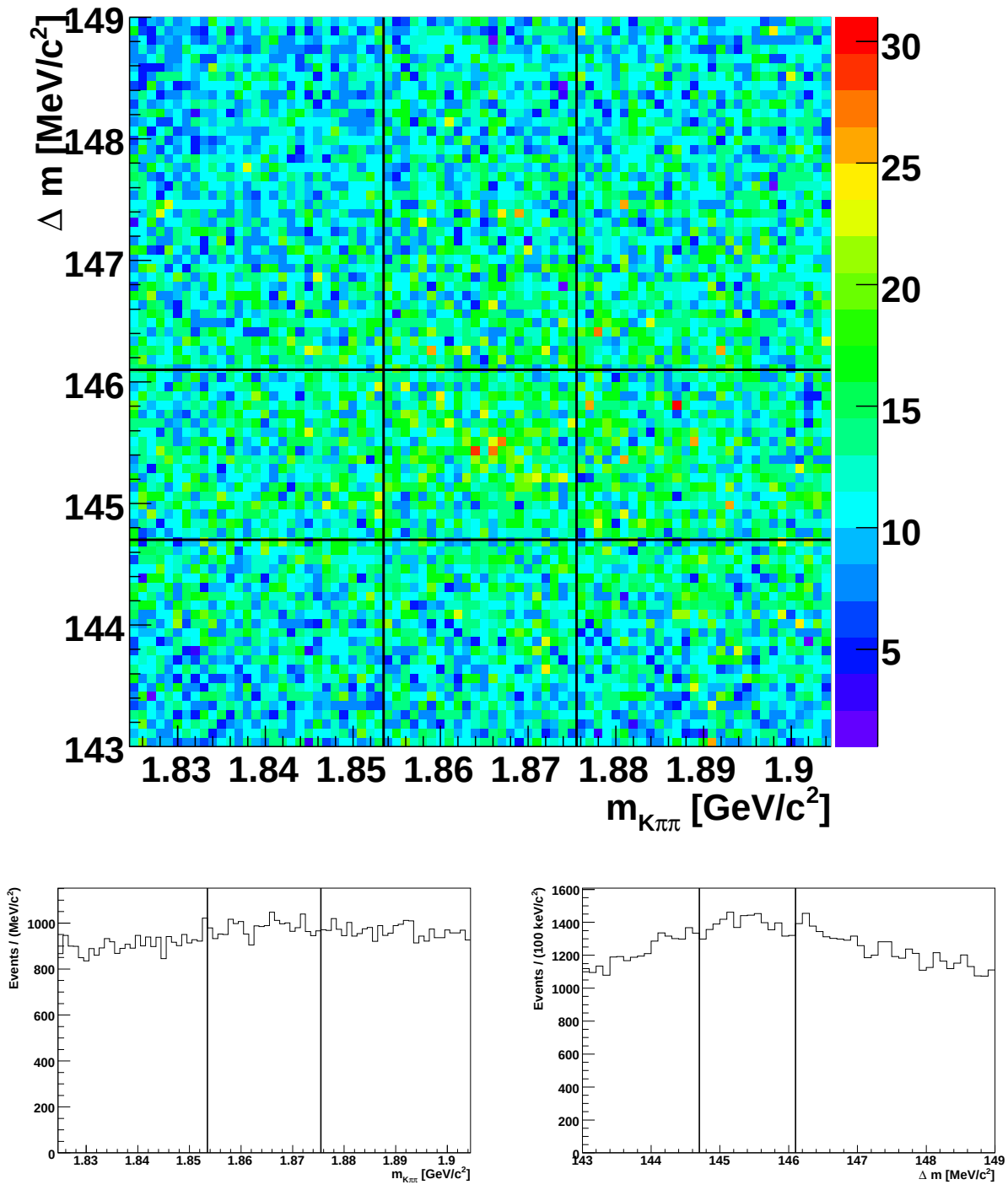

Figure 6.1: a) Distribution of category-3 background in the $m_{K\pi\pi} - \Delta m$ plane. The black lines indicate the signal box. Note the low, broad ridge running along the signal Δm region. b) Projection to $m_{K\pi\pi}$. c) Projection to Δm.

Parameter name	Comment	Value
	Signal	
n_1	Number of signal events	613134 ± 12104
f_u	Fraction of uncorrelated part of PDF	0.8589 ± 0.0048
f_{g1}		0.4796 ± 0.0140
$\overline{m}_1$	First mean for m_{D^0}	(1.86350 ± 0.00004) GeV/c^2
σ_{m1}	First σ for m_{D^0}	(0.00698 ± 0.00006) GeV/c^2
$\overline{m}_2$		(1.86432 ± 0.00003) GeV/c^2
σ_{m2}		(0.00474 ± 0.00003) GeV/c^2
f_{J1}	Fraction of Δm Johnson function	0.5345 ± 0.0058
$\overline{d}_{J1}$	Mean of Δm Johnson function	(145.41 ± 0.0020) MeV/c^2
σ_{J1}		(0.1494 ± 0.0020) MeV/c^2
γ_{J1}		-0.0423 ± 0.0044
δ_{J1}		0.6341 ± 0.0074
$\overline{d}_{J2}$		(145.41 ± 0.0013) MeV/c^2
σ_{dJ2}		(0.1755 ± 0.0009) MeV/c^2
f_{G1}	Fraction of first correlated Gaussian	0.7455 ± 0.0209
$\overline{d}_{G1}$	First correlated Δm mean	(145.403 ± 0.004) MeV/c^2
σ_{dG1}	First correlated Δm sigma	(0.3035 ± 0.0059) MeV/c^2
$\overline{m}_{G1}$		(1.8642 ± 0.0004) GeV/c^2
σ_{mG1}		(0.0150 ± 0.0003) GeV/c^2
k_{G1}	First correlation coefficient	0.0771 ± 0.01302
$\overline{d}_{G2}$		(145.416 ± 0.001) MeV/c^2
σ_{dG2}		(0.4836 ± 0.0378) MeV/c^2
$\overline{m}_{G2}$		(1.8456 ± 0.0015) GeV/c^2
σ_{mG2}		(0.0152 ± 0.0010) GeV/c^2
k_{G2}		0.1861 ± 0.0397
	Background	
n_2	Number of category-2 events	26357 ± 939
n_3	Number of category-3 events	3362 ± 5546
n_4	Number of category-4 events	167879 ± 3263
b	Slope of threshold function	-4.0498 ± 0.1089
c	Slope of polynomial	-0.2738 ± 0.0599

Table 6.1: Fit results from the step-1 fit to data.

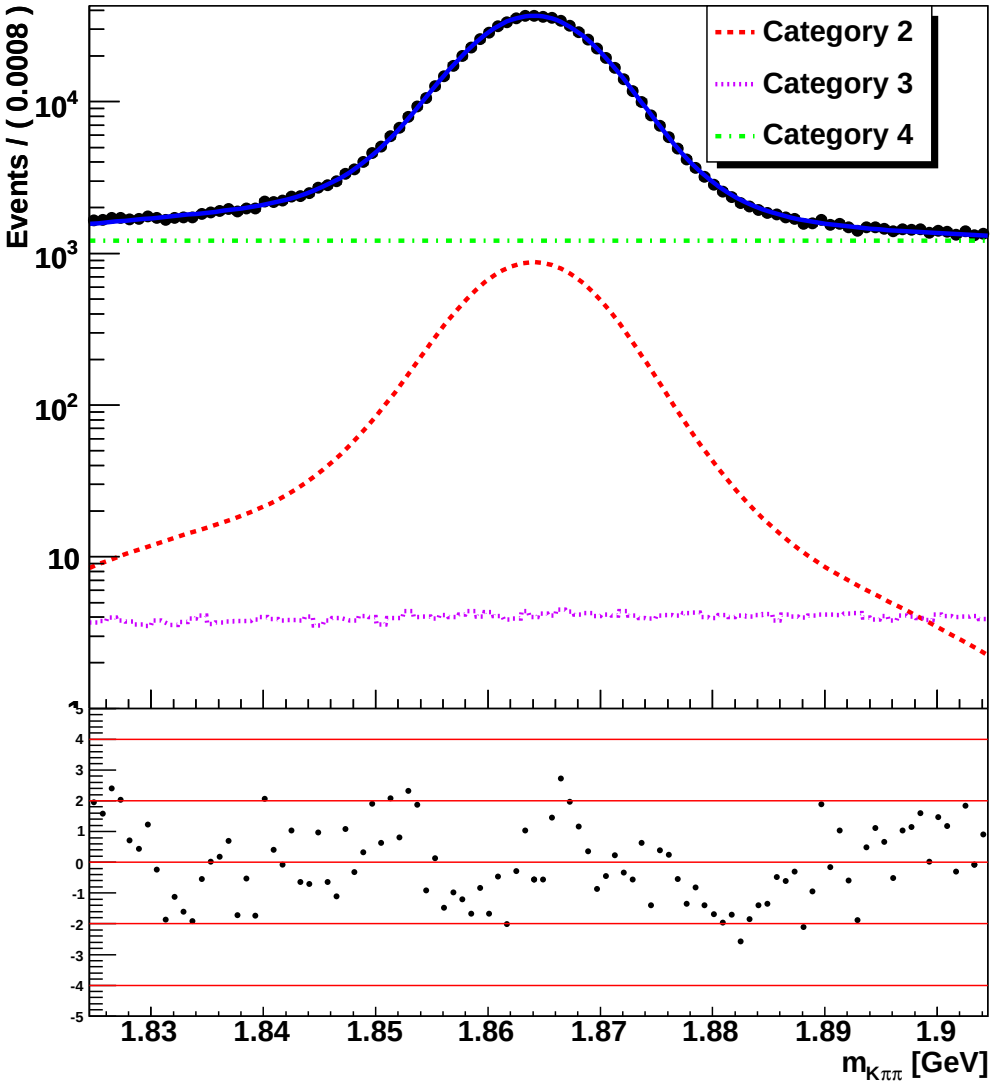

Figure 6.2: Step-1 fit to data projected to $m_{K\pi\pi}$. The background categories are shown separately, not cumulatively - that is, the green dash-dotted line shows only category 4, not category 2+3+4. The lower part of the plot shows the normalised residuals, that is, the data minus the curve, divided by the error on the data.

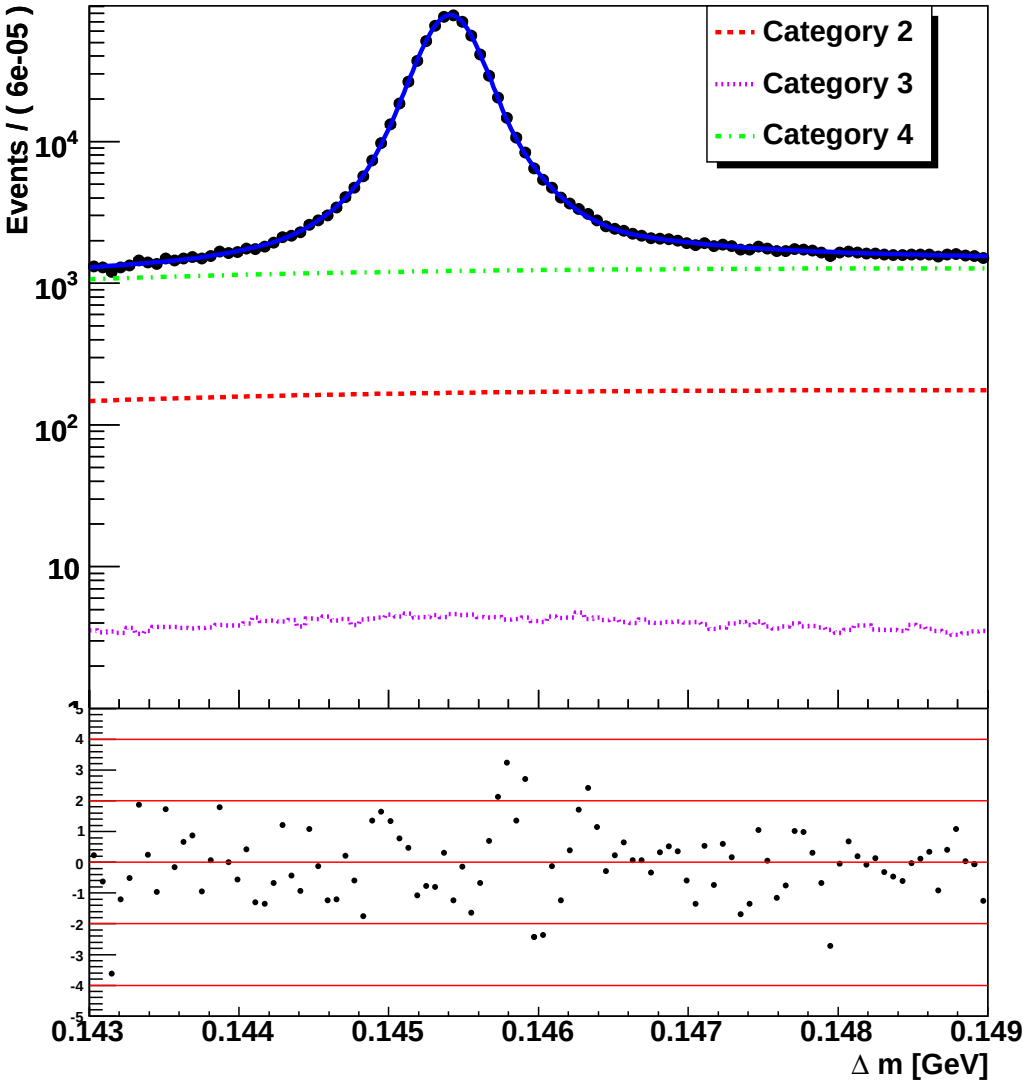

Figure 6.3: Step-1 fit to data projected to Δm. The background categories are shown separately, not cumulatively - that is, the green dash-dotted line shows only category 4, not category 2+3+4. The lower part of the plot shows the normalised residuals, that is, the data minus the curve, divided by the error on the data.

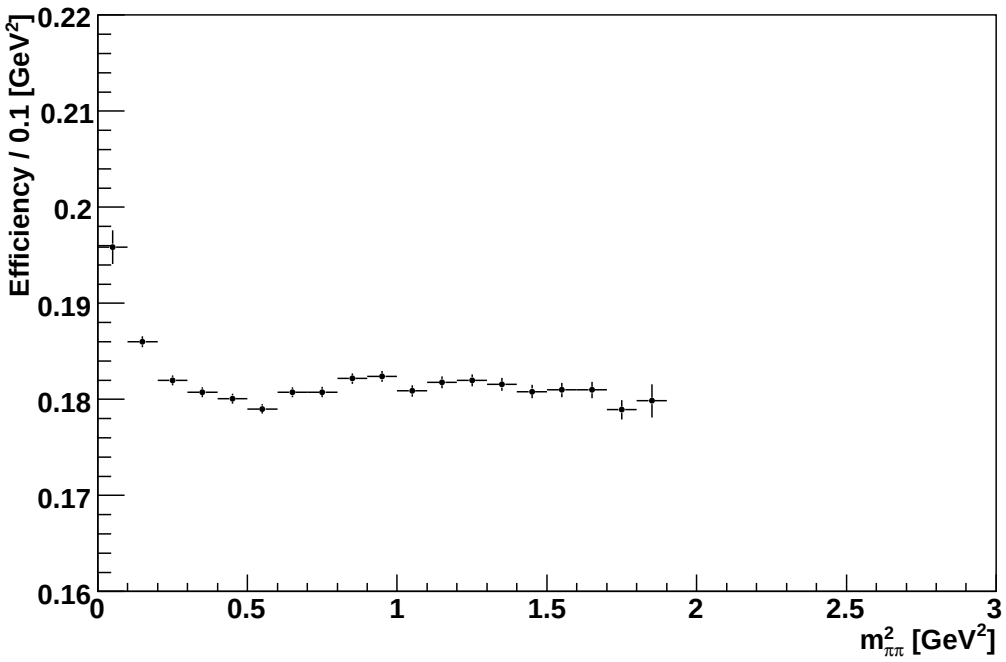

Figure 6.4: Reconstruction efficiency as a function of $m^2_{\pi\pi}$.

6.3 Efficiency

The efficiency of the reconstruction algorithm described in Chapter 4 depends slightly on the momentum of the final-state pions - in other words, on position in the Dalitz plot. In the signal PDF, this is modelled by simply multiplying the squared amplitude by the local efficiency. The local efficiency is found by generating flat Monte Carlo, signal events with no dependence of the amplitude on the Dalitz plot, reconstructing it, and dividing the resulting reconstructed distribution by the original generated distribution. Figures 6.4 through 6.7 show the results. This histogram is used as a lookup table for determining the local efficiency for all fits. To dampen out fluctuations, bins with fewer than 50 reconstructed entries use the average efficiency of their neighbouring bins. Only neighbour bins which themselves have more than 50 reconstructed entries are used in this average; if there are none, the overall average across the entire Dalitz plot is used instead.

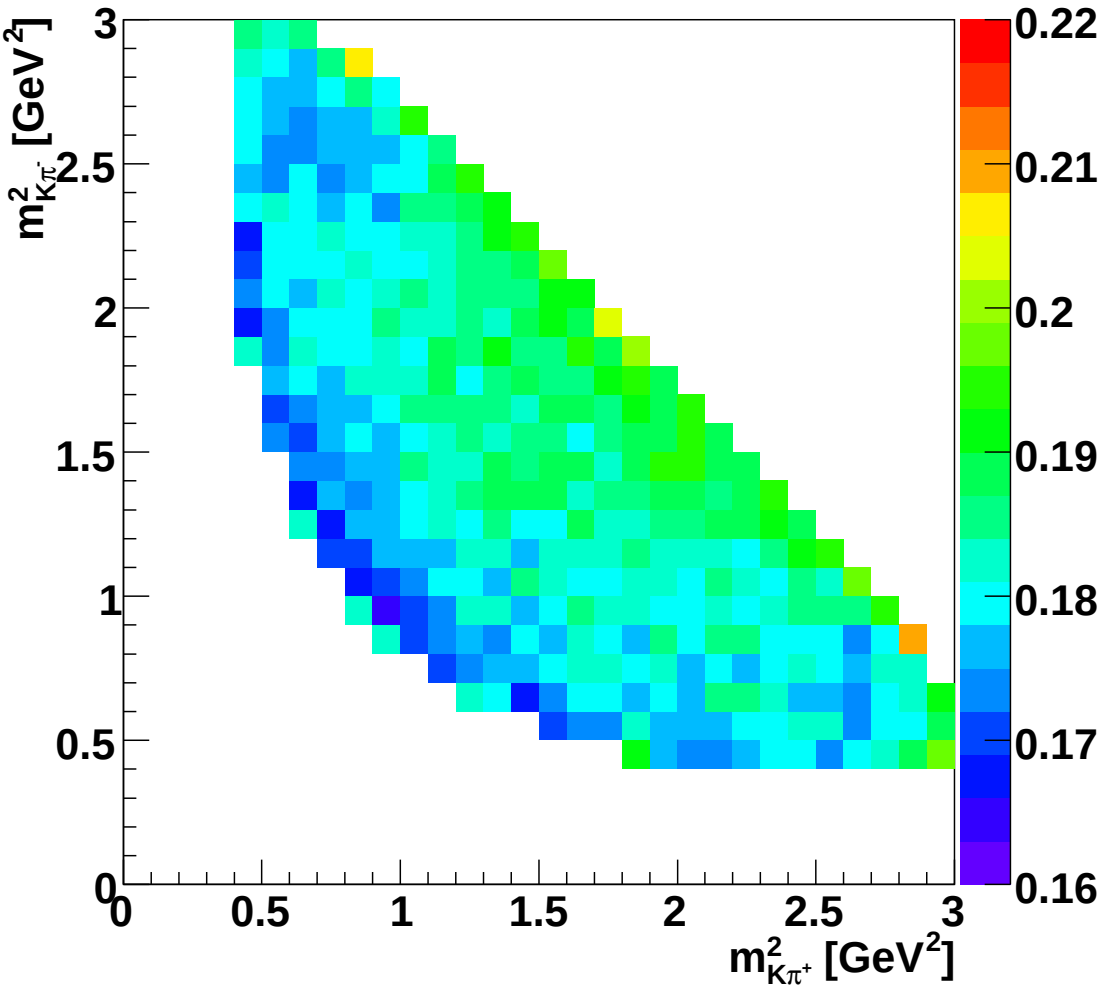

Figure 6.5: Reconstruction efficiency as a function of position in the Dalitz plot.

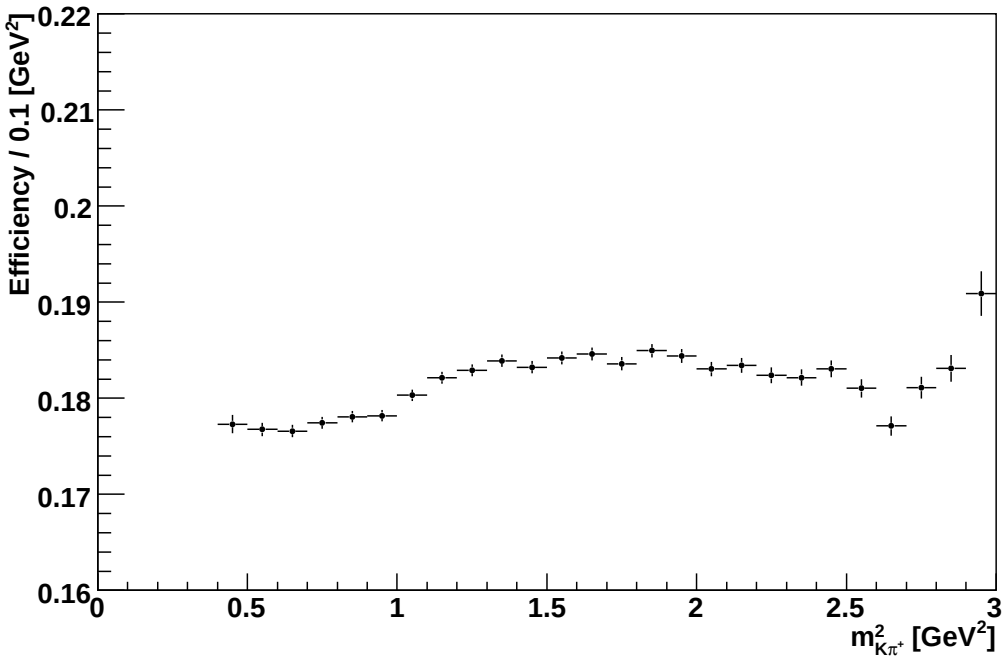

Figure 6.6: Reconstruction efficiency as a function of $m^2_{K\pi^+}$.

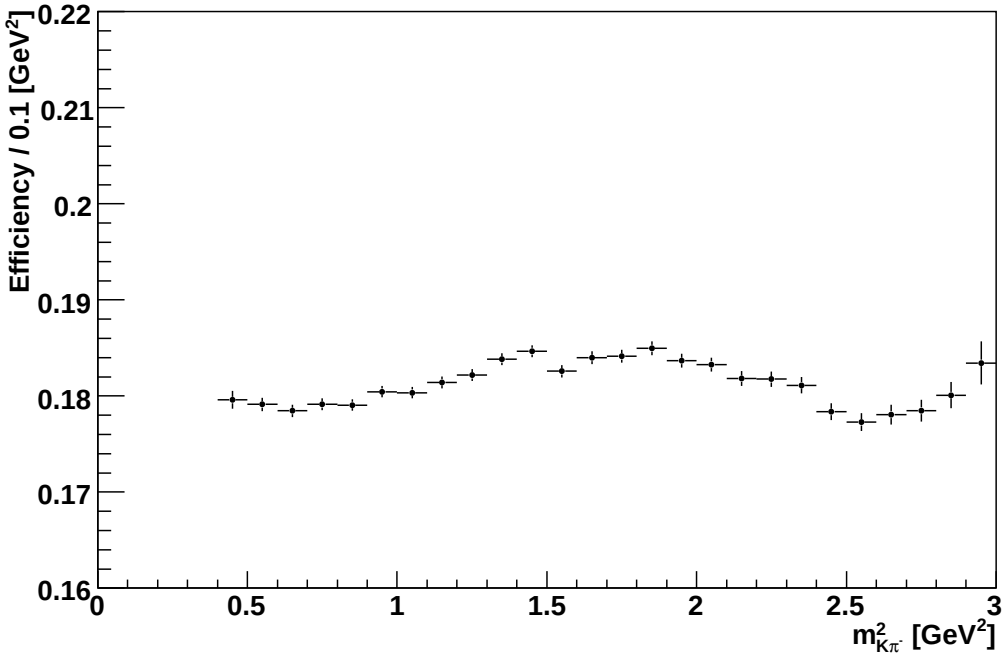

Figure 6.7: Reconstruction efficiency as a function of $m^2_{K\pi^-}$.

6.4 Step 2: Full mixing fit

Next we consider the fit to D^0 decay time and the Dalitz-plot variables $m^2_{K\pi^+}$ and $m^2_{K\pi^-}$, for events in the signal box shown in Figure 6.1. The amounts of each event category are scaled from the numbers found in the previous step and, along with the parameters of the m_{D^0}, Δm distributions, fixed. The PDF describing the Dalitz-plot distribution of signal events is a combination the pure-BW isobar model described in Chapter 5; models with K-matrix and LASS parametrisations are used for evaluating systematic errors. This model applies to D^0 decays; in events where the slow pion is negatively charged, indicating a D^{*-} and hence a $\overline{D^0}$, we interchange the Dalitz-plot coordinates before adding the event to the data set. Note that the data set is reduced from that used in the previous step, since we use only events within the *signal box*, that is, with Δm between 144.7 and 146.1 MeV/c^2 and m_{D^0} within 11 MeV/c^2 of the average m_{D^0} value found in step 1. The box is thus $\pm 2\sigma$ in each of these two quantities.

The Dalitz-plot and time distributions for the background components are as follows. The category-2 background shares the isobar model used for signal, except that it has a wrong-sign component:

$$P_2(m_{K\pi^+}, m_{K\pi^-}; f_{RS}) \;=\; f_{RS} I(m_{K\pi^+}, m_{K\pi^-}) + (1 - f_{RS}) I(m_{K\pi^-}, m_{K\pi^+}). \quad (6.18)$$

Here $I(m_{K\pi^+}, m_{K\pi^-})$ is the signal isobar model. Note the reversal of the arguments in the second term; this represents D^0 particles correctly reconstructed, but matched with a pion of the wrong charge and therefore wrongly identified as $\overline{D^0}$, or vice-versa. These events will either have had their Dalitz-plot variables flipped when they should not have been, or left alone when they should have been flipped; the reversed component accounts for this. The fraction f_{RS} is taken from Monte Carlo and held fixed at 54%; there is a corresponding systematic error from varying it. The time distribution of the category-2 events is the same as that used for the signal, including dependence on x and y, since these events are sufficiently correctly reconstructed to be sensitive to mixing.

Parameter name	Comment	Value
$\overline{t_{b1}}$	Mean of first Gaussian	-0.051 ps
σ_{b1}	Sigma of first Gaussian	0.977 ps
$\overline{t_{b2}}$	Mean of second Gaussian	0.172 ps
σ_{b2}	Sigma of second Gaussian	0.396 ps
f_{b1}	Fraction of first Gaussian	40.2%
f_{b2}	Fraction of second Gaussian	55.8%
s_{34}	Slope of linear term	0

Table 6.2: Parameters of the background time distribution.

The category-3 and category-4 backgrounds in the Dalitz plot are both modeled simply by a histogram, shown in Figure 6.8. As with the category-3 model of the m_{D^0}, Δm distribution, the histogram is created from Monte Carlo, and acts as a lookup table showing the density of events at each point in the Dalitz-plot space. The time distribution for these categories is a sum of two Gaussians and a straight line:

$$T_{34}(t; f_{b1}, f_{b2}) = f_{b1}G_{b1}(t) + f_{b2}G_{b2}(t) + (1 - f_{b1} - f_{b2}L(t) \tag{6.19}$$

with (using the hat notation introduced in Section 6.2)

$$G_{b1}(t; \hat{t}_{b1}) = e^{-0.5\hat{t}_{b1}^2} \tag{6.20}$$

$$G_{b2}(t; \hat{t}_{b2}) = e^{-0.5\hat{t}_{b2}^2} \tag{6.21}$$

$$L(t; s_{34}) = (1 + s_{34}t). \tag{6.22}$$

The straight line normalisation is straightforward:

$$N_L^{-1}(t; s_{34}) = t_{max} - t_{min} + 0.5s_{34}(t_{max}^2 - t_{min}^2). \tag{6.23}$$

The parameters of this function are found by fitting to Monte Carlo, and held fixed in the fit to data; they are shown in Table 6.2. A systematic uncertainty is assigned to this procedure by varying the parameters within their uncertainty.

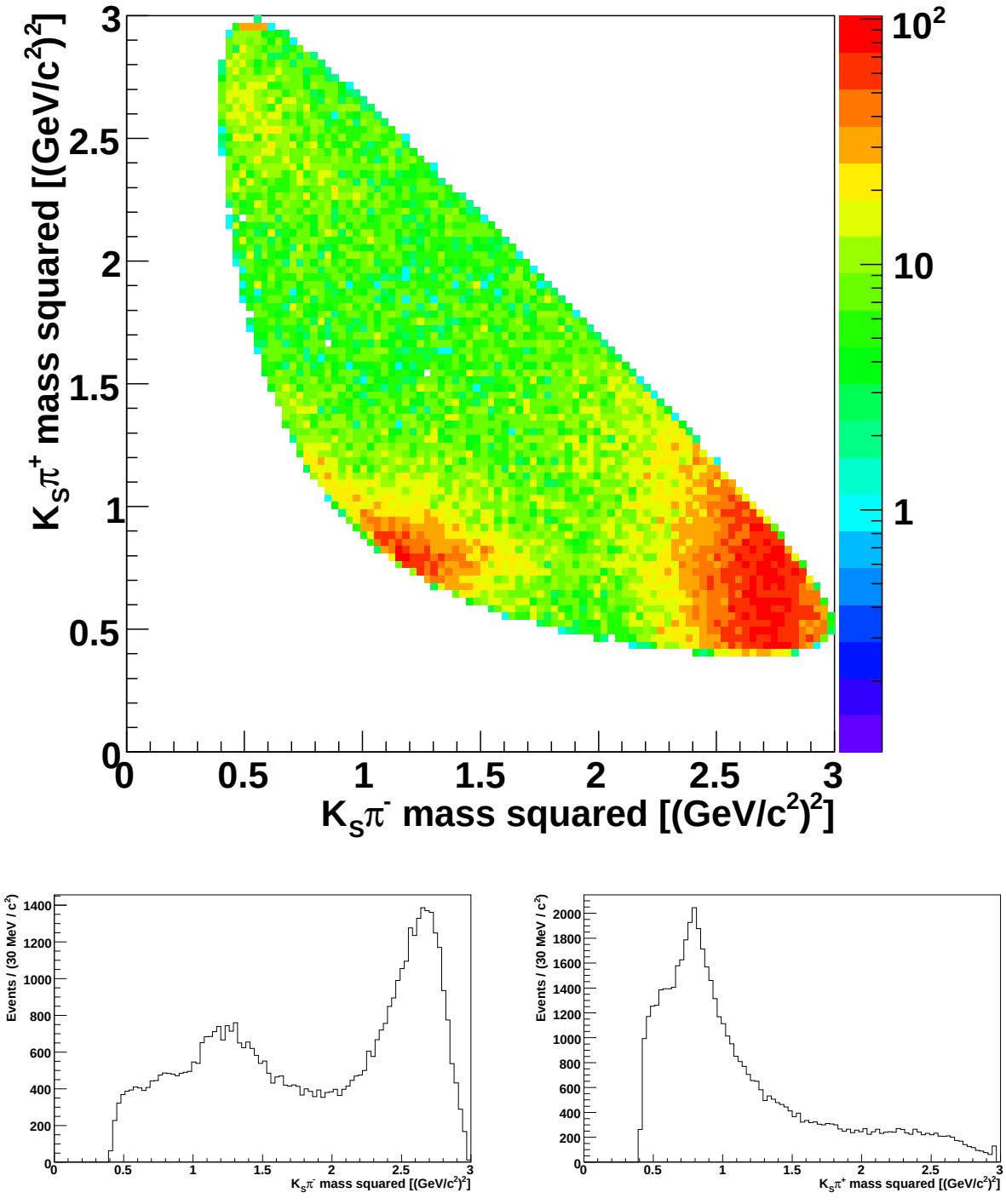

Figure 6.8: a) Dalitz-plot distribution of category-3 and category-4 background within the $m_{K\pi\pi} - \Delta m$ signal box. b) Projection to $m^2_{K\pi^-}$. c) Projection to $m^2_{K\pi^+}$.

The full signal PDF including the time and σ_t distribution is

$$P_s(m_{K\pi^+}, m_{K\pi^-}, t, \sigma_t) = (A(m_{K\pi^+}, m_{K\pi^-}, t)E(m_{K\pi^+}, m_{K\pi^-})) \otimes S(t, \sigma_t))H(\sigma_t) \quad (6.24)$$

where $E(m_{K\pi^+}, m_{K\pi^-})$ is the efficiency, and $A(m_{K\pi^+}, m_{K\pi^-}, t)$ is given by Eqn. 2.28, which we repeat here for convenience:

$$\begin{aligned} A(m_{K\pi^+}, m_{K\pi^-}, t) &= |A_1|^2 e^{-(1+y)t/\tau} && (6.25)\\ &\quad +|A_2|^2 e^{-(1-y)t/\tau} && (6.26)\\ &\quad +2\Re\left(A_1 A_2^*\right) e^{-t/\tau} \cos(xt/\tau) && (6.27)\\ &\quad +2\Im\left(A_1 A_2^*\right) e^{-t/\tau} \sin(xt/\tau). && (6.28) \end{aligned}$$

The uncertainty in our measurement of t is σ_t, and the resolution function $S(t, \sigma_t)$ is a sum of three Gaussians, denoted 'C', 'T' and 'O' for 'core', 'tail' and 'outlier' respectively:

$$\begin{aligned} S(t, \sigma_t; f_C, f_T, b_C, b_T, b_O, s_C, s_T, s_O) &= f_C e^{-\frac{(t-b_C)^2}{2(s_C\sigma_t)^2}} && (6.29)\\ &\quad + f_T e^{-\frac{(t-b_T)^2}{2(s_T\sigma_t)^2}} && (6.30)\\ &\quad + (1 - f_C - f_T) e^{-\frac{(t-b_O)^2}{2s_O^2}}. && (6.31) \end{aligned}$$

Notice that the outlier Gaussian is different from the other two, in that it uses a global error s_O rather than a scaling factor on the per-event error, $s_{C,T}\sigma_t$. The core Gaussian offset b_C is permitted to vary; the other two have their offsets b_T and b_O fixed at zero. The width of the outlier is also fixed, but as it turns out, the fit in any case assigns it a negligible fraction. The distribution $H(\sigma_t)$ of the per-event errors is modelled by a separate histogram for each category; the overall distribution is shown in Figure 6.9. (The distribution can also vary across the Dalitz plot; this is considered as a systematic in the next chapter, by having separate distributions for 2, 4 or 8 $m_{\pi\pi}$ mass strips.) Having a separate σ_t distribution for each category slightly increases our power to discriminate between them, but more importantly, it avoids the infamous Punzi effect described in Ref [27]. With these

notes we are ready to look at the full convolved equation, which is moderately complicated. For clarity, we will suppress the sum over three Gaussians and show the convolution with only one, which we denote $G(t;\sigma,b)$. Here the σ - no subscript - is the *effective* width of the Gaussian: Either the per-event σ_t multiplied by the respective scale factor s_C or s_T, or the global outlier width s_O; and b is the offset denoted $b_{C,T,O}$ above. We then find

$$\begin{aligned}
A(m_+^2,m_-^2,t)\otimes S(t,\sigma_t) &= \int_{-\infty}^{\infty} A(m_+^2,m_-^2,t)G(t'-t;\sigma,b)\mathrm{d}t' \\
&= \int_{-\infty}^{\infty} |A_1|^2 e^{-(1+y)t/\tau} G(t'-t;\sigma,b)\mathrm{d}t' + \\
&\quad \int_{-\infty}^{\infty} |A_2|^2 e^{-(1-y)t/\tau} G(t'-t;\sigma,b)\mathrm{d}t' + \\
&\quad \int_{-\infty}^{\infty} 2\Re\left(A_1A_2^*\right) e^{-t/\tau}\cos(xt/\tau) G(t'-t;\sigma,b)\mathrm{d}t' + \\
&\quad \int_{-\infty}^{\infty} 2\Im\left(A_1A_2^*\right) e^{-t/\tau}\sin(xt/\tau) G(t'-t;\sigma,b)\mathrm{d}t' \\
&= |A_1|^2 e^{-\frac{t-b}{\tau/(1+y)}} e^{\frac{\sigma_t^2(1+y)^2}{2\tau^2}} \mathrm{erfc}\left(K(t;\sigma,\tau/(1+y),b)\right) + \\
&\quad |A_2|^2 e^{-\frac{t-b}{\tau/(1-y)}} e^{\frac{\sigma_t^2(1-y)^2}{2\tau^2}} \mathrm{erfc}\left(K(t;\sigma,\tau/(1-y),b)\right) + \\
&\quad 2\Re\left(A_1A_2^*\right) e^{-\frac{(t-b)^2}{2\sigma^2}} \Re\left[w\left(L(t;\sigma,\tau,-x,b)\right)\right] - \\
&\quad 2\Im\left(A_1A_2^*\right) e^{-\frac{(t-b)^2}{2\sigma^2}} \Im\left[w\left(L(t;\sigma,\tau,-x,b)\right)\right]
\end{aligned} \tag{6.32}$$

where $\mathrm{erfc}(x)$ is the complementary error function, $w(x) = e^{-x^2}\mathrm{erfc}(-ix)$ is the complex error function, and

$$K(t;\sigma,\tau,b) = \frac{\sigma}{\sqrt{2}\tau} - \frac{t-b}{\sqrt{2}\sigma} \tag{6.33}$$

$$L(t;\sigma,\tau,x,b) = \frac{x(t-b)}{\tau} + i\left(\frac{\sigma}{\sqrt{2}\tau} - \frac{t-b}{\sqrt{2}\sigma}\right). \tag{6.34}$$

Normalising these expressions is not entirely trivial, but fortunately they factorise into a Dalitz-plot part (A_1A_2 in various combinations, and the efficiency) and a time-dependent part. The former is evaluated numerically, and each term multiplied by the integral over t

of the corresponding resolution-function term, using the *average* σ_t as σ. Denoting the four resolution-function integrals by subscripts of the Dalitz-plot integrals they are multiplying, so that $N_{|A_1|^2}$ is the integral of the first term in Eqn. 6.32, we have

$$\begin{aligned} N_{|A_1|^2} &= -\frac{\tau}{1+y}\Bigg[\mathrm{erf}\left(-\frac{t_{max}-b}{\sqrt{2}\sigma}\right) - \mathrm{erf}\left(-\frac{t_{min}-b}{\sqrt{2}\sigma}\right) + \\ &\quad e^{\frac{\sigma^2(1+y)^2}{2\tau^2}} e^{-\frac{t_{max}-b}{\sqrt{2}\sigma}} \mathrm{erfc}\left(K(t_{max};\sigma,\tau/(1+y),b)\right) - \\ &\quad e^{\frac{\sigma^2(1+y)^2}{2\tau^2}} e^{-\frac{t_{min}-b}{\sqrt{2}\sigma}} \mathrm{erfc}\left(K(t_{min};\sigma,\tau/(1+y),b)\right)\Bigg] \end{aligned} \tag{6.35}$$

$$\begin{aligned} N_{|A_2|^2} &= -\frac{\tau}{1-y}\Bigg[\mathrm{erf}\left(-\frac{t_{max}-b}{\sqrt{2}\sigma}\right) - \mathrm{erf}\left(-\frac{t_{min}-b}{\sqrt{2}\sigma}\right) + \\ &\quad e^{\frac{\sigma^2(1-y)^2}{2\tau^2}} e^{-\frac{t_{max}-b}{\sqrt{2}\sigma}} \mathrm{erfc}\left(K(t_{max};\sigma,\tau/(1-y),b)\right) - \\ &\quad e^{\frac{\sigma^2(1-y)^2}{2\tau^2}} e^{-\frac{t_{min}-b}{\sqrt{2}\sigma}} \mathrm{erfc}\left(K(t_{min};\sigma,\tau/(1-y),b)\right)\Bigg] \end{aligned} \tag{6.36}$$

$$\begin{aligned} N_{\Re(A_1A_2^*)} &= -\frac{\tau}{1+x^2}\Bigg[\Re\left(w\left(L(t_{max};\sigma,\tau,-x,b)\right) - w\left(L(t_{min};\sigma,\tau,-x,b)\right)\right) + \\ &\quad x\Im\left(w\left(L(t_{max};\sigma,\tau,-x,b)\right) - w\left(L(t_{min};\sigma,\tau,-x,b)\right)\right) + \\ &\quad \mathrm{erf}\left(-\frac{t_{max}-b}{\sqrt{2}\sigma}\right) - \mathrm{erf}\left(-\frac{t_{min}-b}{\sqrt{2}\sigma}\right)\Bigg] \end{aligned} \tag{6.37}$$

$$\begin{aligned} N_{\Im(A_1A_2^*)} &= -\frac{\tau}{1+x^2}\Bigg[x\Re\left(w\left(L(t_{max};\sigma,\tau,-x,b)\right) - w\left(L(t_{min};\sigma,\tau,-x,b)\right)\right) - \\ &\quad \Im\left(w\left(L(t_{max};\sigma,\tau,-x,b)\right) - w\left(L(t_{min};\sigma,\tau,-x,b)\right)\right) + \\ &\quad x\left(\mathrm{erf}\left(-\frac{t_{max}-b}{\sqrt{2}\sigma}\right) - \mathrm{erf}\left(-\frac{t_{min}-b}{\sqrt{2}\sigma}\right)\right)\Bigg]. \end{aligned} \tag{6.38}$$

Tables 6.3 and 6.4 show the fit parameters. The central values for x and y were initially disguised by adding an unknown random number, which was revealed ('unblinding') only after all the choices for event selection had been made and all systematic studies finished. However, after unblinding, a bug was discovered in the fit PDF, making it necessary to re-run the fit. We assumed no *CP* violation in either mixing or decay, i.e. $p = q$ and $\arg(\lambda_f) = 0$. The statistical uncertainties of around 0.25% for the mixing parameters are comparable to those found by Belle (Ref. [5]).

The measured value 404.3 fs of τ is quite low compared to the world average of 410.1 fs. As a check on the robustness of the fit, therefore, we fix τ to its nominal value and repeat the

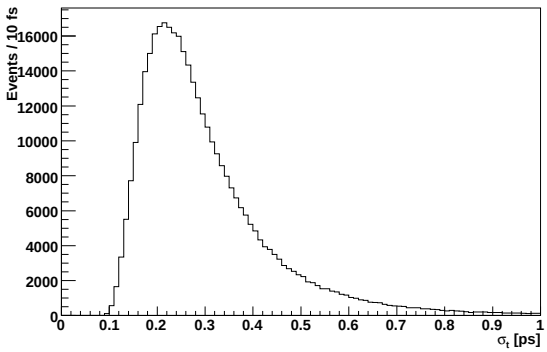

Figure 6.9: Distribution of σ_t, the reported error on the measured decay time from the kinematic fit.

fit. We find that x changes by less than 0.005%, while y changes by about 0.05%. Because correlations between fit parameters is already accounted for in the reported errors, we do not assign this change as a systematic error, but consider it a stability cross-check.

Parameter name	Comment	Value
Mixing results		
x		0.43% ± 0.25%
y		0.70% ± 0.22%
τ		404.3 ± 0.9 ps
Results for D^0 only		
x		0.49% ± 0.36%
y		0.82% ± 0.31%
τ		405.0 ± 1.3 ps
Results for $\overline{D}^0$ only		
x		0.46% ± 0.35%
y		0.55% ± 0.31%
τ		403.8 ± 1.3 ps
Resolution parameters		
f_C	Core fraction	86.4% ± 2.5%
f_T	Tail fraction	13.6% ± 2.5%
b_C	Core offset	-3.7 ± 0.8 ps
s_C	Core scale factor	0.96 ± 0.01
s_T	Tail scale factor	1.52 ± 0.05

Table 6.3: Fit results from the step-2 fit to data.

Resonance	$\Re c_j$	$\Im c_j$	Magnitude	Phase	Mass [GeV/c^2]	Width [GeV/c^2]	Spin	Type
$\pi^+\pi^-$								
$\rho(770)$	1.000	0.000	1.000	0.000	0.776	0.150	1	CP-odd
$f_0(1370)$	-1.180 ± 0.084	1.371 ± 0.087	1.809	2.282	1.434	0.173	0	CP-even
$f_0(980)$	-0.405 ± 0.004	-0.265 ± 0.006	0.484	-2.563	0.975	0.044	0	CP-even
$f_2(1270)$	0.687 ± 0.017	-0.130 ± 0.015	0.699	-0.187	1.275	0.185	2	CP-even
$\omega(782)$	-0.017 ± 0.001	0.038 ± 0.001	0.042	1.992	0.783	0.008	1	CP-odd
σ	-1.890 ± 0.025	-0.700 ± 0.025	2.015	-2.787	0.528	0.512	0	CP-even
σ'	-0.323 ± 0.008	-0.084 ± 0.008	0.334	-2.888	1.033	0.099	0	CP-even
$K^0_S\pi^-$								
$K^*(892)^-$	-1.211 ± 0.007	1.231 ± 0.007	1.727	2.348	0.894	0.046	1	Flavour
$K^*_0(1430)^-$	1.702 ± 0.014	1.072 ± 0.017	2.011	0.562	1.459	0.175	0	Flavour
$K^*_2(1430)^-$	0.866 ± 0.014	-0.784 ± 0.019	1.168	-0.736	1.426	0.099	2	Flavour
$K^*(1680)^-$	-1.167 ± 0.059	-0.131 ± 0.040	1.174	-3.030	1.677	0.205	1	Flavour
$K^0_S\pi^+$								
$K^*(892)^+$	0.114 ± 0.003	-0.114 ± 0.003	0.161	-0.785	0.894	0.046	1	Flavour
$K^*_0(1430)^+$	0.155 ± 0.011	0.085 ± 0.013	0.177	0.502	1.459	0.175	0	Flavour
$K^*_2(1430)^+$	0.073 ± 0.014	-0.070 ± 0.013	0.101	-0.764	1.426	0.099	2	Flavour
$K^*(1680)^+$	1.448 ± 0.042	-0.944 ± 0.047	1.729	-0.578	1.677	0.205	1	Flavour
$K^0_S\pi^+\pi^-$								
NR	-0.691 ± 0.132	3.469 ± 0.108	3.538	1.768	0.000	0.000	0	CP-even

Table 6.4: Fit results for the complex amplitudes, relative to $\rho(770)$, of the resonances used in the isobar model.

Chapter 7

Systematic cross checks

This chapter describes tests of the fit's robustness and bias, and our procedure for choosing the optimum tradeoff of purity versus sample size. Throughout, when a systematic uncertainty is given in percent, this should be taken as an absolute rather than relative measurement. That is, if the uncertainty were given as 0.1%, the measurement would be $(x \pm 0.1)\%$

7.1 General procedure

The purpose of these tests is to convince ourselves that the mixing fit PDF is self-consistent and robust. We therefore generate fake or 'toy' data sets using the EvtGen framework (Ref. [28]) adapted for *BABAR* , which we also use for our full Monte Carlo event sample, but applying no detector effects or resolution. For this purpose we generate only the lifetime and Dalitz distribution of the D^0, and no reconstruction simulation is done - we look directly at the generated quantities. We generate several different combinations of mixing parameters, and for each combination we generate several samples. This allows us to cross-check the reported fit error by comparing it with the RMS of the distribution of reported mixing parameters. For example, in the first row of Table 7.1, the average error in x reported by the ten different fits is 0.076%. The RMS of the fit values for x is 0.057%, which is roughly comparable.

After these toy Monte Carlo tests have been completed, we proceed to full Monte Carlo. Here EvtGen simulates complete e^+e^- collisions under the constraint that the full event contain a D^* decaying through $D^0\pi$, with the D^0 in turn going to $K_s\pi\pi$. We then simulate the full reconstruction algorithm of the *BABAR* detector and of this analysis, and again attempt to fit the resulting samples, to check the extracted mixing parameters against those generated.

7.1.1 Note on 'free will'

The MINUIT fit algorithm considers itself to have converged when its EDM, estimated distance to minimum, drops below a threshold value, usually 10^{-3}. It follows that, although the true minimum is a single point in parameter space, fit results can be anywhere in a many-dimensional sphere surrounding that point. Further, the particular point at which MINUIT crosses this sphere and finds that it has converged depends on the path taken. It follows that small differences in initial conditions can lead to noticeable differences in the fit result. This is similar to the phenomenon of 'chaos' in, eg, weather simulations, but differs in that MINUIT is constrained to end up somewhere close to the true solution (assuming convergence).

We refer to this sensitivity to the path taken as 'free will', because we initially became aware of it by running the same fit twice and getting different results. Since computers are deterministic (and no random numbers are used in the algorithm), this was puzzling, even in light of the argument above, because the initial conditions (including the starting values of the fit parameters) were *exactly* the same, bit for bit. Sensitivity to, say, differences in the twelfth decimal point ought to be irrelevant when numbers were genuinely identical down to the sixty-fourth bit. Hence 'free will' - it appeared that the computers had somehow lost their deterministic character.

The explanation turned out to lie in small differences in machine architecture; the computers making up the batch farms at SLAC are not completely homogenous. Tiny differences in their roundoff errors when multiplying very large by very small numbers (of order 10^{80} and 10^{-80} - such numbers crop up in the evaluation of the convolution functions) added up and

eventually led to slightly different answers for the mixing parameters. Since such differences are already included in the MINUIT error estimate, and in any case the effect is tiny, we do not assign a corresponding systematic. It is mentioned here for completeness and as a possible warning of the coming robot uprising.

7.2 Toy Monte Carlo tests

It is possible for bias to occur due to low statistics. This effect is easier to discuss by analogy, in a simple case where the PDF is amenable to calculation by humans; in particular, the case of measuring particle momentum from the curvature of a track. (My explanation follows [29].) Consider a uniform magnetic field, in which we measure a particle trajectory by taking points at regular intervals with a known Gaussian resolution. We then measure the curvature with an unbiased Gaussian distribution. But the momentum is inverse to the curvature. If the true curvature (in arbitrary units) is 5, and the true momentum is 0.2, we might make curvature measurements of 4, 5, and 6. This averages to 5, as expected. But the corresponding momentum measurements average to $(1/4 + 1/5 + 1/6)/3 = 0.21$, larger than the true value. Such bias can be significant even with large statistics, as shown by the toy results in Table 7.5. For this simple case one can get better results by calculating the average curvature first, and only then inverting.

In the case of our mixing measurement, the source of bias is not so simple; we are not measuring x and y directly, we are measuring a distribution of D^0 decay-time variations across the Dalitz plot, which depends on the mixing parameters in a complicated way. The possibility of a low-statistics bias therefore exists, and we test for it by generating a large number of events without detector resolution effects, efficiency, or background (hence 'toy' Monte Carlo) and fitting (keeping resonance amplitudes fixed for simplicity at this stage) in two ways: First, by splitting into several independent sub-samples, and second, by combining all the samples into one. If the sub-samples show a bias while the large combined sample doesn't, there is a low-statistics bias at work. Tables 7.1 and 7.2 show the results. Although

True (x, y) [%]	Sample	Results for x [%]				Results for y [%]			
		$\langle$Result$\rangle$	$\langle x - x_{in} \rangle$	$\langle$Error$\rangle$	RMS/$\sqrt{n-1}$	$\langle$Result$\rangle$	$\langle y - y_{in} \rangle$	$\langle$Error$\rangle$	RMS/$\sqrt{n-1}$
(1.00, 1.00)	10 × 2M	0.950	-0.050	0.076	0.019	0.926	-0.074	0.067	0.020
(1.00, -1.00)	10 × 2M	0.976	-0.024	0.077	0.026	-1.128	-0.128	0.066	0.026
(1.00, 0.000)	10 × 2M	0.999	-0.001	0.076	0.021	-0.123	-0.123	0.067	0.016
(-1.00, 1.00)	10 × 2M	-1.022	-0.022	0.075	0.020	0.915	-0.085	0.068	0.028
(-1.00, -1.00)	10 × 2M	-1.015	-0.015	0.077	0.020	-1.103	-0.103	0.066	0.023
(-1.00, 0.000)	10 × 2M	-1.061	-0.061	0.076	0.026	-0.079	-0.079	0.067	0.016
(0.000, 1.00)	10 × 2M	-0.059	-0.059	0.075	0.022	0.894	-0.106	0.068	0.030
(0.000, -1.00)	10 × 2M	-0.028	-0.028	0.077	0.015	-1.104	-0.104	0.066	0.022
(0.000, 0.000)	10 × 2M	-0.033	-0.033	0.076	0.021	-0.087	-0.087	0.067	0.028
(0.50, 0.50)	10 × 2M	0.483	-0.017	0.076	0.018	0.387	-0.113	0.067	0.028
(0.50, -0.50)	10 × 2M	0.445	-0.056	0.081	0.025	-0.582	-0.082	0.064	0.027
(-0.50, 0.50)	10 × 2M	-0.547	-0.047	0.075	0.028	0.412	-0.088	0.067	0.018
(-0.50, -0.50)	10 × 2M	-0.510	-0.010	0.077	0.018	-0.585	-0.085	0.066	0.024

Table 7.1: Results of fitting to toy Monte Carlo using samples of 2 million events each. Both x and y display a bias; the fit result is consistently smaller than the generated value.

True (x, y) [%]	Sample	Results for x [%]				Results for y [%]			
		$\langle$Result$\rangle$	$\langle x - x_{in} \rangle$	$\langle$Error$\rangle$	RMS/$\sqrt{n-1}$	$\langle$Result$\rangle$	$\langle y - y_{in} \rangle$	$\langle$Error$\rangle$	RMS/$\sqrt{n-1}$
(1.00, 1.00)	1×20M	0.950	-0.050	0.024	-	0.926	-0.074	0.021	-
(1.00, -1.00)	1×20M	0.974	-0.026	0.024	-	-1.126	-0.126	0.021	-
(1.00, 0.000)	1×20M	0.999	-0.001	0.024	-	-0.123	-0.123	0.021	-
(-1.00, 1.00)	1×20M	-1.024	-0.024	0.024	-	0.913	-0.087	0.021	-
(-1.00, -1.00)	1×20M	-1.020	-0.020	0.024	-	-1.102	-0.102	0.021	-
(-1.00, 0.000)	1×20M	-1.061	-0.061	0.024	-	-0.079	-0.079	0.021	-
(0.000, 1.00)	1×20M	-0.059	-0.059	0.024	-	0.894	-0.106	0.021	-
(0.000, -1.00)	1×20M	-0.028	-0.028	0.024	-	-1.104	-0.104	0.021	-
(0.000, 0.000)	1×20M	-0.033	-0.033	0.024	-	-0.087	-0.087	0.021	-
(0.50, 0.50)	1×20M	0.483	-0.017	0.024	-	0.387	-0.113	0.021	-
(0.50, -0.50)	1×20M	0.435	-0.065	0.025	-	-0.577	-0.077	0.021	-
(-0.50, 0.50)	1×20M	-0.546	-0.046	0.024	-	0.411	-0.089	0.021	-
(-0.50, -0.50)	1×20M	-0.510	-0.010	0.024	-	-0.584	-0.084	0.021	-

Table 7.2: Results of fitting to toy Monte Carlo using samples of 20 million events each. The mixing parameters show a bias very similar to that in Table 7.1.

True (x, y) [%]	Sample	Results for x [%]				Results for y [%]			
		$\langle$Result$\rangle$	$\langle x - x_{in} \rangle$	$\langle$Error$\rangle$	RMS/$\sqrt{n-1}$	$\langle$Result$\rangle$	$\langle y - y_{in} \rangle$	$\langle$Error$\rangle$	RMS/$\sqrt{n-1}$
(1.00, 1.00)	10 × 2M	0.965	-0.035	0.075	0.022	0.972	-0.028	0.067	0.015
(1.00, -1.00)	10 × 2M	0.971	-0.029	0.077	0.027	-1.021	-0.021	0.066	0.031
(1.00, 0.000)	10 × 2M	0.993	-0.007	0.076	0.027	0.051	0.051	0.066	0.016
(-1.00, 1.00)	10 × 2M	-0.981	0.019	0.074	0.019	1.028	0.028	0.068	0.017
(-1.00, -1.00)	10 × 2M	-0.969	0.031	0.076	0.024	-1.024	-0.024	0.066	0.016
(-1.00, 0.000)	10 × 2M	-1.016	-0.016	0.075	0.016	0.005	0.005	0.067	0.016
(0.000, 1.00)	10 × 2M	-0.001	-0.001	0.075	0.030	1.018	0.018	0.067	0.012
(0.000, -1.00)	9 × 2M	-0.027	-0.027	0.077	0.019	-1.001	-0.001	0.066	0.019
(0.000, 0.000)	9 × 2M	0.031	0.031	0.076	0.029	0.017	0.017	0.066	0.018
(0.50, 0.50)	10 × 2M	0.481	-0.019	0.076	0.021	0.464	-0.036	0.067	0.025
(0.50, -0.50)	10 × 2M	0.474	-0.026	0.077	0.014	-0.494	0.006	0.066	0.015
(-0.50, 0.50)	10 × 2M	-0.487	0.013	0.075	0.016	0.468	-0.032	0.067	0.027
(-0.50, -0.50)	10 × 2M	-0.459	0.041	0.076	0.026	-0.499	0.001	0.067	0.020

Table 7.3: Results of fitting to toy Monte Carlo without radiative events. The bias from Tables 7.1 and 7.1 has disappeared.

True (x, y) [%]	Sample	Results for x [%]				Results for y [%]			
		$\langle$Result$\rangle$	$\langle x - x_{in} \rangle$	$\langle$Error$\rangle$	RMS/$\sqrt{n-1}$	$\langle$Result$\rangle$	$\langle y - y_{in} \rangle$	$\langle$Error$\rangle$	RMS/$\sqrt{n-1}$
(1.00, 1.00)	8 × 2M	0.986	-0.014	0.107	0.043	1.041	0.041	0.095	0.032
(1.00, -1.00)	10 × 2M	1.009	0.009	0.109	0.032	-1.046	-0.046	0.094	0.034
(1.00, 0.000)	10 × 2M	0.987	-0.013	0.108	0.045	-0.084	-0.084	0.094	0.020
(-1.00, 1.00)	9 × 2M	-0.987	0.013	0.106	0.038	0.984	-0.016	0.096	0.043
(-1.00, -1.00)	8 × 2M	-0.985	0.015	0.108	0.052	-0.992	0.008	0.094	0.030
(-1.00, 0.000)	9 × 2M	-1.018	0.018	0.107	0.034	-0.049	-0.049	0.095	0.028
(0.000, 1.00)	9 × 2M	0.034	0.034	0.107	0.032	1.034	0.034	0.095	0.048
(0.000, -1.00)	8 × 2M	-0.002	-0.002	0.109	0.020	-1.033	-0.033	0.096	0.046
(0.000, 0.000)	10 × 2M	0.000	0.000	0.108	0.025	0.005	0.005	0.094	0.036
(0.50, 0.50)	10 × 2M	0.495	-0.005	0.108	0.030	0.484	-0.016	0.095	0.043
(0.50, -0.50)	9 × 2M	0.465	-0.035	0.108	0.036	-0.474	0.026	0.094	0.048
(-0.50, 0.50)	8 × 2M	-0.520	-0.020	0.107	0.015	0.507	0.007	0.095	0.022
(-0.50, -0.50)	4 × 2M	-0.549	-0.049	0.116	0.068	-0.447	0.053	0.101	0.068

Table 7.4: Results of fitting to toy Monte Carlo with radiative events and resonance parameters left free. The bias from Tables 7.1 and 7.1 is gone.

Number of events	Average curvature	Average momentum
10	5.4203 ± 0.2028	0.1872 ± 0.0073
100	5.0426 ± 0.0996	0.2071 ± 0.0047
1000	4.9854 ± 0.0333	0.2112 ± 0.0017
10000	4.9885 ± 0.0101	0.2100 ± 0.0005
100000	4.9965 ± 0.0032	0.2094 ± 0.0002
1000000	5.0006 ± 0.0010	0.20921 ± 0.00005

Table 7.5: Results of randomly generating 'curvature' measurements. The curvature is distributed as a Gaussian with mean 5 and standard deviation 1; the momentum is the inverse of the curvature. Notice the very slow convergence of the momentum results to the true value of 0.2.

there is a small bias of around -0.1% in y, and roughly -0.03% in x, it is quite consistent between the two methods; we therefore conclude that sample size is not its source.

This toy Monte Carlo is also useful for testing for bias due to radiative decays. $D^0 \to K_S\pi^+\pi^-\gamma$ decays with a low-energy photon are signal events for a mixing measurement. However, the additional photon shifts the (m_+^2, m_-^2) Dalitz plot of these events slightly down and to the left, which may lead to a bias in the fit result. Table 7.3 shows the result of turning off radiative events when generating the toy Monte Carlo. These fits show no bias in either mixing parameter. It follows that the radiative events modelled by the PHOTOS program do cause a small bias. Figure 7.1 shows the energy-loss spectrum.

The fits to toy Monte Carlo discussed so far have permitted only the D^0 lifetime and the two mixing parameters to float; the amplitudes and phases of the isobar-model resonances have been kept fixed. Table 7.4 shows what occurs when these parameters are left free. The biases found in Table 7.1 now disappear. They are no doubt replaced by some bias in the parameters of the resonance model, relative to what was used to generate the events; but for purposes of measuring mixing, this is a second-order effect. The 'PHOTOS bias', therefore, can be neglected.

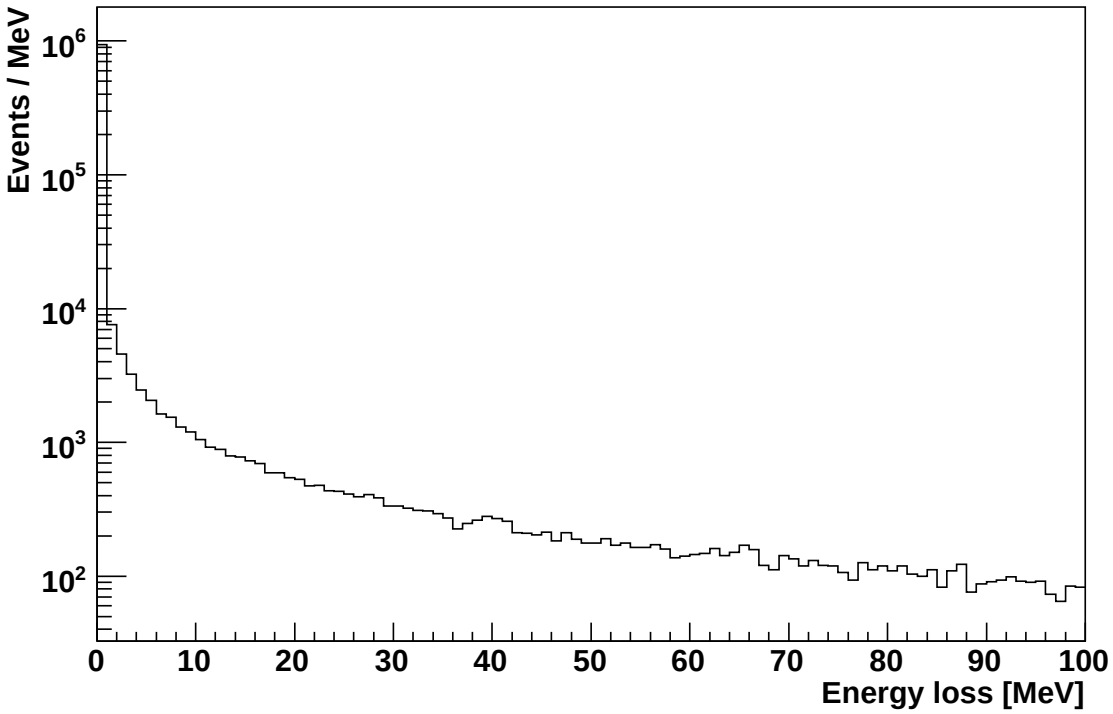

Figure 7.1: Spectrum of energy radiated by D^0 mesons in Monte Carlo simulations using PHOTOS.

Sample size [thousands]	Error on x [%]	Error on y [%]
10000	0.15	0.13
1000	0.48	0.42
100	1.54	1.30
10	7.53	9.58

Table 7.6: Reported fit errors from different-sized signal Monte Carlo samples. Sample sizes are shown prior to selection cuts.

7.3 Full Monte Carlo tests

The next step is to test for bias in the full signal Monte Carlo. Notice that at this stage the only backgrounds are from mis-reconstruction of signal events, which are relatively tiny. As with the preceding toy tests, several different samples are generated for varying mixing parameters; because this full Monte Carlo is much more computationally expensive, there are fewer samples. Specifically, we generate five samples for each of six different (x, y) pairs, namely $(\pm 1\%, \pm 1\%)$, $(0, 0)$, and $(25\%, 25\%)$. Each sample contains two million signal events before cuts, which gives a size comparable to the data sample after reconstruction. Where we consider samples separately, we number them 1 through 5. These full Monte Carlo events are passed through the selection steps described in Chapter 4 and fitted using the signal PDF from Chapter 6.

7.3.1 Nominal ('vanilla') fit

Table 7.7 shows the results; there is an overall bias of roughly 0.1% on both x and y. We assign this value as a fit bias' systematic error to both mixing parameters. We refer to the results from this fit as the 'vanilla' numbers, and use them as the base for comparisons in other MC cross-checks.

As a point of interest, Table 7.6 shows the reported fit error for the mixing parameters using different sample sizes. The dependence is roughly $1/\sqrt{N}$ until very small sample sizes are reached.

7.3.2 Cross check with D^0 mass constraint

Table 7.8 shows the same results when the mass constraint is applied in the kinematic fit for the D^0 decay. The central values (and bias) are unaffected, while the statistical uncertainties show a tiny improvement, on the order of 0.005%. This is unexpectedly small, since the mass-constrained fit reduces both the spread of pull values across the signal window and the average σ_t. The smallness of the effect is probably due to the many other parameters in the fit, which contribute to the reported error on the mixing parameters. As a consequence, we do not use the mass-constrained information, since it does not meaningfully improve our errors or bias.

7.3.3 Cross check with m_+ and m_- resolution

The measurement of m_+ and m_- is not perfect, having a resolution of a few MeV/c^2, as shown in Figure 7.2. To test whether this is the cause of the observed bias in the mixing parameters, we redo the above fits using the generated, rather than reconstructed, values for the invariant masses. Tables 7.9 and 7.10 show the resulting changes in the reported mixing parameters for each Monte Carlo sample; in these and all subsequent per-sample deviation tables, each entry is the 'vanilla' fit result minus the fit result from the changed fit. Although there is a systematic change between the fits to generated and reconstructed values, it is in the *wrong direction* to account for the bias above; the bias would actually be worse if the true values were used! This is unexpected, but may be explained by the masses and widths used for the isobar resonances, which were found in a fit to reconstructed values and kept fixed, and thus are not really suited to describing the true values.

True (x, y) [%]	Sample	Results for x [%]				Results for y [%]			
		$\langle$Result$\rangle$	$\langle x - x_{in} \rangle$	$\langle$Error$\rangle$	RMS/$\sqrt{n-1}$	$\langle$Result$\rangle$	$\langle y - y_{in} \rangle$	$\langle$Error$\rangle$	RMS/$\sqrt{n-1}$
(1.00, 1.00)	5 × 2M	0.822	-0.178	0.334	0.128	1.005	0.005	0.295	0.124
(1.00, -1.00)	5 × 2M	1.036	0.036	0.324	0.116	-0.937	0.063	0.271	0.085
(-1.00, 1.00)	5 × 2M	-0.877	0.123	0.328	0.154	1.006	0.006	0.272	0.129
(-1.00, -1.00)	5 × 2M	-0.974	0.026	0.321	0.084	-0.922	0.078	0.273	0.092
(25.00, 25.00)	5 × 2M	24.949	-0.051	0.382	0.188	25.017	0.017	0.281	0.062
(0.000, 0.000)	5 × 2M	0.168	0.168	0.321	0.068	0.089	0.089	0.272	0.121
		Results for τ [fs]				Results for offset [fs]			
		$\langle$Result$\rangle$	$\langle \tau - \tau_{in} \rangle$	$\langle$Error$\rangle$	RMS/$\sqrt{n-1}$	$\langle$Result$\rangle$		$\langle$Error$\rangle$	RMS/$\sqrt{n-1}$
(1.00, 1.00)	5 × 2M	410.346	-0.654	1.310	0.881	0.952		1.127	0.656
(1.00, -1.00)	5 × 2M	411.035	0.035	1.225	0.688	1.017		1.049	0.156
(-1.00, 1.00)	5 × 2M	409.709	-1.291	1.221	0.831	1.601		1.049	0.540
(-1.00, -1.00)	5 × 2M	411.467	0.467	1.226	0.541	0.924		1.050	0.326
(25.00, 25.00)	5 × 2M	410.679	-0.321	1.558	0.532	0.531		1.097	0.584
(0.000, 0.000)	5 × 2M	411.183	0.183	1.216	0.524	0.379		1.050	0.231

Table 7.7: Results of fitting to full Monte Carlo samples. (Notice that there is no 'input' offset, hence there is no column for the difference between fit result and generated value.)

True (x, y) [%]	Sample	Results for x [%]				Results for y [%]			
		$\langle$Result$\rangle$	$\langle$Error$\rangle$	RMS/$\sqrt{n-1}$	$\langle$Result$\rangle$	$\langle$Error$\rangle$	RMS/$\sqrt{n-1}$		
(1.00, 1.00)	5 × 2M	0.781	-0.219	0.330	0.129	0.942	-0.058	0.289	0.115
(1.00, -1.00)	5 × 2M	1.054	0.054	0.319	0.118	-1.022	-0.022	0.268	0.079
(-1.00, 1.00)	5 × 2M	-0.951	0.049	0.323	0.167	0.906	-0.094	0.266	0.102
(-1.00, -1.00)	5 × 2M	-0.952	0.048	0.313	0.075	-1.023	-0.023	0.269	0.093
		Results for τ [fs]				Results for offset [fs]			
		$\langle$Result$\rangle$	$\langle$Error$\rangle$	RMS/$\sqrt{n-1}$	$\langle$Result$\rangle$		$\langle$Error$\rangle$	RMS/$\sqrt{n-1}$	
(1.00, 1.00)	5 × 2M	410.788	-0.212	1.263	0.828	0.036		1.053	0.530
(1.00, -1.00)	5 × 2M	411.476	0.476	1.177	0.779	0.435		0.992	0.178
(-1.00, 1.00)	5 × 2M	410.314	-0.686	1.182	0.759	0.924		0.979	0.380
(-1.00, -1.00)	5 × 2M	411.744	0.744	1.189	0.706	0.602		1.001	0.381

Table 7.8: Results of fitting to full Monte Carlo samples using a mass-constrained fit for the D^0 decay. The bias in the mixing parameters is similar to that in Table 7.7.

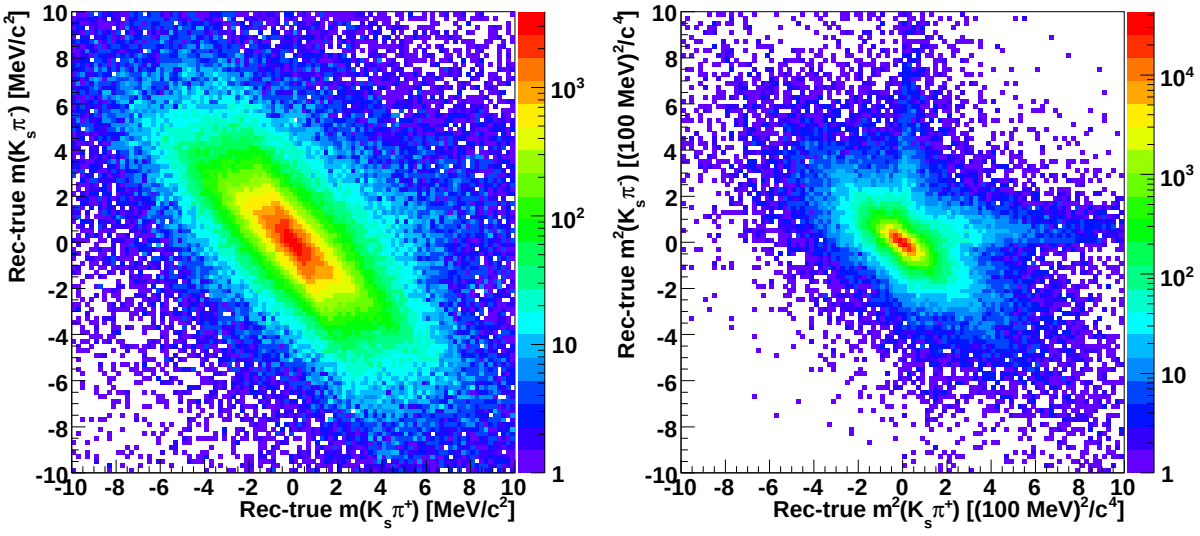

Figure 7.2: Resolution of the Dalitz variables. The horizontal and vertical tails are due to radiating pions; there is more phase space for increasing than for decreasing the reconstructed parent mass (by increasing rather than decreasing the opening angle between pion and kaon).

True (x, y) [%]	Sample 1	Sample 2	Sample 3	Sample 4	Sample 5
(1.00, 1.00)	-0.029	-0.118	-0.057	-0.121	-0.117
(1.00, -1.00)	-0.065	-0.025	-0.016	-0.141	-0.076
(-1.00, 1.00)	-0.047	-0.107	-0.061	-0.062	-0.118
(-1.00, -1.00)	-0.061	-0.214	-0.032	-0.123	-0.081

Table 7.9: Change in fit result (in 10^{-2}) for x for individual samples using the true (rather than reconstructed) Dalitz-plot variables. The average deviation is -0.083%, the RMS is 0.048%, and the correlation with the y deviations reported in Table /reftable:massresDeltaY is -0.21.

True (x, y) [%]	Sample 1	Sample 2	Sample 3	Sample 4	Sample 5
(1.00, 1.00)	0.038	0.055	-0.003	0.030	0.026
(1.00, -1.00)	0.007	-0.003	-0.031	-0.007	0.007
(-1.00, 1.00)	0.046	0.057	-0.003	-0.028	-0.082
(-1.00, -1.00)	0.057	0.060	-0.007	-0.019	0.016

Table 7.10: Change in fit result (in 10^{-2}) for y for individual samples using the true (rather than reconstructed) Dalitz-plot variables. The average deviation is 0.01%, the RMS is 0.035%, and the correlation with the x deviations reported in Table 7.9 is -0.21.

7.4 Misalignment tests

The positions of the 340 individual detector elements, known as wafers, within the SVT tracking system are not perfectly constant (at the level of micrometers) over time. Ref. [30] describes the procedure *BABAR* uses to measure deviations of the actual wafer positions from nominal. Since the mixing parameters are very sensitive to decay times, and decay times are sensitive to position measurements, these misalignments are a possible source of systematic error. To assess this, we use Monte Carlo events generated with the SVT wafers deliberately misaligned. We use five different misalignment files; each file contains six parameters for each wafer, three showing displacement and three showing rotation from the nominal position. Four of these files are generated from differences between successive measurements of the wafer alignments, and thus represent the time dependence of the wafer positions; fits using these misalignments are labelled 'maTime$N$' with N going from 1 through 4. The fifth is generated by shifting each layer of wafers in the z direction, the amount of shift being proportional to the radius of the wafer layer; this boost bias (label 'maBoost') is intended to test the effect of systematic shifts in wafer positions.

Doing tests with misalignment requires a full reconstruction of each event, down to fitting individual detector hits to make tracks; it is very computationally expensive. Consequently we are unable to use as many different samples as in the previous section. Instead we have 8 million events, generated with $x = y = 1\%$, which we split into four samples each of 2 million (before reconstruction) and label 0 through 3.

Misalignment was originally detected through azimuthal asymmetries in lifetime and mass measurements. Figure 7.3 shows the dependence of measured D^0 lifetime and mass on azimuthal angle for data; Figures 7.4 and 7.5 show the same effects for sample 0, with and without misalignment; the corresponding plots for the other samples are consistent with these. The misalignment files represent upper bounds on the shifts that occur over time, and the azimuthal dependence of τ is correspondingly more dramatic; it follows that the systematic uncertainty may be overestimated using these files. Table 7.11 shows the mixing parameters obtained by doing the full mixing analysis on Monte Carlo samples reconstructed

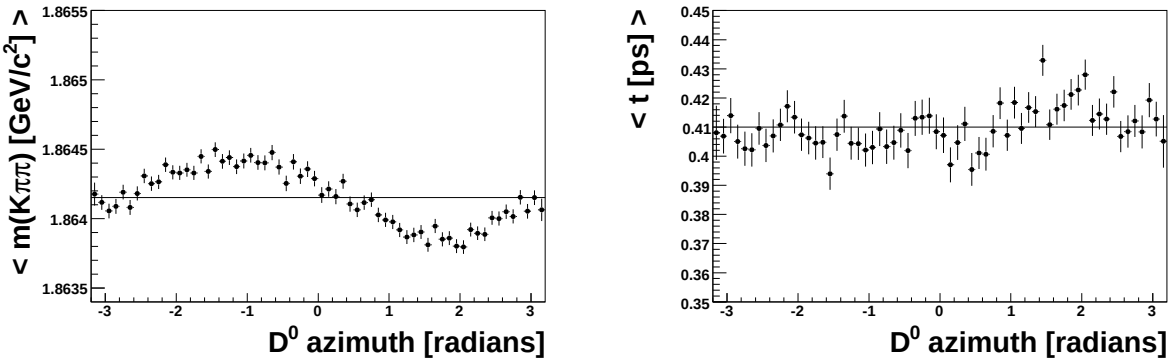

Figure 7.3: Average m_{D^0} (left) and D^0 decay time (right) in data as a function of azimuthal angle.

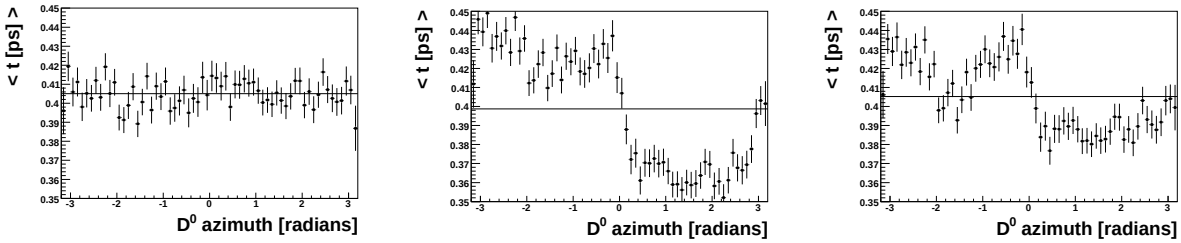

No misalignment

maTime1

maTime3

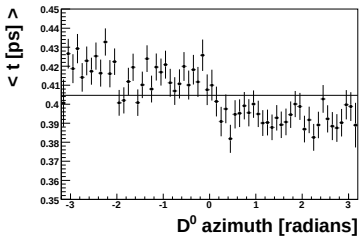

maBoost

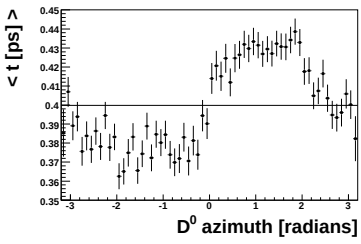

maTime2

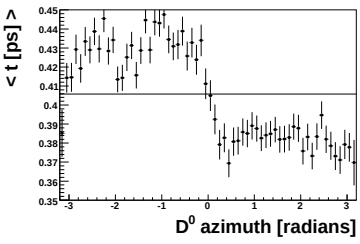

maTime4

Figure 7.4: Dependence of D^0 decay time on D^0 azimuthal angle for Monte Carlo sample 0 with different misalignments. Note that the effect is much larger than that shown in Figure 7.3.

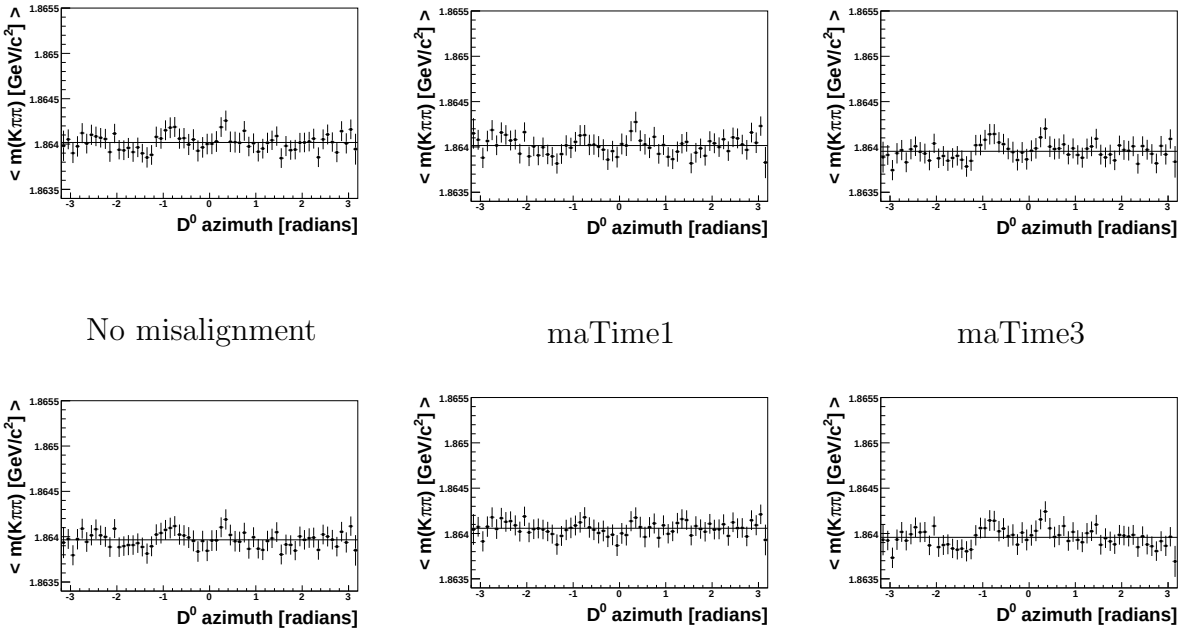

No misalignment maTime1 maTime3

maBoost maTime2 maTime4

Figure 7.5: Dependence of measured D^0 mass time on D^0 azimuthal angle for Monte Carlo sample 0 with different misalignments. Note that the effect is smaller than that shown in Figure 7.3.

with each of these misalignments, to be compared with the 'vanilla' result where no misalignment was used. (Note that this use of vanilla is different from that in the previous section.) Tables 7.12 and 7.13 show the per-sample deviations of the misaligned from the vanilla events. The RMS of these deviations, rounded to 0.1%, is taken as the systematic uncertainty due to misalignment of the SVT elements.

Misalignment	Sample	Results for x [%]				Results for y [%]			
		$\langle$Result$\rangle$	$\langle x - x_{in} \rangle$	$\langle$Error$\rangle$	RMS/$\sqrt{n-1}$	$\langle$Result$\rangle$	$\langle y - y_{in} \rangle$	$\langle$Error$\rangle$	RMS/$\sqrt{n-1}$
vanilla	4×2M	1.385	0.385	0.338	0.225	0.824	-0.176	0.299	0.178
maTime1	4×2M	1.414	0.414	0.339	0.218	0.890	-0.110	0.304	0.138
maTime2	4×2M	1.405	0.405	0.338	0.245	0.875	-0.125	0.306	0.141
maTime3	4×2M	1.424	0.424	0.338	0.229	0.932	-0.068	0.304	0.128
maTime4	4×2M	1.396	0.396	0.338	0.231	0.935	-0.065	0.305	0.150
maBoost	4×2M	1.406	0.406	0.338	0.233	0.935	-0.065	0.304	0.143
		Results for τ [fs]				Results for offset [fs]			
		$\langle$Result$\rangle$	$\langle \tau - \tau_{in} \rangle$	$\langle$Error$\rangle$	RMS/$\sqrt{n-1}$	$\langle$Result$\rangle$		$\langle$Error$\rangle$	RMS/$\sqrt{n-1}$
vanilla	4×2M	410.940	-0.060	1.320	0.299	0.312		1.142	0.675
maTime1	4×2M	413.316	2.316	1.352	0.468	-10.044		1.155	0.832
maTime2	4×2M	409.045	-1.955	1.339	0.512	-1.230		1.159	0.684
maTime3	4×2M	412.820	1.820	1.346	0.485	-2.673		1.151	0.853
maTime4	4×2M	412.037	1.037	1.338	0.545	-0.101		1.150	0.869
maBoost	4×2M	411.981	0.981	1.345	0.461	-1.111		1.151	0.807

Table 7.11: Results of fitting to signal Monte Carlo samples with misaligned SVT wafers. The generated mixing parameters are $x = y = 1\%$. Notice that these sets of samples are not independent; the same underlying events have been reconstructed with different misalignment files.

Misalignment	Sample 0	Sample 1	Sample 2	Sample 3
maTime1	-0.081	0.004	0.081	-0.119
maTime2	-0.037	-0.063	0.158	-0.138
maTime3	-0.084	-0.043	0.037	-0.069
maTime4	-0.061	-0.012	0.139	-0.113
maBoost	-0.112	-0.021	0.130	-0.084

Table 7.12: Change in fit result (in 10^{-2}) for x for misaligned individual samples with respect to the fit of the 'vanilla' MC. The average deviation is -0.024%, the RMS is 0.087%, and the correlation with the y deviation (Table 7.13) is 65.4%.

Misalignment	Sample 0	Sample 1	Sample 2	Sample 3
maTime1	-0.046	-0.050	0.022	-0.190
maTime2	0.005	-0.056	0.013	-0.165
maTime3	-0.093	-0.119	0.016	-0.235
maTime4	-0.069	-0.038	-0.075	-0.261
maBoost	-0.111	-0.083	-0.023	-0.224

Table 7.13: Change in fit result (in 10^{-2}) for y for misaligned individual samples with respect to the fit of the 'vanilla' MC. The average deviation is -0.089%, the RMS is 0.084%, and the correlation with the x deviations (Table 7.12) is 65.4%.

7.5 D^0 mass test

The measured D^0 decay time is correlated with the measured D^0 mass, as shown for signal Monte Carlo in Figure 7.6. The reason is shown schematically in Figure 7.7: When varying the position of the D^0 vertex in the direction parallel to its momentum, two things happen. First, the angle between its daughters' momenta will be either opened or closed, and this changes the reconstructed D^0 mass; second, the flight length will be changed, and it is from the flight length that we calculate the decay time. Since we measure the mixing parameters precisely by their effect on D^0 decay times, it follows that an uncertainty in the D^0 mass may translate to a systematic uncertainty in the mixing parameters. To test this, we repeat the study of Section 7.3 (using the decay time from the non-mass-constrained kinematic fit) with the window of accepted D^0 masses moved. For each sample, the mixing fit is repeated with the D^0 mass window either moved up by half an MeV/c^2, or down by the same amount. Half an MeV/c^2 is a little larger than the difference between the value used in our Monte Carlo, 1864.5 MeV/c^2, and the peak value we see in the data, 1864.1 MeV/c^2. The Monte Carlo value is the 2006 world average [21]; hence the half-an-MeV change is a reasonable estimate of our uncertainty about the D^0 mass as measured by the *BABAR* detector. Tables 7.15 and 7.16 show the resulting averages; Figure 7.8 compares the pull distributions for each mass window.

A better way to consider this effect, however, is to look at the change in each Monte Carlo sample, instead of averages over sets of five samples, as the mass window is moved either up or down. Tables 7.17 through 7.20 show the change in fit result for each sample relative to the fit with the default mass window. Figure 7.9 shows the distribution of the difference between the change in the upward-moved sample and that in the downward-moved sample; this difference is a per-sample estimate of the effect of changing the mass window. It is clear that the upward-moved samples have consistently higher values than the downward-moved samples, and therefore that the D^0 mass window used will influence the mixing parameters. In particular, a change of 1 MeV/c^2 induces an average change of $\sim$0.05% in both mixing parameters; this small effect is washed out by the statistical uncertainty of

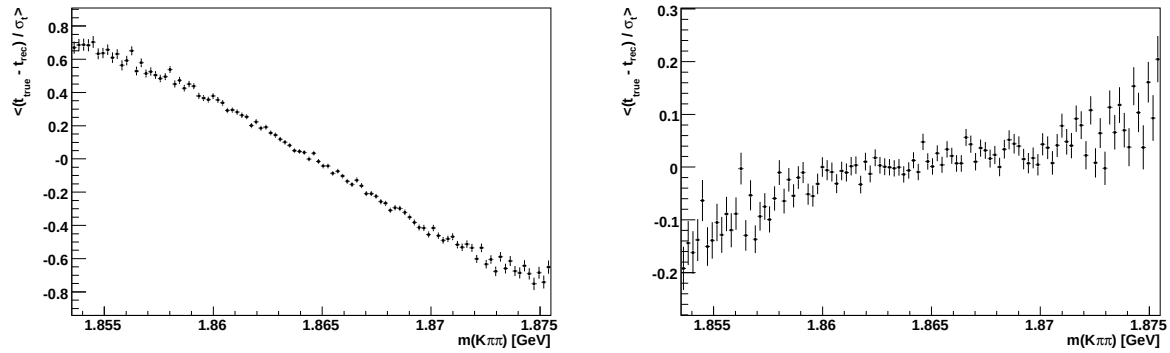

Figure 7.6: Average difference between generated and reconstructed decay times, in units of the error from the kinematic fit, as a function of reconstructed D^0 mass. The events are signal Monte Carlo. The left-hand plot has no mass constraint in the kinematic fit, the right-hand plot does.

$\sim$0.3% when comparing averages and pull distributions, as in the previous paragraph, but shows up in a per-sample comparison since the fit results for the different mass windows are not independent.

Taking the uncertainty in our measurement of the D^0 mass as 0.5 MeV/c^2 - as noted, a little more than the difference between the 2006 PDG value and our average - and the effect of moving the mass window as 0.05% per MeV moved, the corresponding systematic uncertainty in the mixing parameters is 0.025%.

In Tables 7.21 through 7.24 the per-sample study is repeated using the decay time from the mass-constrained kinematic fit; as shown in Figure 7.10, there is still a systematic effect on the mixing parameters, although its sense is reversed. This agrees with the reversal of the decay time's dependence on the D^0 mass shown in Figure 7.6.

Change in mass window [MeV/c^2]	Δx [%]	Δy [%]
+0.5	-0.028	0.020
-0.5	-0.004	-0.058

Table 7.14: Change in fit result for data with the mass window moved up or down.

Table 7.14 shows the changes in the mixing parameters when the mass window is moved in a fit to data; the numbers are compatible with the results from Monte Carlo.

D^0 window move [MeV/c^2]	True (x, y) [%]	Sample	Results for x [%]			Results for y [%]		
			⟨Result⟩	⟨Error⟩	RMS/$\sqrt{n-1}$	⟨Result⟩	⟨Error⟩	RMS/$\sqrt{n-1}$
0.5	(1.00, 1.00)	5 × 2M	1.084	0.329	0.137	0.951	0.290	0.122
0.0	(1.00, 1.00)	5 × 2M	1.058	0.329	0.143	0.940	0.291	0.130
-0.5	(1.00, 1.00)	5 × 2M	1.017	0.333	0.140	0.923	0.295	0.138
0.5	(1.00, -1.00)	5 × 2M	1.035	0.314	0.167	-0.908	0.263	0.044
0.0	(1.00, -1.00)	5 × 2M	0.995	0.314	0.144	-0.964	0.264	0.062
-0.5	(1.00, -1.00)	5 × 2M	0.956	0.314	0.158	-1.003	0.264	0.057
0.5	(-1.00, 1.00)	5 × 2M	-0.795	0.310	0.130	1.096	0.270	0.161
0.0	(-1.00, 1.00)	5 × 2M	-0.798	0.311	0.137	1.084	0.271	0.166
-0.5	(-1.00, 1.00)	5 × 2M	-0.848	0.311	0.132	1.065	0.271	0.163
0.5	(-1.00, -1.00)	5 × 2M	-0.907	0.304	0.111	-0.995	0.261	0.058
0.0	(-1.00, -1.00)	5 × 2M	-0.943	0.310	0.099	-0.978	0.265	0.067
-0.5	(-1.00, -1.00)	5 × 2M	-0.955	0.304	0.100	-1.036	0.261	0.061
			Results for τ [fs]			Results for offset [fs]		
			⟨Result⟩	⟨Error⟩	RMS/$\sqrt{n-1}$	⟨Result⟩	⟨Error⟩	RMS/$\sqrt{n-1}$
0.5	(1.00, 1.00)	5 × 2M	410.582	1.316	0.923	4.110	0.944	0.521
0.0	(1.00, 1.00)	5 × 2M	409.093	1.313	0.945	2.596	1.037	0.567
-0.5	(1.00, 1.00)	5 × 2M	407.486	1.314	0.930	1.164	1.083	0.575
0.5	(1.00, -1.00)	5 × 2M	411.497	1.227	0.522	3.932	1.021	0.311
0.0	(1.00, -1.00)	5 × 2M	409.923	1.215	0.723	2.554	1.022	0.286
-0.5	(1.00, -1.00)	5 × 2M	408.424	1.225	0.803	1.155	1.025	0.299
0.5	(-1.00, 1.00)	5 × 2M	409.859	1.218	1.062	4.683	1.017	0.472
0.0	(-1.00, 1.00)	5 × 2M	408.541	1.210	1.110	3.197	1.021	0.500
-0.5	(-1.00, 1.00)	5 × 2M	407.190	1.211	1.179	1.747	1.025	0.541
0.5	(-1.00, -1.00)	5 × 2M	412.165	1.175	0.310	2.810	0.954	0.266
0.0	(-1.00, -1.00)	5 × 2M	411.226	1.221	0.360	1.861	1.020	0.405
-0.5	(-1.00, -1.00)	5 × 2M	410.671	1.182	0.616	0.762	3.036	0.495

Table 7.15: Results of fitting to full Monte Carlo samples with the acceptable D^0 mass window changed.

D^0 window move [MeV/c^2]	True (x, y) [%]	Sample	Results for x [%]			Results for y [%]		
			⟨Result⟩	⟨Error⟩	RMS/$\sqrt{n-1}$	⟨Result⟩	⟨Error⟩	RMS/$\sqrt{n-1}$
0.5	(1.00, 1.00)	5 × 2M	1.088	0.324	0.149	0.877	0.284	0.123
0.0	(1.00, 1.00)	5 × 2M	1.034	0.325	0.155	0.892	0.285	0.128
-0.5	(1.00, 1.00)	5 × 2M	1.002	0.330	0.155	0.897	0.290	0.139
0.5	(1.00, -1.00)	5 × 2M	1.102	0.308	0.166	-1.056	0.260	0.064
0.0	(1.00, -1.00)	5 × 2M	1.030	0.308	0.141	-1.063	0.260	0.069
-0.5	(1.00, -1.00)	4 × 2M	1.063	0.308	0.169	-1.031	0.260	0.096
0.5	(-1.00, 1.00)	5 × 2M	-0.833	0.306	0.135	0.956	0.265	0.150
0.0	(-1.00, 1.00)	5 × 2M	-0.874	0.306	0.143	0.973	0.266	0.149
-0.5	(-1.00, 1.00)	5 × 2M	-0.915	0.306	0.140	0.957	0.265	0.141
0.5	(-1.00, -1.00)	5 × 2M	-0.908	0.305	0.110	-1.089	0.261	0.068
0.0	(-1.00, -1.00)	5 × 2M	-0.936	0.305	0.095	-1.071	0.261	0.064
-0.5	(-1.00, -1.00)	5 × 2M	-0.955	0.305	0.100	-1.084	0.261	0.057
			Results for τ [fs]			Results for offset [fs]		
			⟨Result⟩	⟨Error⟩	RMS/$\sqrt{n-1}$	⟨Result⟩	⟨Error⟩	RMS/$\sqrt{n-1}$
0.5	(1.00, 1.00)	5 × 2M	409.706	1.270	0.895	0.808	0.369	0.156
0.0	(1.00, 1.00)	5 × 2M	409.539	1.273	0.889	1.836	1.042	0.499
-0.5	(1.00, 1.00)	5 × 2M	409.224	1.272	0.859	2.502	1.034	0.318
0.5	(1.00, -1.00)	5 × 2M	410.659	1.178	0.738	1.490	0.953	0.171
0.0	(1.00, -1.00)	5 × 2M	410.508	1.180	0.892	2.082	0.956	0.292
-0.5	(1.00, -1.00)	4 × 2M	410.567	1.172	1.135	2.877	0.947	0.186
0.5	(-1.00, 1.00)	5 × 2M	409.232	1.168	1.167	2.094	0.952	0.286
0.0	(-1.00, 1.00)	5 × 2M	409.199	1.165	1.175	2.636	0.958	0.424
-0.5	(-1.00, 1.00)	5 × 2M	409.107	1.168	1.248	3.228	0.952	0.330
0.5	(-1.00, -1.00)	5 × 2M	411.525	1.178	0.443	1.301	0.952	0.185
0.0	(-1.00, -1.00)	5 × 2M	411.737	1.174	0.476	1.736	0.939	0.296
-0.5	(-1.00, -1.00)	5 × 2M	411.700	1.179	0.467	2.359	0.955	0.195

Table 7.16: Results of fitting to full Monte Carlo samples with the acceptable D^0 mass window changed, with a mass constraint in the kinematic fit.

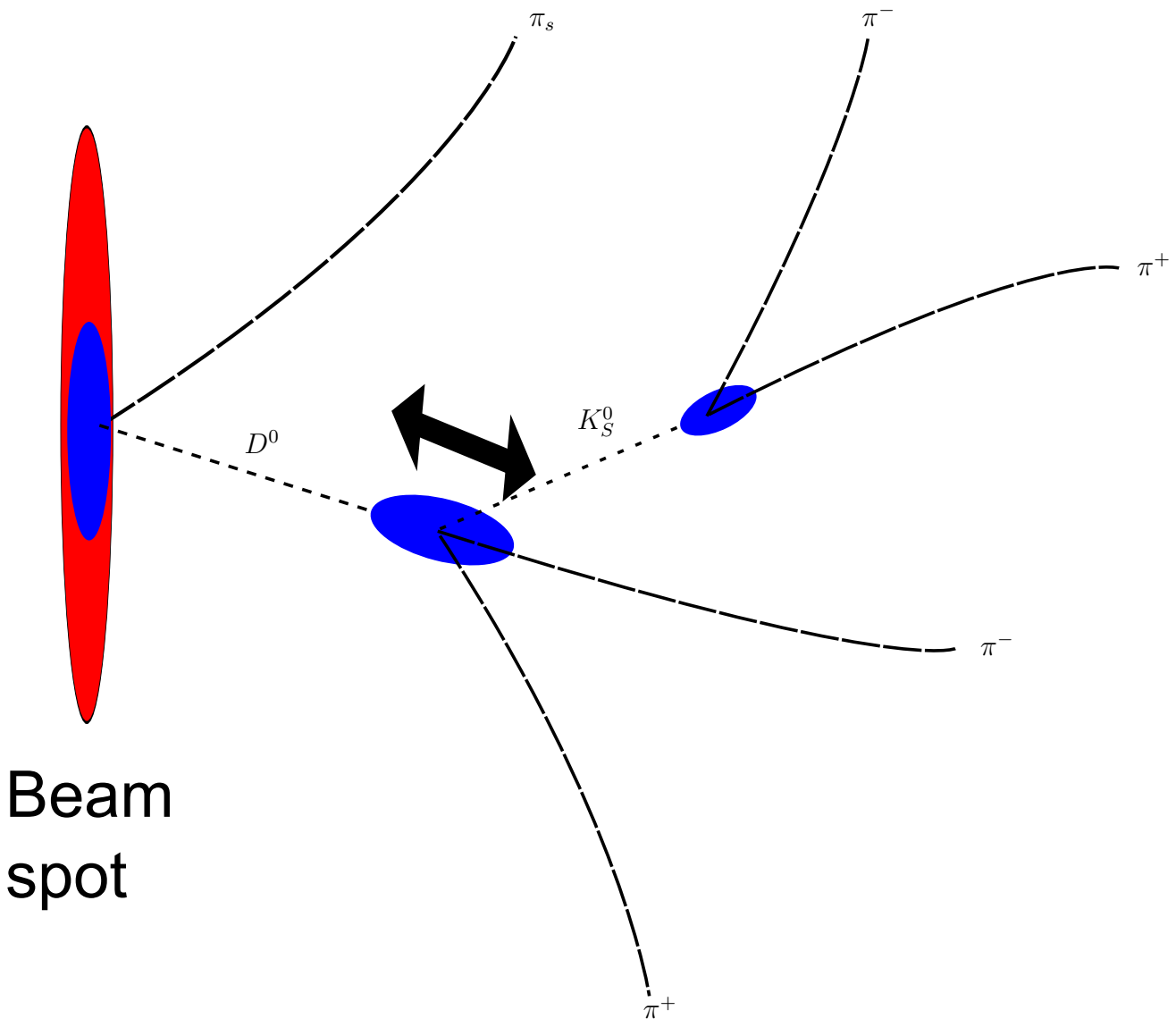

Figure 7.7: D^* decay-tree reconstruction. The D^* decay vertex is effectively fixed to the beam spot; when the D^0 decay vertex is moved along the D^0 momentum, the angle between its daughters' momenta (which determines the reconstructed mass) and the flight length (which determines the decay time) both change.

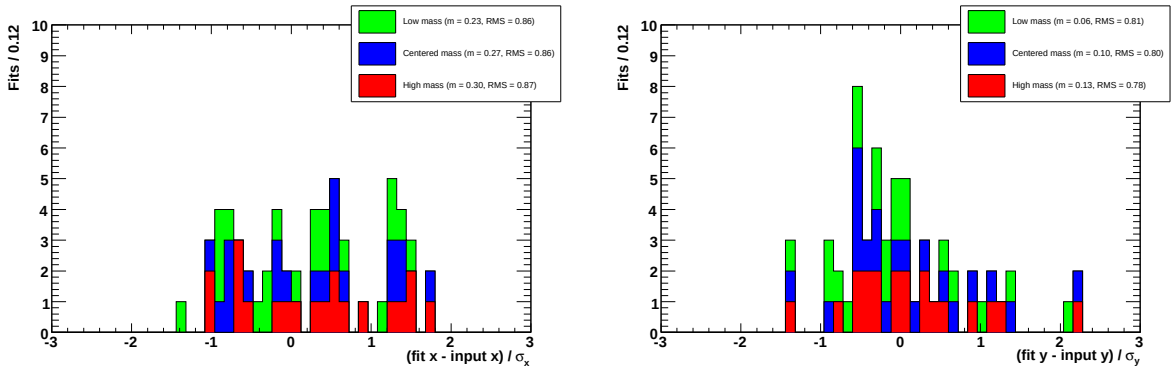

Figure 7.8: Pull distributions for fits with mass windows moved down (green), unchanged (blue) or moved up (red), for x (left) and y (right).

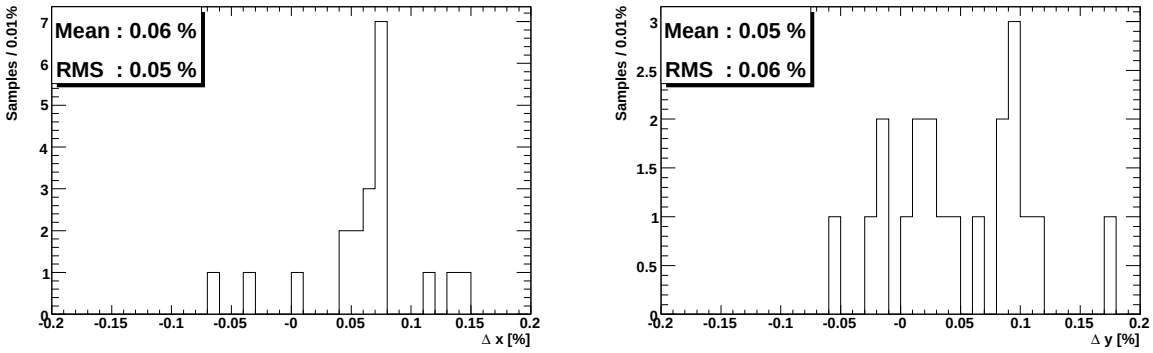

Figure 7.9: Difference between the fit results for 'up-moved' and 'down-moved' samples. The left-hand plot shows the 'up-minus-down' differences for x, the right-hand plot for$y$.

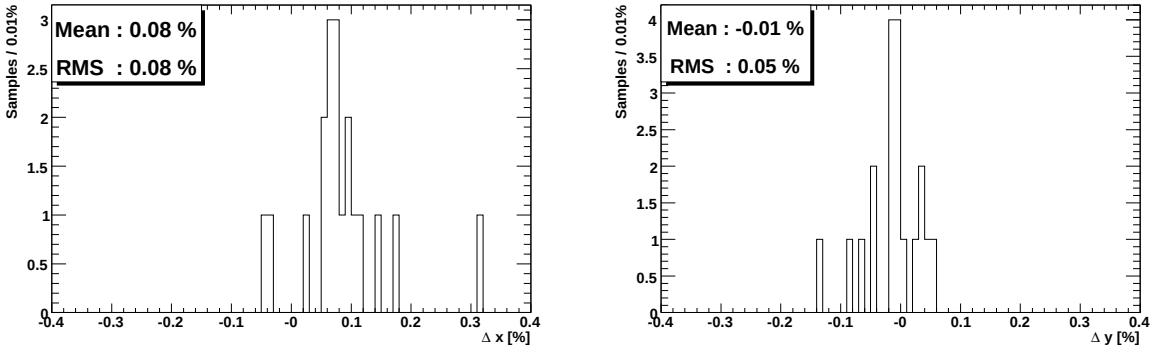

Figure 7.10: Difference between the fit results for 'up-moved' and 'down-moved' samples, using a mass constraint on the kinematic fit. The left-hand plot shows the 'up-minus-down' differences for x, the right-hand plot for$y$.

True (x, y) [%]	Sample 1	Sample 2	Sample 3	Sample 4	Sample 5
(1.00, 1.00)	0.001	0.007	-0.037	-0.074	-0.027
(1.00, -1.00)	-0.009	-0.103	-0.084	-0.047	0.046
(-1.00, 1.00)	0.038	0.006	-0.058	0.027	-0.025
(-1.00, -1.00)	-0.048	-0.063	-0.064	-0.014	0.007

Table 7.17: Change in fit result (in 10^{-2}) for x for individual samples, with the acceptable D^0 mass window moved by 0.5 MeV/c^2, with respect to the fit of the same sample with the default mass window.

True (x, y) [%]	Sample 1	Sample 2	Sample 3	Sample 4	Sample 5
(1.00, 1.00)	-0.004	0.007	-0.036	0.043	-0.063
(1.00, -1.00)	0.001	-0.155	-0.082	-0.040	-0.003
(-1.00, 1.00)	0.000	-0.006	-0.035	-0.020	0.004
(-1.00, -1.00)	0.019	-0.024	-0.001	-0.046	0.138

Table 7.18: Change in fit result (in 10^{-2}) for y for individual samples, with the acceptable D^0 mass window moved by 0.5 MeV/c^2, with respect to the fit of the same sample with the default mass window.

True (x, y) [%]	Sample 1	Sample 2	Sample 3	Sample 4	Sample 5
(1.00, 1.00)	0.074	0.053	0.036	0.002	0.038
(1.00, -1.00)	0.140	-0.032	0.049	0.032	0.005
(-1.00, 1.00)	0.103	0.059	0.002	0.033	0.052
(-1.00, -1.00)	0.027	-0.015	0.054	0.048	-0.055

Table 7.19: Change in fit result (in 10^{-2}) for x for individual samples, with the acceptable D^0 mass window moved by -0.5 MeV/c^2, with respect to the fit of the same sample with the default mass window.

True (x, y) [%]	Sample 1	Sample 2	Sample 3	Sample 4	Sample 5
(1.00, 1.00)	0.017	-0.014	0.070	-0.014	0.025
(1.00, -1.00)	0.048	0.026	0.014	0.051	0.058
(-1.00, 1.00)	0.033	0.009	0.054	-0.008	0.009
(-1.00, -1.00)	0.008	0.067	0.026	0.065	0.125

Table 7.20: Change in fit result (in 10^{-2}) for y for individual samples, with the acceptable D^0 mass window moved by -0.5 MeV/c^2, with respect to the fit of the same sample with the default mass window.

7.6 Uncertainty from the amplitude model

The isobar model described in Chapter 5 gives a reasonable description of the Dalitz plot, but it is not the only possible model. We also consider the following models:

True (x, y) [%]	Sample 1	Sample 2	Sample 3	Sample 4	Sample 5
(1.00, 1.00)	-0.026	-0.033	-0.083	-0.089	-0.038
(1.00, -1.00)	-0.035	-0.109	-0.147	-0.060	-0.005
(-1.00, 1.00)	0.003	-0.035	-0.099	-0.018	-0.059
(-1.00, -1.00)	-0.070	-0.077	-0.028	-0.017	0.048

Table 7.21: Change in fit result (in 10^{-2}) for x for individual samples, with the acceptable D^0 mass window moved by 0.5 MeV/c^2, with respect to the fit of the same sample with the default mass window, using the mass-constrained kinematic fit.

True (x, y) [%]	Sample 1	Sample 2	Sample 3	Sample 4	Sample 5
(1.00, 1.00)	0.010	0.035	0.008	0.039	-0.013
(1.00, -1.00)	0.012	0.014	-0.068	-0.021	0.025
(-1.00, 1.00)	0.015	0.027	0.002	0.022	0.017
(-1.00, -1.00)	0.060	0.002	0.011	-0.027	0.040

Table 7.22: Change in fit result (in 10^{-2}) for y for individual samples, with the acceptable D^0 mass window moved by 0.5 MeV/c^2, with respect to the fit of the same sample with the default mass window, using the mass-constrained kinematic fit.

True (x, y) [%]	Sample 1	Sample 2	Sample 3	Sample 4	Sample 5
(1.00, 1.00)	0.047	0.059	0.059	-0.033	0.029
(1.00, -1.00)		-0.041	0.031	0.258	-0.036
(-1.00, 1.00)	0.089	0.042	0.009	0.003	0.060
(-1.00, -1.00)	0.026	-0.008	0.045	0.033	-0.002

Table 7.23: Change in fit result (in 10^{-2}) for x for individual samples, with the acceptable D^0 mass window moved by -0.5 MeV/c^2, with respect to the fit of the same sample with the default mass window, using the mass-constrained kinematic fit.

True (x, y) [%]	Sample 1	Sample 2	Sample 3	Sample 4	Sample 5
(1.00, 1.00)	0.008	-0.010	0.050	-0.045	-0.027
(1.00, -1.00)		-0.005	-0.032	-0.159	0.022
(-1.00, 1.00)	0.043	0.009	0.037	-0.024	0.011
(-1.00, -1.00)	-0.007	-0.006	0.020	0.030	0.028

Table 7.24: Change in fit result (in 10^{-2}) for y for individual samples, with the acceptable D^0 mass window moved by -0.5 MeV/c^2, with respect to the fit of the same sample with the default mass window, using the mass-constrained kinematic fit.

- An isobar model, but with only the first σ resonance, and inserting a κ resonance centered at 500 MeV/c^2 and with width 400 MeV/c^2 in each $K\pi$ S-wave.

- The $\pi\pi$ S-wave is described by the K-matrix model described in Section 5.3 instead of the isobar model.
- Using the LASS parametrisation of the $K\pi$ S-wave discussed in Section 5.4 in place of the pure isobar model.
- Both the $\pi\pi$ and $K\pi$ S-waves are replaced, by the K-matrix and LASS models respectively.

Table 7.25 shows the change in mixing parameters from using different resonance models. The maximum deviation in each parameter is taken as the model systematic uncertainty, giving 0.087% for x and 0.046% for y.

Fit	Δx [%]	Δy [%]
BW-only fit	0.000	0.000
κ resonance	-0.021	0.046
Kmatrix+LASS fit	-0.087	0.044
K-matrix only	-0.044	-0.024
LASS only	-0.042	0.046

Table 7.25: Change in fit result for data when different resonance models are used.

To ensure that the models reflect a real uncertainty in the best way of describing the Dalitz plot, we calculate the χ^2 per degree of freedom using an adaptive binning. If we found that any model was significantly worse than the others, we would not use it in calculating a systematic uncertainty, on the grounds that you cannot learn anything about your real model uncertainty by using a model you know to be bad. To take a trivial example, a flat amplitude model would give a different set of mixing parameters and a bad goodness-of-fit, and would not tell you about the real model sensitivity.

The adaptive-binning algorithm is as follows. Begin by considering the entire Dalitz plot as a single bin, and count the number of events in that bin. Now split the bin into four equal parts (one vertical split-in-half, one horizontal) if the following are true:

- No bin internal to the kinematic boundary would have less than 36 events in it after the split.

- No bin has a width less than $1/2^n$ of the entire Dalitz-plot width - in other words, we haven't already split n times to produce the bin. We refer to the number 2^n as the fineness of the underlying grid, since it is the maximum number of bins we could get in each dimension. For example, if the limit n is set to 9, we would get at most a 512×512 grid across the Dalitz plot.

This procedure is followed recursively (ignoring bins outside the boundary) until no more splits are possible, and we then calculate $\chi^2 = \sum_i (P_i - O_i)^2/E_i^2$, where P_i is the predicted number of events in the bin i, O_i is the observed number, E_i is the error in the prediction (taken as its square root) and the sum goes over bins internal to the kinematic limit. Note that in checking whether new bins would have less than 36 events, we could use either the PDF prediction or the data; we chose the prediction to avoid fluctuations in low-population regions; this the number of degrees of freedom varies slightly (for the same grid fineness) between different models.

We find that this procedure gives a χ^2 per degree of freedom which depends on the fineness of the grid, as shown in Table 7.26. It is worth noting that the $\Delta\chi^2$, the *difference* (not the ratio) between the χ^2 and the degrees of freedom, remains roughly constant. Since the ratio approaches a constant as we increase the fineness to 4096, we stop at that point and take those numbers as the goodness-of-fit; since there are no large differences, we take the pure-BW fit as our nominal result. (We do not use the κ model in order to make our result more easily comparable to previous *BABAR* analyses.) and use all the other models for systematics. Figure 7.11 shows the distribution of χ across the Dalitz plot, with grid fineness 4096, for the pure-BW model.

7.7 Mistag effects

The category-2 background, where a correctly reconstructed D^0 is matched with a track that did not come from a D^* decay, is further divided into 'lucky' and 'unlucky'. In the lucky events, the random track has the charge which correctly tags the D^0; in unlucky events, a

Grid fineness	Nominal fit	BW with κ	LASS
128	4497.2 / 1297 = 3.47	3615.1 / 1299 = 2.78	6210.6 / 1295 = 4.80
256	8187.1 / 4924 = 1.66	7314.3 / 4935 = 1.48	10277.2 / 4948 = 2.08
512	17360.4 / 14090 = 1.23	16485.4 / 14097 = 1.17	19329.1 / 13904 = 1.39
1024	26199.5 / 22810 = 1.15	25336.9 / 22833 = 1.11	28220.6 / 22642 = 1.25
2048	33146.7 / 29585 = 1.12	32220.4 / 29591 = 1.09	35174.6 / 29418 = 1.20
4096	33378.1 / 29937 = 1.11	32531.7 / 30035 = 1.08	35397.5 / 29717 = 1.19
Grid fineness	K-matrix	K-matrix and LASS	
128	4600.4 / 1273 = 3.61	4417.6 / 1282 = 3.45	
256	8410.1 / 4891 = 1.72	8214.9 / 4904 = 1.68	
512	17467.0 / 13960 = 1.25	16969.5 / 13698 = 1.24	
1024	26275.6 / 22636 = 1.16	25790.3 / 22438 = 1.15	
2048	33219.7 / 29421 = 1.13	32672.1 / 29214 = 1.12	
4096	33453.7 / 29686 = 1.13	32975.2 / 29524 = 1.12	

Table 7.26: χ^2 per degree of freedom for different fit models with different grid finenesses.

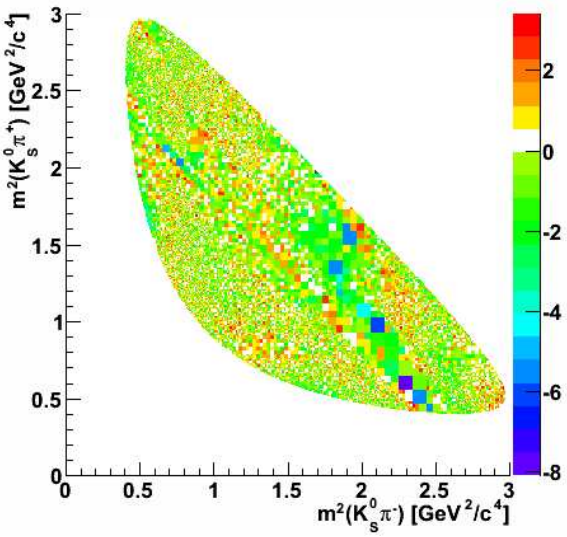

Figure 7.11: Distribution of χ across the Dalitz plot, for the pure-BW (nominal) model with the grid fineness set to 4096.

D^0 is tagged as $\overline{D}^0$ or vice-versa. A Dalitz plot showing only these events is reversed with respect to the correctly tagged events; for example, the strong K^{*-} band fills in the trough of the K^{*+}, diluting the sensitivity to mixing. The percentage of unlucky events, also called the mistag fraction, is estimated from Monte Carlo. Naively one would expect it to be 50%, but there are charge asymmetries in the detector response and in the production physics. The slow pion candidate, whether or not it is correctly reconstructed, is more likely to come from the same c-quark jet that produced the D^0 candidate; tracks from the other c quark are less likely to have a momentum and direction that allows a plausible D^* candidate. Since the c quark is positively charged, a randomly selected track from its decay has a slightly greater probability of being positively charged, that is, tagging the D^* correctly. In Monte Carlo, we find that the fraction of misreconstructed D^* candidates which are correctly tagged, the 'lucky fraction', is 54%. Table 7.27 shows the effect of varying the assumed lucky fraction. Notice that this study is done on data, not Monte Carlo. There is a tiny dependence of each mixing parameter on the lucky fraction, about half of one-hundredth of a percent for a change in the lucky fraction from 45% to 60%.

In addition, Table 7.28 shows the results of fits to toy Monte Carlo where the fit PDF assumes no mistagging, while the toy sample has some unlucky events. Note that this table shows a much more substantial effect of changing the lucky fraction; this can be understood in terms of the size of the category-2 background. In data, category 2 is on the order of a few thousand events, and if the true mistag fraction is, say, 50%, and we call it 55%, this is equivalent to mis-estimating the number of unlucky events by a few hundred. Since the data sample is on the order of half a million events, realistic uncertainties in the mistag fraction are on the order of at most a per-*mille* of the sample. In the toy tests, however, we deliberately mis-estimate the number of unlucky events by several *percent* of the sample - creating an effect an order of magnitude larger. The effect is roughly linear; if we extrapolate down from the 0.1% change in mixing parameters we get at 0.5% unlucky events, to see what we would get at the half-a-permille level that is the most we expect in data, we find 0.01% - in good agreement with the data tests above. We therefore assign a suitably minor systematic of

Lucky fraction [%]	Δx [%]	Δy [%]
45.0	0.0033	0.0032
47.5	0.0024	0.0024
50.0	0.0012	0.0014
52.5	0.0003	0.0005
54.0	0.0000	0.0000
55.0	-0.0003	-0.0003
57.5	-0.0015	-0.0014
60.0	-0.0021	-0.0021

Table 7.27: Change in reported mixing parameters, relative to the fit using the nominal value of 54%, when the assumed lucky fraction is changed.

Unlucky fraction	Fit x [%]	Δx [%]	Fit y [%]	Δy [%]
0.0%	0.836	0.000	0.971	0.000
0.5%	0.714	-0.122	0.849	-0.122
1.0%	0.729	-0.107	0.820	-0.151
1.5%	0.653	-0.183	0.745	-0.226
2.5%	0.531	-0.305	0.656	-0.315
5.0%	0.291	-0.545	0.600	-0.371

Table 7.28: Results from toy Monte Carlo with small mistag fractions; the fit PDF used here assumes no mistagging.

0.01% from this effect.

7.8 Note on $K^*(1410)$

In Belle's similar analysis (Ref. [5]), the resonances $K^{*\pm}(1410)$ were included in the isobar model. As a comparison and cross-check, we made a fit to our data including these resonances; as shown in Table 7.29, we find them to be smaller than in the Belle analysis. The change in mixing parameters relative to the nominal fit is small, 0.013% for x and -0.002% for y. Note that Belle reported the amplitudes in terms of a magnitude and a phase in degrees; for ease of comparison we have converted this to a real and imaginary part. Our result is significantly different from Belle's; in particular, our 'wrong-sign' resonance does not have half the magnitude of the 'right-sign', but is much smaller. Since such wrong-sign decays are doubly-Cabibbo-suppressed, while the right-sign ones are Cabibbo-favoured, our

	Belle		This analysis	
	Real	Imaginary	Real	Imaginary
$K^{*-}(1410)$	0.61 ± 0.03	-0.23 ± 0.04	-0.33 ± 0.02	-0.08 ± 0.02
$K^{*+}(1410)$	-0.32 ± 0.02	-0.07 ± 0.02	0.06 ± 0.02	-0.02 ± 0.02

Table 7.29: Amplitudes of the $K^{*\pm}(1410)$ resonances, relative to $\rho = 1$.

smaller ratio (a factor 5 in amplitude, 25 in rate) is closer to the naive expectation. Note that including the $K^*(1410)$ rsonances makes the goodness-of-fit worse; for grid fineness of 256, the χ^2 per degree of freedom is 2.28, significantly worse than any other model.

7.9 Fit variations

In addition to the big effects considered so far, there are a number of small changes that can be made to the fit, which may have a systematic effect on the mixing parameters. The effects to be considered are:

- Varying the background and signal yields within their uncertainties. The results are shown in Table 7.30 and added in quadrature to give uncertainties of 0.010% for x and 0.007% for y. Notice that this procedure probably overestimates this uncertainty, since the change from decreasing the yield of each category is very close to the negative of the change from increasing the yield; however, since the numbers are small compared to other systematics, a more sophisticated process is not required.

- Background amplitude model. The Dalitz-plot distribution of the category-3 and category-4 backgrounds is described by a histogram taken from Monte Carlo events; we vary this by instead using events from the data sidebands, specifically by taking events where $|m_{D^0} - \overline{m}| > 45$ MeV/c^2, where $\overline{m}$ is the average D^0 mass found by the step-1 fit, 1.86411 GeV/c^2.

- Background time model. The category-3 and category-4 distribution in decay time is fixed (to values found from Monte Carlo) in the step-2 fit, as described in 6.4. The PDF is a sum of two Gaussians plus a small linear component; we vary the means and

widths of the Gaussians and the fraction of the second one, as shown in Table 7.31, and add the deviations from the nominal fit in quadrature to give a systematic uncertainty of 0.024% for x and 0.060% for y. As with the yields, this is probably an overestimate, but since the values are relatively small this does not matter.

- Normalisation of the Dalitz-plot PDF. In the canonical fit we do this by integrating over a grid of 400×400 points; for this test we increase this to 1000×1000 points.

- Efficiency. Instead of the histogram used in the canonical fit, we fit a 2-dimensional polynomial to the efficiency distribution and use that as the estimate of efficiency.

- Error on the proper time. Here there are three variations:

  - Split the Dalitz plot into slices, and have a separate σ_t distribution for each slice.
  - Model the σ_t distributions with a parametrised PDF instead of histograms.
  - Change the maximum allowed σ_t from 1 ps to 0.8 ps.

- K_sK_s background: An additional background component is added to the fit to model the decay $D^0 \to K_sK_s$. This 'category-5' PDF consists of a histogram (created from Monte Carlo) for the Dalitz plot, and a simple exponential (using the same lifetime τ as the signal) for the time. The resolution function for the lifetime is shared with the signal.

- Consider the meson radius, R in Eqn. 2.16, to be 1.0 and 2.0 c/GeV instead of the nominal 1.5 c/GeV; the systematic is the full difference between the high- and low-radius fits.

All these changes are done, one by one, to the fit to data, and the systematic uncertainty is taken as the difference between the mixing-parameter values for the changed fit and the nominal fit. Table 7.32 shows the changes in x and y, which are taken as systematic uncertainties to be added in quadrature. The dominant effects are misalignment and the amplitude model.

Yield change	Δx [%]	Δy [%]
Cat 1 increase	0.002	0.001
Cat 1 decrease	-0.002	-0.001
Cat 2 increase	0.003	0.003
Cat 2 decrease	-0.003	-0.003
Cat 3 increase	-0.001	0.000
Cat 3 decrease	0.000	0.000
Cat 4 increase	-0.006	-0.004
Cat 4 decrease	0.006	0.004
Total	0.010	0.007

Table 7.30: Changes in mixing parameters when increasing or decreasing the category yields by one reported sigma.

Parameter change	Δx [%]	Δy [%]
$\overline{t_{b1}}$ increase	0.004	0.010
$\overline{t_{b1}}$ decrease	-0.004	-0.009
σ_{b1} increase	0.008	0.018
σ_{b1} decrease	-0.011	-0.022
$\overline{t_{b2}}$ increase	0.009	0.022
$\overline{t_{b2}}$ decrease	-0.008	-0.019
σ_{b2} increase	0.008	0.024
σ_{b2} decrease	-0.008	-0.024
f_{b1} increase	-0.006	-0.014
f_{b1} decrease	0.008	0.020
Total	0.024	0.060

Table 7.31: Changes in mixing parameters when varying the parameters of the background time PDF, Eqn. 6.19.

Fit variation	Δx [%]	Δy [%]
Category yields	0.010	0.007
Background time model	0.024	0.060
Background amplitude model	0.011	0.003
Normalisation	-2×10^{-4}	-3×10^{-4}
Polynomial efficiency (*)	0.037	0.018
Sliced σ_t	0.082	0.048
Parametrised σ_t	-5×10^{-5}	-2×10^{-5}
K_sK_s component	-0.034	-0.018
Meson radius	0.025	0.008
Total	0.103	0.081

Table 7.32: Mixing-parameter variations from varying the fit. Numbers marked with an asterisk were provided by Jordi Garra Tico.

The total systematic uncertainty from fit variations is found by adding all the variations in quadrature, giving 0.100% for x and 0.081% for y. The correlation between the x and y changes is 0.78.

7.10 Sample variations

In the previous section we considered variations in the fit model; now we consider variations on the sample selection. Changing the sample is expected to produce some variation in the fit result by plain statistical fluctuation, and it is therefore not necessary to take the entire change in result as a systematic uncertainty. Instead, for each sample, we look at the quadratic change in the reported fit error, $\Delta\sigma = sqrt\sigma_1^2 - \sigma_2^2$ where the subscript 1 refers to the fit with the larger error, and subtract this from the change in fit result. If this corrected change is larger than zero, we assign it as a systematic.

The changes we make in the sample are as follows:

- Varying the D^0 decay time selection. Instead of taking the range $t \in [-6, 6]$ ps, we take $t \in [-5, 5]$ ps.

- Size of the signal box. As a test of our understanding of the background, we increase the signal box to be 22 MeV/c^2 in m_{D^0} and 1.4 MeV/c^2 in Δm, considerably increasing

the relative amount of background.

- Change the maximum allowed σ_t from 1 ps to 0.85 ps.

Table 7.33 shows the results; the effects are all small compared to the misalignment systematic.

Fit variation	Δx [%]	$\Delta\sigma_x$ [%]	Adjusted Δx [%]	Δy [%]	$\Delta\sigma_y$ [%]	Adjusted Δy [%]
Decay-time selection	0.009	0.011	0.000	0.015	0.008	0.007
Signal box	0.105	0.054	0.051	0.062	0.063	0.000
Changed σ_t range	0.013	0.006	0.007	0.001	0.001	0.000
Total	0.051			0.007		

Table 7.33: Mixing-parameter variations from varying the sample.

7.11 Systematics summary

Table 7.34 summarises the sources of systematic uncertainty. The dominant contributions are from detector misalignment and the resonance model.

Source	x uncertainty [%]	y uncertainty [%]
Misalignment	0.100	0.100
Resonance model	0.087	0.046
D^0 mass	0.025	0.025
Mistagging	0.010	0.010
Fit bias	0.100	0.100
Fit variations	0.103	0.081
Sample variations	0.051	0.007
Total	0.204	0.172

Table 7.34: Summary of the systematic uncertainties.

Chapter 8

Conclusion

This chapter summarises the results of the analysis.

8.1 Systematic errors

We have considered systematic errors due to several possible causes, summarised in Table 8.1. Adding the contributions in quadrature, we find 0.20% for x and 0.17% for y.

Source	Described in Section	Effect on x [%]	Effect on y [%]
Sample size	7.2	0	0
Radiative decays	7.2	0	0
Fit bias	7.3	0.100	0.100
Misalignment	7.4	0.100	0.100
D^0 mass	7.5	0.025	0.025
Resonance model	7.6	0.087	0.046
Mistag effects	7.7	0.010	0.010
Fit variations	7.9	0.103	0.081
Sample variations	7.10	0.051	0.007
Total	-	0.204	0.172

Table 8.1: Sources of systematic uncertainty for the mixing parameters.

8.2 Results

The final values for the mixing parameters are

$$\begin{aligned} x &= (0.43 \pm 0.25 \pm 0.20)\% \\ y &= (0.70 \pm 0.22 \pm 0.17)\%. \end{aligned}$$

Note that these numbers differ from those found by our cross-checking colleagues in their separate fit (and reported in our joint journal article, Ref [31]), namely $x = (0.26 \pm 0.24)\%$ and $y = (0.60 \pm 0.21)\%$. The difference is less than the statistical uncertainty.

For comparison, some previous results are shown in Table 8.2; there is a review in [32]. Taking only events with a D^0 gives instead

$$\begin{aligned} x_{D^0} &= (0.49 \pm 0.36 \pm 0.20)\% \\ y_{D^0} &= (0.82 \pm 0.31 \pm 0.17)\% \end{aligned}$$

and conversely, using only $\overline{D}^0$ events gives

$$\begin{aligned} x_{\overline{D}^0} &= (0.46 \pm 0.35 \pm 0.20)\% \\ y_{\overline{D}^0} &= (0.55 \pm 0.31 \pm 0.17)\%. \end{aligned}$$

Since the numbers are well within the uncertainties, we find no evidence of *CP* violation.

Figure 8.1 shows confidence-level contours in $x - y$ space; the 68%-confidence contour (that is, the inmost ellipse, covering the area where the change in $-2 \log \mathcal{L}$ is less than 2.3) is referred to as the '1-sigma' contour, since its coverage is equivalent to a range of 1 sigma around the central value in one dimension. Figure 8.2 combines several *BABAR* mixing results to improve the contours; in particular, it takes this result (in green), the 2009 measurement of y_{CP} using $D^0 \to K^+K^-$ and $D^0 \to \pi^+\pi^-$ (Ref. [33]) (in red), and two measurements of rotated mixing parameters using $D^0 \to K^+\pi^-$ (Ref. [6], in magenta) and $D^0 \to K^+\pi^-\pi^0$

Experiment	Reference	Channel	Result [%]
E791 1998	[35]	$D^0 \to K^+K^-$	$y_{CP} = 0.8 \pm 2.9 \pm 1.0$
FOCUS 2000	[36]	$D^0 \to K^+K^-$	$y_{CP} = 3.4 \pm 1.4 \pm 0.7$
CLEO 2002	[37]	$D^0 \to K^+K^-, pi^+\pi^-$	$y_{CP} = -1.1 \pm 2.5 \pm 1.4$
BABAR 2003	[38]	$D^0 \to K^+K^-, pi^+\pi^-$	$y_{CP} = 0.8 \pm 0.4^{+0.5}_{-0.4}$
Belle 2003	[39]	$D^0 \to K^+K^-$	$y_{CP} = 1.15 \pm 0.69 \pm 0.38$
Belle 2006	[40]	$D^0 \to K^+\pi^-$	$-2.8 < y' < 2.1$, $x'^2/2 < 0.036$
Belle 2007	[5]	$D^0 \to K_s\pi\pi$	$x = 0.80 \pm 0.29^{+0.13}_{-0.16}$, $y = 0.33 \pm 0.24^{+0.10}_{-0.14}$
Belle 2007	[41]	$D^0 \to K^+K^-, \pi^+\pi^-, K^+\pi^-$	$y_{CP} = 1.31 \pm 0.32 \pm 0.25$
BABAR 2007	[6]	$D^0 \to K^+\pi^-$	$y' = 0.97 \pm 0.44 \pm 0.31$, $x'^2 = -0.022 \pm 0.030 \pm 0.021$
Belle 2008	[42]	$D^0 \to K^{(*)-}\ell^+\nu_\ell$	$R_M = (1.3 \pm 2.2 \pm 2.0) \times 10^{-2}$
BABAR 2008	[43]	$D^0 \to K^+K^-, \pi^+\pi^-, K^+\pi^-$	$y_{CP} = 1.24 \pm 0.39 \pm 0.13$
BABAR 2008	[34]	$D^0 \to K^+\pi^-\pi^0$	$x'' = (2.61^{+0.57}_{-0.68} \pm 0.39)\%$, $y'' = (-0.06^{+0.55}_{-0.64} \pm 0.34)\%$
CDF 2008	[10]	$D^0 \to K^+\pi^-$	$y' = 0.85 \pm 0.76$, $x'^2 = -0.012 \pm 0.035$
Belle 2008	[44]	$D^0 \to K^0_S K^+K^-$	$y_{CP} = 0.21 \pm 0.63$(stat.) ± 0.78(syst.) ± 0.01(model)
BABAR 2009	[33]	$D^0 \to K^+K^-, \pi^+\pi^-, K^+\pi^-$	$y_{CP} = 1.16 \pm 0.22 \pm 0.18$
Belle 2009	[45]	$D^0 \to K^0_S K^+K^-$	$y_{CP} = 0.11 \pm 0.61 \pm 0.52$

Table 8.2: Other measurements of mixing parameters. Where limits are given, they are at the 95% CL.

(Ref. [34], in cyan). These results are fitted to produce 1-sigma and 1-sigma contours in dark and light blue.

8.3 Outlook

The present direct measurement of x and y is a powerful constraint on the strong phases which cause ambiguity in other hadronic mixing analyses. Figure 8.2 is an example of this effect: The annulus from the $K\pi$ measurement of x'^2 and y', and the box from y_{CP}, collapse into a much smaller 'kidney-shaped' area when combined with the $K^0_S\pi^+\pi^-$ results. Similar analyses are underway at *BABAR* with $D^0 \to \pi^+\pi^-\pi^0$ and with $D^0 \to K^0_S K^-\pi^+$, which will refine the kidney even further. The result is compatible with the Standard Model as far as the size of the mixing effect goes; hope for New Physics must be put into both parameters

having the same sign (which requires a further theoretical understanding) or into a search for *CP* violation. Note that, since our result for x is smaller than the previous Belle result, the world-average mixing parameters are moved towards agreement with the Standard Model.

The planned SuperB experiment, with 100 times *BABAR* 's design luminosity, will further improve the contours and will also have much better sensitivity to *CP* violation. Figure 8.3 shows a guess at what a contour plot from SuperB might look like. We have taken the x and y values from the fit shown in Figure 8.2 as the central values, and made hypothetical measurements by varying each result around this central value. The width of the variation is taken as one-tenth its current error (statistical and systematic), simulating the much larger sampleB. It seems clear, with this assumption, that SuperB will give very strong constraints on the mixing parameters, strong enough even to see *CP* violation if there is any to be seen.

Future studies will attempt to measure *CP* violation in mixing, *ie* $|q/p|$ and ϕ, by allowing these quantities to vary in the fit instead of keeping them fixed to *CP*-conserving values as in this analysis. A further possibility is to measure direct *CP* violation by allowing D^0 and $\overline{D}^0$ to have different values for the resonance amplitudes.

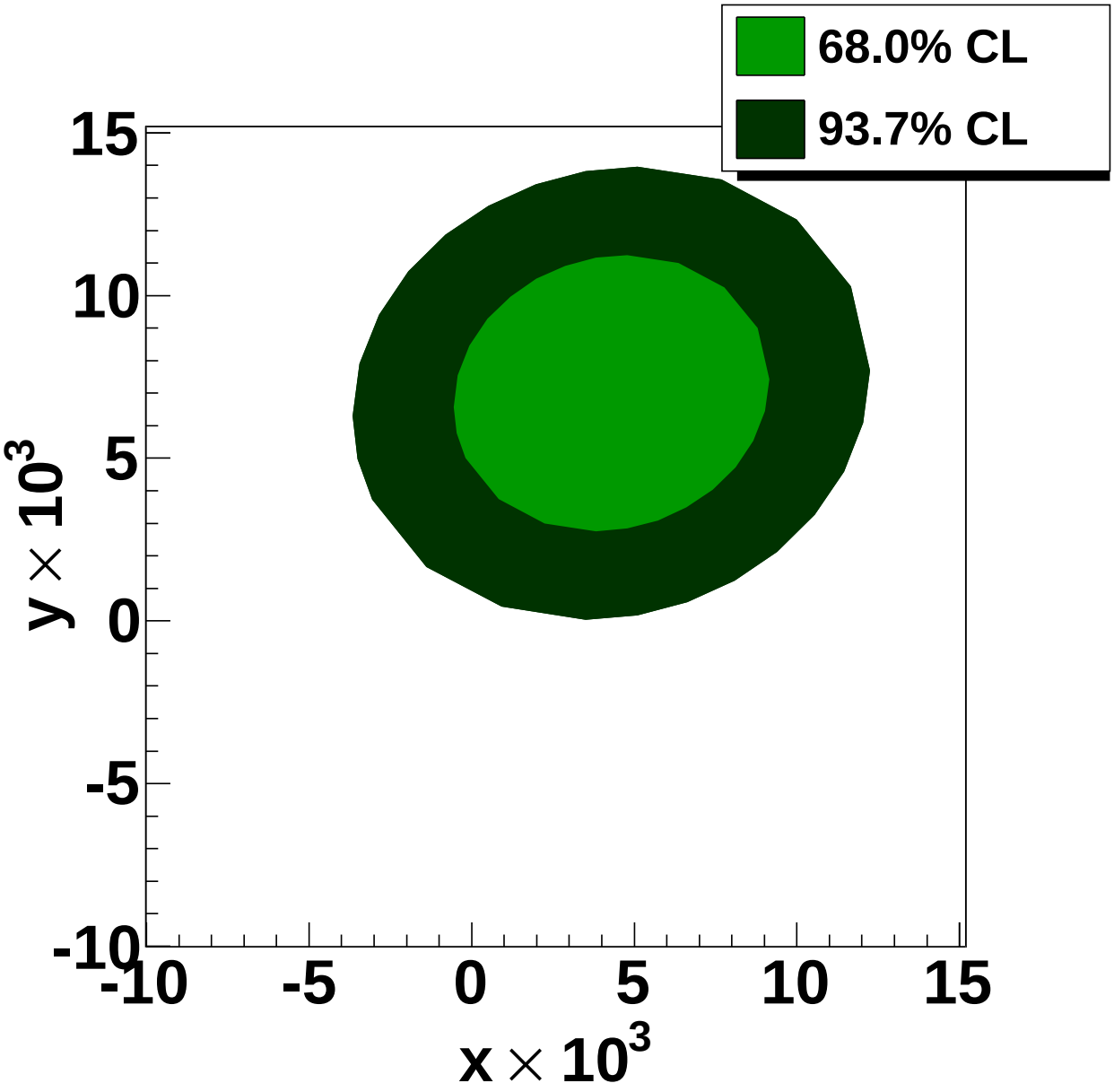

Figure 8.1: Contours enclosing 68% ('1-sigma') and 95% ('2-sigma') confidence regions for the mixing parameters.

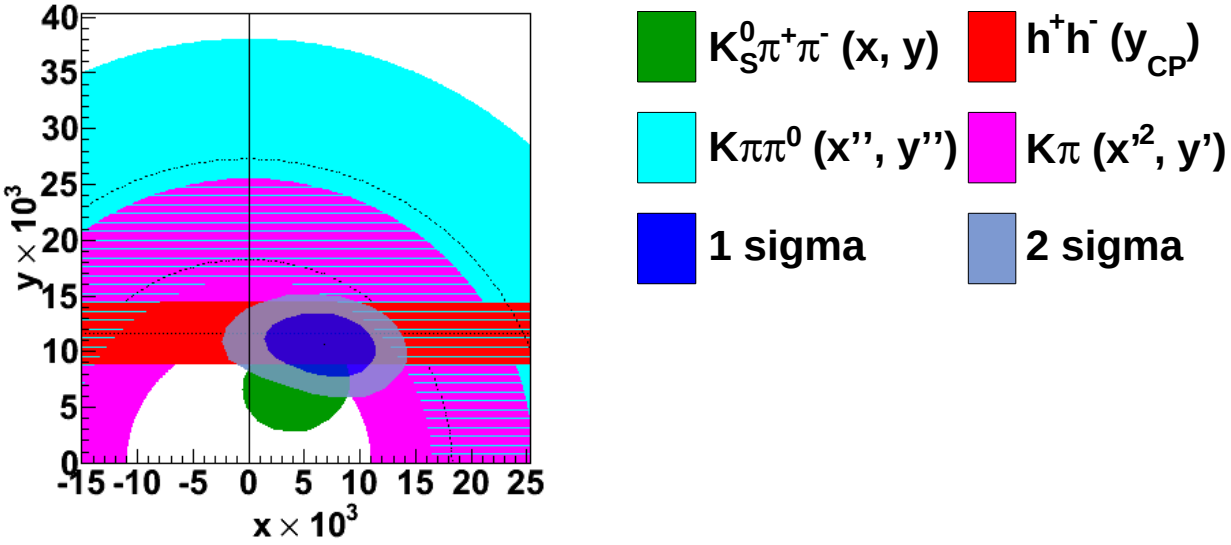

Figure 8.2: Contours enclosing 68% (dark blue) and 95% (light blue) confidence regions for the mixing parameters, averaging this study with other mixing results as described in the text.

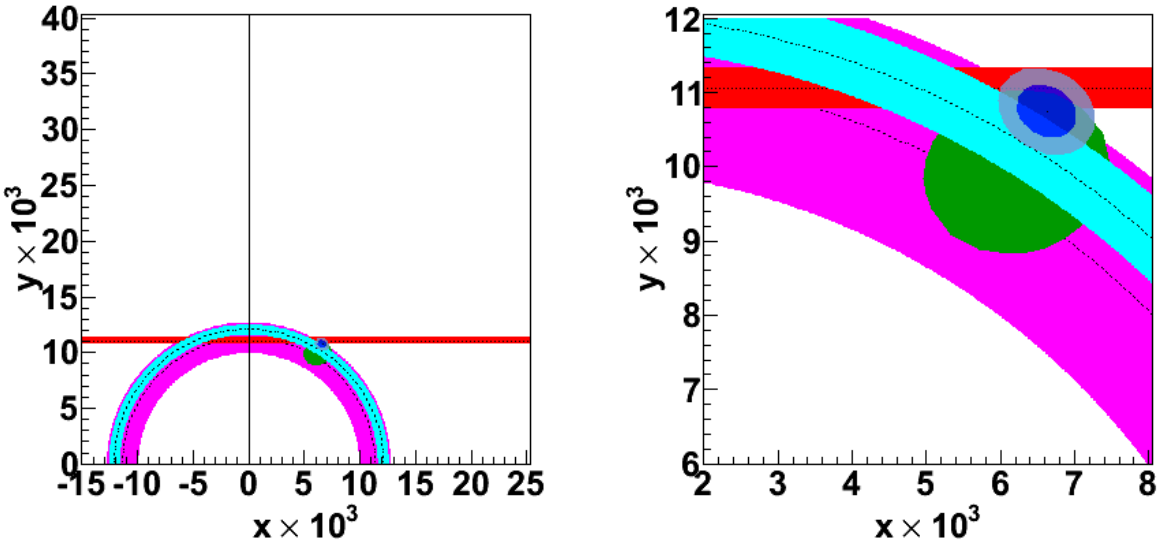

Figure 8.3: Speculative mixing contours from the proposed SuperB experiment; on the left the contours are shown on the same scale as in Figure 8.2, on the right they are shown zoomed in.

Bibliography

[1] K. Lande *et al.*, Phys. Rev. **103**, 1901 (1956).

[2] C. Albajar *et al.*, Phys. Lett. **B186**, 247 (1987).

[3] V. M. Abazov *et al.*, Phys. Rev. Lett. **97**, 021802 (2006), hep-ex/0603029.

[4] S. Bianco, F. L. Fabbri, D. Benson, and I. Bigi, A Cicerone for the physics of charm, Riv. Nuovo Cim. **26N7**, 1 (2003), hep-ex/0309021.

[5] K. Abe *et al.*, Measurement of D0-D0bar mixing in D0→Ks pi+ pi- decays, Phys. Rev. Lett. **99**, 131803 (2007), 0704.1000.

[6] B. Aubert *et al.*, Evidence for D^0 -anti-D0 Mixing, Phys. Rev. Lett. **98**, 211802 (2007), hep-ex/0703020.

[7] B. Aubert *et al.*, Measurement of D^0-$\overline{D}^0$ mixing using the ratio of lifetimes for the decays $D^0 \to K^-\pi^+$, K^-K^+, and $\pi^-\pi^+$, Submitted to Phys. Rev. D. - Rap. Comm. (2008).

[8] B. Aubert *et al.*, Search for mixing in $D^0 \to K^+\pi^-\pi^0$, Given at Lepton-Photon 2007 (2007).

[9] B. Aubert *et al.*, Search for $D^0\bar{D}^0$ mixing in the decays $D^0 \to K^+\pi^-\pi^+\pi^-$, (2006), hep-ex/0607090.

[10] T. Aaltonen *et al.*, Evidence for $D^0 - \bar{D}^0$ mixing using the CDF II Detector, Phys. Rev. Lett. **100**, 121802 (2008), 0712.1567.

[11] C. Amsler *et al.*, Review of Particle Physics, Phys. Lett **B667**, 1 (2008).

[12] P. F. Harrison and H. R. Quinn, The *BABAR* Physics Book, (1998).

[13] A. F. Falk, Y. Grossman, Z. Ligeti, and A. A. Petrov, SU(3) breaking and D0 - anti-D0 mixing, Phys. Rev. **D65**, 054034 (2002), hep-ph/0110317.

[14] D. M. Asner *et al.*, Search for D^0 - $\overline{D}^0$ Mixing in the Dalitz Plot Analysis of $D^0 \to K^0_S\pi^+\pi^-$, Phys. Rev. **D72**, 012001 (2005), hep-ex/0503045.

[15] A. Kagan, Alex's note. TODO: Find out correct way to cite., (2006).

[16] S. L. Glashow, J. Iliopoulos, and L. Maiani, Weak Interactions with Lepton-Hadron Symmetry, Phys. Rev. D **2**, 1285 (1970).

[17] M. Artuso, B. Meadows, and A. A. Petrov, Charm Meson Decays, Annu. Rev. Nucl. Part. Sci. **58**, (2008), arXiv/0802.2934.

[18] A. F. Falk *et al.*, The D0 - anti-D0 mass difference from a dispersion relation, Phys. Rev. **D69**, 114021 (2004), hep-ph/0402204.

[19] E. D. Bloom and F. J. Gilman, Scaling, duality, and the behaviour of resonances in inelastic electron-proton scattering, Phys. Rev. Lett. **25**, (1970).

[20] B. Aubert *et al.*, The BaBar detector, Nucl. Instrum. Meth. **A479**, 1 (2002), hep-ex/0105044.

[21] W. M. Y. et al, Review of Particle Physics, Journal of Physics G **33**, 1+ (2006).

[22] E. M. Aitala *et al.*, Experimental evidence for a light and broad scalar resonance in $D^+ \to \pi - \pi + \pi +$ decay, Phys. Rev. Lett. **86**, 770 (2001), hep-ex/0007028.

[23] Chung *et al.*, Annalen der Physik **507**, 404 (1995).

[24] V. V. Anisovich and A. V. Sarantsev, K-matrix analysis of the ($IJ^{PC} = 00^{++}$)-wave in the mass region below 1900 MeV, Eur. Phys. J. **A16**, 229 (2003), hep-ph/0204328.

[25] D. Aston *et al.*, A study of $K^-\pi^+$ scattering in the reaction $K^-p \to K^-\pi^+n$ at 11 GeV/c, Nucl. Phys. B **296**, 493 (1988).

[26] C. Gobel, The scalar kappa from D+ → K- pi+ pi+: Further studies, AIP Conf. Proc. **688**, 266 (2004), hep-ex/0307003.

[27] G. Punzi, Comments on likelihood fits with variable resolution, (2004), physics/0401045.

[28] D. J. Lange, The EvtGen particle decay simulation package, Nucl. Instrum. Meth. **A462**, 152 (2001).

[29] M. Sokoloff, Private communication, 2009.

[30] D. N. Brown, A. V. Gritsan, Z. J. Guo, and D. Roberts, Local Alignment of the BABAR Silicon Vertex Tracking Detector, (2008), 0809.3823.

[31] P. del Amo Sanchez *et al.*, Measurement of $D^0 - \overline{D}^0$ mixing parameters using $D^0 \to K^0_S\pi^+\pi^-$ and $D^0 \to K^0_S K^+K^-$ decays, Phys. Rev. Lett. **105**, 081803 (2010), hep-ex/1004.5053.

[32] D. Asner, Review of Charm Sector Mixing and CP Violation, Nuclear Physics B - Proceedings Supplements **170**, 223 (2007).

[33] B. Aubert *et al.*, Measurement of D0-D0bar Mixing using the Ratio of Lifetimes for the Decays D0-¿K-pi+ and K+K-, Phys. Rev. **D80**, 071103 (2009), 0908.0761.

[34] B. Aubert *et al.*, Measurement of $D^0 - \bar{D}^0$ mixing from a time- dependent amplitude analysis of $D^0 \to K^+\pi^-\pi^0$ decays, Phys. Rev. Lett. **103**, 211801 (2009), 0807.4544.

[35] E. M. Aitala *et al.*, Branching fractions for D0 → K+ K- and D0 → pi+ pi-, and a search for CP violation in D0 decays, Phys. Lett. **B421**, 405 (1998), hep-ex/9711003.

[36] J. M. Link *et al.*, A measurement of lifetime differences in the neutral D meson system, Phys. Lett. **B485**, 62 (2000), hep-ex/0004034.

[37] S. E. Csorna *et al.*, Lifetime Differences, direct CP Violation and Partial Widths in D0 Meson Decays to K+K- and pi+pi-, Phys. Rev. **D65**, 092001 (2002), hep-ex/0111024.

[38] B. Aubert *et al.*, Limits on $D^0\bar{D}^0$ mixing and CP violation from the ratio of lifetimes for decay to $K^-\pi^+$, K^-K^+ and $\pi^-\pi^+$, Phys. Rev. Lett. **91**, 121801 (2003), hep-ex/0306003.

[39] K. Abe *et al.*, Measurement of the D0 - anti-D0 lifetime difference using D0 $\rightarrow$ K pi / K K decays, (2003), hep-ex/0308034.

[40] L. M. Zhang *et al.*, Improved constraints on D0 - anti-D0 mixing in D0 $\rightarrow$ K+ pi- decays at Belle, Phys. Rev. Lett. **96**, 151801 (2006), hep-ex/0601029.

[41] M. Staric *et al.*, Evidence for D^0 - $\bar{D}^0$ Mixing, Phys. Rev. Lett. **98**, 211803 (2007), hep-ex/0703036.

[42] U. Bitenc *et al.*, Improved search for D0 mixing using semileptonic decays at Belle, Phys. Rev. **D77**, 112003 (2008), 0802.2952.

[43] B. Aubert *et al.*, Measurement of D^0 - $\bar{D}^0$ mixing using the ratio of lifetimes for the decays $D^0 \rightarrow K^-\pi^+$, K^-K^+, and $\pi^-\pi^+$, Phys. Rev. **D78**, 011105 (2008), 0712.2249.

[44] I. Adachi *et al.*, Measurement of y(CP) in D meson decays to CP eigenstates, (2008), 0808.0074.

[45] .